The Green Bank North Celestial Cap Pulsar Survey

V. Pulsar Census and Survey Sensitivity

McEwen, A.E.; Spiewak, R.; Swiggum, J.K.; Kaplan, D.L.; Fiore, W.; Agazie, G.Y.; Blumer, H.; Chawla, P.; DeCesar, M.; Kaspi, V.M.; Kondratiev, V.I.; LaRose, M.; Levin, L.; Lynch, R.S.; McLaughlin, M.; Mingyar, M.; Noori, H. Al; Ransom, S.M.; Roberts, M.S.E.; Schmiedekamp, A.; Schmiedekamp, C.; Siemens, X.; Stairs, I.; Stovall, K.; Surnis, M.; van Leeuwen, J.

DOI
10.3847/1538-4357/ab75e2

Publication date
2020

Document Version
Submitted manuscript

Published in
Astrophysical Journal

Draft version February 17, 2020
Typeset using LaTeX **twocolumn** style in AASTeX62

The Green Bank North Celestial Cap Pulsar Survey. V. Pulsar Census and Survey Sensitivity

A. E. McEwen,[1] R. Spiewak,[2] J. K. Swiggum,[1] D. L. Kaplan,[1] W. Fiore,[3,4] G. Y. Agazie,[3,4] H. Blumer,[3,4] P. Chawla,[5] M. DeCesar,[6] V. M. Kaspi,[5] V. I. Kondratiev,[7,8] M. LaRose,[3,4] L. Levin,[9] R. S. Lynch,[10] M. McLaughlin,[3,4] M. Mingyar,[3,4] H. Al Noori,[11] S. M. Ransom,[12] M. S. E. Roberts,[13,14] A. Schmiedekamp,[15] C. Schmiedekamp,[15] X. Siemens,[1] I. Stairs,[16] K. Stovall,[17] M. Surnis,[3,4] and J. van Leeuwen[7,18]

[1] *Center for Gravitation, Cosmology, and Astrophysics, Department of Physics, University of Wisconsin-Milwaukee, P.O. Box 413, Milwaukee, WI 53201, USA*
[2] *Centre for Astrophysics and Supercomputing, Swinburne University of Technology, P.O. Box 218, Hawthorn, VIC 3122, Australia*
[3] *Department of Physics and Astronomy, West Virginia University, Morgantown, WV 26506, USA*
[4] *Center for Gravitational Waves and Cosmology, West Virginia University, Chestnut Ridge Research Building, Morgantown, WV 26505*
[5] *Department of Physics & McGill Space Institute, McGill University, 3600 University Street, Montreal, QC H3A 2T8, Canada*
[6] *Department of Physics, 730 High St., Lafayette College, Easton, PA 18042, USA*
[7] *ASTRON, the Netherlands Institute for Radio Astronomy, Oude Hoogeveensedijk 4, 7991 PD Dwingeloo, The Netherlands*
[8] *Astro Space Centre, Lebedev Physical Institute, Russian Academy of Sciences, Profsoyuznaya Str. 84/32, Moscow 117997, Russia*
[9] *Jodrell Bank Centre for Astrophysics, School of Physics and Astronomy, The University of Manchester, Manchester, M13 9PL, UK*
[10] *Green Bank Observatory, P.O. Box 2, Green Bank, WV 24494, USA*
[11] *Department of Physics, University of California, Santa Barbara, Santa Barabara, CA 93106, USA*
[12] *National Radio Astronomy Observatory, 520 Edgemont Road, Charlottesville, VA 23903, USA*
[13] *New York University Abu Dhabi, Abu Dhabi, UAE*
[14] *Eureka Scientific, Inc., 2452 Delmer St., Suite 100, Oakland, CA 94602, USA*
[15] *Department of Physics, The Pennsylvania State University, Ogontz Campus, Abington, Pennsylvania 19001, USA*
[16] *Dept. of Physics and Astronomy, UBC, 6224 Agricultural Road, Vancouver, BC, V6T 1Z1 Canada*
[17] *University of New Mexico, Albuquerque, NM 87131*
[18] *Anton Pannekoek Institute for Astronomy, University of Amsterdam, Postbus 94249, 1090 GE Amsterdam, The Netherlands*

ABSTRACT

The Green Bank North Celestial Cap (GBNCC) pulsar survey will cover the entire northern sky ($\delta > -40°$) at 350 MHz, and is one of the most uniform and sensitive all-sky pulsar surveys to date. We have created a pipeline to re-analyze GBNCC survey data to take a 350 MHz census of all pulsars detected by the survey, regardless of their discovery survey. Of the 1413 pulsars in the survey region, we were able to recover 670. For these we present measured signal-to-noise ratios (S/N), flux densities, pulse widths, profiles, and where appropriate, refined measurements of dispersion measure (656 out of 670) and new or improved spectral indices (339 out of 670 total, 47 new, 292 improved). We also measure the period-pulse width relation at 350 MHz to scale as $W \propto P^{-0.27}$. Detection scans for several hundred sources were reanalyzed in order to inspect pulsars' single pulse behavior and 223 were found to exhibit evidence of nulling. With a detailed analysis of measured and expected S/N values and the evolving radio frequency interference environment at 350 MHz, we assess the GBNCC survey's sensitivity as a function of spin period, dispersion measure, and sky position. We find the sky-averaged limiting flux density of the survey to be 0.74 mJy. Combining this analysis with PsrPopPy pulsar population simulations, we predict 60/5 non-recycled/millisecond pulsar discoveries in the survey's remaining 21,000 pointings, and we begin to place constraints on population model parameters.

1. INTRODUCTION

The Green Bank North Celestial Cap (GBNCC; Stovall et al. 2014) pulsar survey began in 2009 and, when complete, will cover the entire sky accessible to the 100 m Robert C. Byrd Green Bank Telescope (GBT; $\delta \geq -40°$, or 85% of the celestial sphere) at 350 MHz. As of mid-2019, the survey is 85% complete and 161 pulsars have been discovered, including 25 millisecond pulsars (MSPs) and 16 rotating radio transients (RRATs; McLaughlin et al. 2006). Timing solutions for these discoveries have been published in Stovall et al. (2014),

Corresponding author: A. E. McEwen
aemcewen@uwm.edu

Karako-Argaman et al. (2015), Kawash et al. (2018), Lynch et al. (2018), and Aloisi et al. (2019), and more are forthcoming. As such, this constitutes one of the largest and most uniform pulsar surveys to date.

In addition to the newly discovered pulsars, the uniform coverage of GBNCC allows a robust re-assessment of the known pulsar population with reliable flux density measurements. Here we present a detailed search for all known pulsars in the GBNCC footprint. We find that 572 previously published pulsars and 98 unpublished pulsars have been re-detected by the survey pipeline and visually confirmed, comprising 670 detections in total, the largest low-frequency, single-survey sample. Similar to previous efforts based on results from the Parkes Multibeam Pulsar Survey (PMPS) and the Pulsar Arecibo L-band Feed Array (PALFA) survey (e.g., see Lorimer et al. 2006; Swiggum et al. 2014; Lazarus et al. 2015), we conduct a detailed analysis of the GBNCC pulsar survey and compare its sensitivity with that of other surveys in overlapping regions of sky. Flux densities at 350 MHz (S_{350}) are presented for all detections, as well as pulse widths and profiles.

In §2, we outline the process used to generate a comprehensive list of pulsars as well as predicting and measuring signal-to-noise ratios (S/N) of detections in the survey. In §3, we present the recovered S/N and flux density measurements for all detected pulsars as well as measurements of pulse width, dispersion measure, and spectral index. We also present the profiles for all of these pulsars. In §4, we discuss how the GBNCC survey is performing compared to expectations and RFI characteristics of the survey, and remark on interesting detections and notable non-detections. We also discuss the implications of our results for the Galactic pulsar population. Finally, in §5, we summarize the main conclusions of this analysis.

2. SAMPLE ASSEMBLY AND DATA REDUCTION

The GBNCC data set as of late fall 2018 included ∼108,000 120 s pointings, each tagged with a unique beam number. Each dual-polarization observation was taken with the GBT over the past ≃10 years. The survey utilizes the GUPPI backend, with a sampling time of 82 μs and 100 MHz of bandwidth centered at 350 MHz (for more information on the observing setup for the GBNCC survey, see Stovall et al. 2014). We began by organizing a comprehensive list of all known pulsars with parameters that were available for use, whether they were published or not. By utilizing the Australia Telescope National Facility (ATNF) pulsar catalog[1] (v1.59, Manchester et al. 2005), we amassed the bulk of the sources from the list of all published pulsars and their positions on the sky as well as their spin parameters and other relevant quantities (dispersion measure, etc.). Discovery parameters are also available for additional pulsars that have not been published but were detected in a number of other recent or ongoing surveys. Many of these surveys, including AODrift (Deneva et al. 2013), SUPERB (Keane et al. 2018, Spiewak et al., 2019, in prep.), GBT 350 MHz Drift (Boyles et al. 2013), PALFA (Cordes et al. 2006; Lazarus et al. 2015), LOTAAS (Sanidas et al. 2019), and HTRU-South (Keith et al. 2010) include pulsars that are in GBNCC survey area, and so were included in the list. More information on these surveys is included in Table 1. Furthermore, we included the list of pulsars that had been discovered in the search pipeline for the GBNCC survey. We then limited this list to pulsars within the range of the survey, i.e., pulsars with $\delta > -40°$. In total, this list contained 2299 pulsars. We determined which pulsars were within 30′ (FWHM of GBT at 350 MHZ) of completed GBNCC pointings, adjusting when necessary to compensate for large (>30′) uncertainties in pulsar position. This reduced the total number of pulsar candidates to 1413. We could then match each pulsar with the GBNCC beams closest to its position before beginning to process the data.

Radio frequency interference (RFI) excision is the first step of GBNCC data analysis, and is done primarily with the `rfifind` tool from the `PRESTO`[2] pulsar data analysis software package (Ransom 2001) as described in §3.1 of Stovall et al. (2014). We also performed an analysis of the `rfifind` output files spanning the lifetime of the GBNCC survey up to late 2018 (roughly 83% of the total survey) to characterize the effects of RFI over the course of the survey. These files contain information about which frequency channels were masked due to RFI for every 120 second scan in the survey. For a particular scan, the effective bandwidth $\Delta\nu$ is the total 100 MHz bandwidth of the GBT 350 MHz receiver multiplied by the ratio of unmasked to total channels for that scan, minus an additional 20 MHz for rolloff.

In some cases, the `rfifind` masks were insufficient to remove additional RFI that was either narrow in frequency space or brief in time. The latter often appears as a very bright burst at ∼0 DM for portions of the observation. To mitigate this, we employed some additional narrowband flagging in the `PRESTO prepfold` command as well as removing corrupted portions of the

[1] http://www.atnf.csiro.au/research/pulsar/psrcat

[2] http://www.cv.nrao.edu/~sransom/presto/

scan in the time-domain. Note that these changes also alter the values for $\tau_{\rm obs}$ and $\Delta\nu$ which consequently change the measured S/N for a given observation. For this reason, we calculate the fraction of data points from the observations that were not omitted in processing and multiply the total bandwidth by this fraction.

After removal of RFI, we dedispersed and folded the observations at each pulsar's rotational period and integrated the profiles to obtain a single average profile for each observation. For the vast majority of sources included in this analysis, a precise ephemeris from the ATNF catalog was used to perform the folding. In all other cases, only the discovery parameters (period, DM and, if known, period derivative) were used. We also repeated this process while allowing dispersion measure to vary and, in some cases, also allowing variations in period and period derivative. This second iteration allows for fine-tuning previously published parameters at the cost of potentially finding bright RFI, which will often occur when attempting to detect low-DM pulsars as sources of RFI have DM $= 0\,{\rm pc\,cm^{-3}}$. The 120 second observation times utilized in the GBNCC survey limit sensitivity to period refinement, so fitting for period was only used to increase the S/N of detections of pulsars for which only discovery parameters were used, and no further timing analysis was done as a part of this study. All folded data were visually inspected to determine likelihood of an actual detection. In cases where RFI still existed in the data, we removed high order (>5) polynomials from the off-pulse regions of the profile. With folded profiles, we calculated a measured signal-to-noise ratio (S/N) (Lorimer & Kramer 2004),

$$\mathrm{S/N_{meas}} = \sum_{i=0}^{N_{\rm bin}} \frac{p_i - \bar{p}_{\rm off}}{\sigma_{\rm off}\sqrt{W N_{\rm bin}/P}}\,\gamma, \qquad (1)$$

where $N_{\rm bin}$ is the number of bins across the pulse profile, p_i is the value of bin i, $\bar{p}_{\rm off}$ is the mean of the off-pulse bins, $\sigma_{\rm off}$ is the standard deviation of the off-pulse bins, W is the on-pulse width in seconds, P is the pulsar spin period in seconds, and γ is a correction factor. When continuous signals are assigned to a finite number of bins in the profile during the folding process in `PRESTO`, their intensity is "smeared" over the neighboring bins, resulting in correlations in the bins' intensities. This correction, dubbed γ, depends on the sampling time and the number of bins in the profile, which (for this study) is dependent on the pulsar spin period. Typical values are close to 0.95. The number of bins $N_{\rm bin}$ was determined by the pulsar period as follows: profiles for pulsars with periods shorter than 1.7 ms had 28 bins, periods shorter than 10 ms had 50 bins, periods shorter than 50 ms had 128 bins, and all others had 200 bins. This prescription retains sensitivity to long-period pulsars but avoids bin widths corresponding to time intervals smaller than the sampling time of 82 μs. Pulse widths were determined with a standard process. First, sigma-clipping was used to find the off-pulse region. Then, the peak value above the noise floor was identified, and bins on either side of the peak were added to the on-pulse width. This process was repeated, adding bins on the sides of the peak until we reached bins within 2σ of the mean of the noise. The edges of the pulse were found by fitting lines to the two bins on either side of the pulse and finding the fraction of the outermost bins that were above the noise floor. At this point, we consider the full on-pulse width to be determined. Each profile was then checked by eye, and corrections to the on-pulse region were made. Any components of the pulse width that were distinct from the main pulse were determined using the same algorithm. To determine the sensitivity of uncertainties in S/N from the choice of the number of on-pulse bins, noisy Gaussian pulses were simulated and various width choices were used to measure the fractional error on S/N. From this test, it was found that on-pulse widths that exceed at least one σ beyond the Gaussian mean were sufficient to greatly reduce the fractional uncertainty on S/N. Beyond this, adding bins had little effect on this fractional uncertainty - so, pulse widths were chosen to encompass all of the pulse visible above the noise. In some cases, additional RFI features were removed prior to the determination of W to minimize errors in W and S/N (see §4.2).

Characteristic measurements of pulse width include measurements at both 50% and 10% of the pulse profile's maximum amplitude (hereafter W_{50} and W_{10}, respectively). These widths are dependent on both pulse period and observing frequency, so measurements at 350 MHz help to fill out the low-frequency regime for a wide range of pulse periods. However, the noise floor in some pulsars limits the ability to determine W_{10} robustly. Note also that W_{50} and W_{10} are distinct from W, which includes all bins that contain the pulse signal, and so W is generally slightly larger than W_{10}.

The expected S/N of a pulsar can be estimated as (Dewey et al. 1985a; Lorimer & Kramer 2004)

$$\mathrm{S/N_{exp}} = \frac{S_{350} G \sqrt{N_{\rm pol}\tau_{\rm obs}\Delta\nu}}{T_{\rm sys}\beta}\sqrt{\frac{P-W}{W}}f(\theta), \qquad (2)$$

where S_{350} is the flux density at 350 MHz, $G = 2\,{\rm K/Jy}$ is the gain of the Green Bank Telescope (Stovall et al. 2014), $N_{\rm pol} = 2$ is the number of polarizations recorded, $\tau_{\rm obs} = 120\,{\rm s}$ is the length of the observation, $\Delta\nu$ is the bandwidth in MHz after removing RFI (see §4.2), $T_{\rm sys}$ is the system temperature (including the sky temperature

at the source position, receiver temperature $\simeq 20\,\mathrm{K}$, and CMB temperature $\simeq 3\,\mathrm{K}$), $\beta \simeq 1.1$ is an instrument-dependent correction factor due to downsampling the data to 2 bits (Lorimer & Kramer 2004), and $f(\theta)$ is a radial Gaussian factor accounting for sensitivity degradation as a function of angular offset from the center of the circular beam θ. The sky temperature in the direction of each pulsar was determined by using the measurements made by Haslam et al. (1981) for the beam positions, scaled to 350 MHz using with the spectral index therein, -2.6.

Where possible we use flux densities at other frequencies and previous measurements of spectral index (α, with $S_\nu \propto \nu^\alpha$) from the ATNF catalog to determine an expected flux density at 350 MHz and the expected S/N (Manchester et al. 2005). In cases where there was no published value for α but flux densities at both 400 MHz and 1400 MHz were published, we determine a spectral index using a simple power law. In all other cases, we assume a spectral index of -1.4 (Bates et al. 2014) to estimate the flux density at 350 MHz. We also calculate the measured flux density of each pulsar by inverting Equation 2 and using measured values for S/N (determined from Equation 1) and pulse width. Comparing the expected flux density to our measurements can both roughly confirm our current models for pulsar emission as well as aid in explaining non-detections.

3. PULSAR FLUX DENSITY CENSUS AT 350 MHZ

We detected 670 pulsars out of a total of 1413 in the survey area, and these detections are listed in Table 4 in Appendix 1. For all following analysis, the beams corresponding to the brightest detections (highest S/N) were used, as these are most likely to represent the pulsars' flux density. Along with pulsar names, we provide several relevant quantities: dispersion measure from searching with `PRESTO` (Ransom 2001), MJD of the brightest detection, angular offset from the center of the beam, W_{50}, W_{10} (when S/N was large enough), detection S/N, 350 MHz flux density measured from the GBNCC data, and measured spectral index α (see §3.2). Uncertainties on the S/N and flux densities were calculated using standard error propagation from equations 1 and 2 and uncertainties on bandwidth, temperature, and θ of 5 MHz, 10 K, and 0.5 degrees, respectively. Among these are 66 millisecond pulsars (MSP), defined here as pulsars with spin periods shorter than 30 ms. The integrated pulse profiles for all of the brightest detections are shown in Figures 13 – 24 along with pulsar names, dispersion measure, and flux density. Figure 1 shows all detected pulsars plotted by their Galactic positions, and different markers indicate whether or not the pulsars were from the ATNF catalog or were a part of one of the other survey lists mentioned above.

3.1. *Comparison Between the GBNCC and Overlapping Pulsar Surveys*

Out of the 210 pulsars with discovery parameters that are not currently listed in the ATNF catalog, 98 were detected. Names, central frequencies, scaled limiting flux densities, and the ratio of detected to processed pulsars are given for each survey in Table 1. It should be noted that there are many pulsars from these surveys (excluding GBNCC) in regions of the sky where the GBNCC survey has yet to observe, and so they may be detected in the future; these pulsars are not included in the counts listed in Table 1. Three of these surveys (SUPERB, HTRU-S, PALFA) were conducted at higher frequencies,, where average sky temperature (especially near the Galactic plane) is much lower. This reason and the increased sensitivity to high DM pulsars at high frequency is useful for diagnosing missed detections. Because these pulsars have neither published flux densities nor spectral indices, reasons for missed detections cannot be determined more robustly than those due to sky temperature, position relative to the survey, extreme nulling/intensity variation, and high DM/short periods. It is also possible that for some of these pulsars, the discovery parameters may not be precise enough to be found in this analysis.

The most surprising missed detections come from the GBT350, AODrift, and LOTAAS surveys, which all have comparable sensitivities and frequencies. In an effort to explain why these pulsars were missed, all of the discovery plots were checked against our results, and acceleration searches were run. Three pulsars (J0100+69 and J0121+14 from LOTAAS, and J1854+36 from AODrift) that were originally missed were found on the second trial, as the DM used in the first run was not close enough to the DM at which the pulsar was discovered. For the majority of pulsars that were not detected after re-running the pipeline, the discoveries were quite dim. The LOTAAS survey also has much longer integration times (60 minutes), which significantly improves the chances of the survey detecting pulsars which may be faint and/or nulling. When checking the discovery plots, it became clear that both of these effects were common to many of the missed pulsars. Some pulsars even appeared to exhibit nulling with 'off' times as large as 100 seconds. Nulling behavior was also seen in many cases for the AODrift survey. For the GBT350 missed pulsars, all three of those that were missed were faint, and several GBNCC beams in which the pulsars were

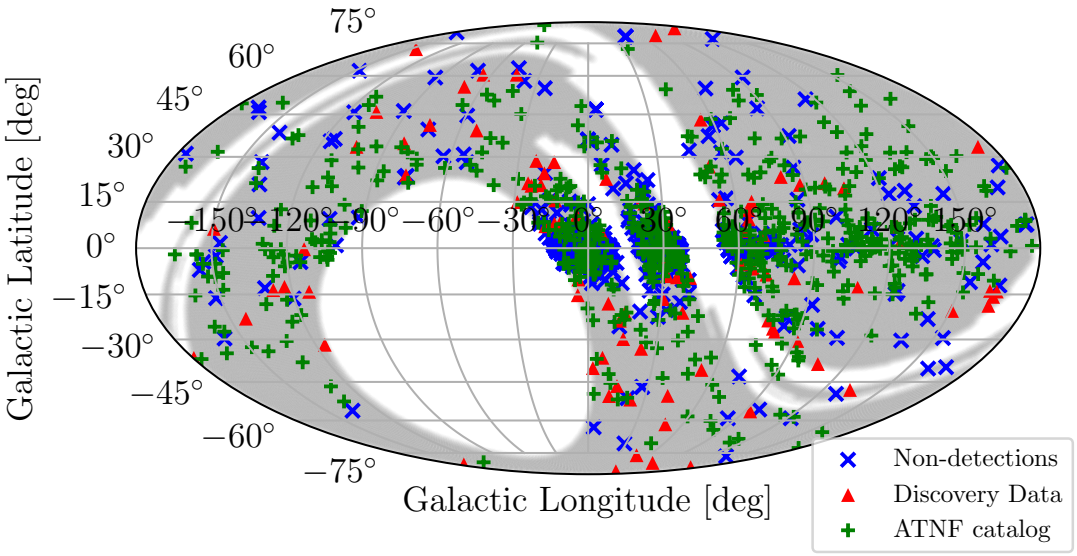

Figure 1. Sky map with pulsars from overlapping surveys, plotted in Galactic coordinates as a Mollweide projection. The shaded regions indicate completed GBNCC observations. Detected pulsars from the ATNF catalog and pulsars that were detected using discovery parameters from overlapping surveys are differentiated by marker type, with green plus symbols indicating pulsars from the catalog and red triangles indicating pulsars from the surveys listed in Table 1. Pulsars that were not detected are plotted as blue "x" symbols.

most likely to be found had RFI that spanned the entire 100 MHz band.

Eight binary pulsars that were originally discovered in the GBNCC survey were not detected in the first pass of this pipeline. These pulsars required acceleration searches, which are automatically performed as a part of the search pipeline, but not here. As a part of the missed pulsar analysis, we ran an additional acceleration search using `ACCELSEARCH` from within the `PRESTO` package, and they were all detected. We also reprocessed data for 15 binary pulsars from the ATNF catalog with short ($\leq$ 0.5 day) orbital periods that were not detected in the first pass using acceleration searches; none of these were detected.

Pulsars with long periods (greater than 2.5 s) were also followed up with a search for single pulses. Because these pulsars would only be observed for at most 48 pulses, non-detections are more common. To address this, we implemented `single_pulse_search.py` from the `PRESTO` package, which searches a range of dispersion measures to find bright single pulses in the data and characterize them by their S/N. In this way, a pulsar that is not detected via a periodicity search may be found by individual pulses. However, we were still unable to find these pulsars using this method.

3.2. *Spectral Indices*

Many previously published spectral indices were determined from flux measurements from high-frequency surveys (e.g., see Jankowski et al. 2018a). Therefore, low frequency surveys like the GBNCC survey provide more stringent constraints on these calculations. Results from this analysis are listed in Table 4. The majority of the pulsars in this data set follow a single power law, or do not have enough (>2) flux density measurements to fit multiple power law functions. However, there are a small number of cases where the emission is better fit by a broken power law, defined instead as a piecewise function composed of two power laws. All 339 pulsars for which we measured spectral index had three or more flux measurements (including our 350 MHz measurements) and were checked by eye to determine whether or not a broken line fit was appropriate. Four pulsars fit these criteria. For these pulsars, we fit two lines, one for high frequency flux density measurements and one for low frequency. The breaking point for the power law was determined by finding the maximum change in the derivative of flux density with respect to frequency. A similar analysis was done in Murphy et al. (2017). Plots of these cases are provided in Figure 2 with both indices included. These plots also display the best-fit line to all measured flux densities. The measured values of α_l and α_h are reported in Table 2.

Table 1. Pulsar Survey Comparison

Survey	Central Frequency (MHz)	Limiting Flux Density[a] (mJy)	Detections[b]	Reference
AODrift	327	0.59	7/13	Deneva et al. (2013)
HTRU−S (low-lat)	1352	0.40	0/9	Keith et al. (2010)
HTRU−S (med-lat)	1352	0.95	3/27	Keith et al. (2010)
HTRU−S (high-lat)	1352	1.2	1/8	Keith et al. (2010)
SUPERB	1352	0.4	2/15	Keane et al. (2018), Spiewak et al. (in prep)
LOTAAS	134	0.63	10/39	Sanidas et al. (2019)
PALFA	1400	0.23	0/29	Lazarus et al. (2015)
GBT350	350	0.59	3/6	Boyles et al. (2013)
GBNCC	350	0.70	72/72	Stovall et al. (2014)

[a] Averaged over the survey area and scaled to 350 MHz.

[b] Number of detections of pulsars from this survey by GBNCC/number of pulsars from this survey within the GBNCC survey area.

Note—Information about individual detections is reported in Table 4.

Table 2. Broken Powerlaw Spectral Indices

PSR	α_l[a]	α_h[a]	Break Frequency (MHz)
J0034-0534	0.6(3)	−3.1(2)	181
J0218+4232	1.15(7)	−2.7(4)	149
J1900-2600	0.2(4)	−1.89(15)	204
J2002+4050	0.2(16)	−1.51(18)	378

[a] Spectral indices below (α_l) and above (α_h) the break.

Note—Quantities in parentheses are uncertainties in the last digit. See Figure 2 for the corresponding plots.

3.3. *Comparison of Dispersion Measure with Catalog Values*

The relatively low frequency of the GBNCC survey allows much higher precision DM measurements than typical 1400-MHz surveys, as dispersion across the band scales as ν^{-2}. As pulses propagate through the interstellar medium, this dispersion results in a frequency dependent delay that smears out the arrival time of the pulse. Tools within the `PRESTO` package adjust for this, shifting the low frequency portion of the signal back in time to line up the pulse across the band. Using the `dmsearch` flag contained within the `PRESTO` command `prepfold`, we processed each of the pulsars and recovered more accurate values of DM. The program adjusts for dispersion and then folds the data at the pulsar's period to line up the pulses in both time and frequency. When `dmsearch` is off, the program does not tune the DM to maximize S/N; otherwise, the DM which aligns the pulses in frequency is returned as a new DM. In some cases, RFI caused the DM searching algorithm to return erroneous values for DM, and so we were unable to refine the dispersion measure. For these pulsars, we include the previously published DM in Table 4 and mark them with a double dagger. More often, we were able to improve upon the previously published values of DM. Most of the discrepancies were small, but in some cases, our more precise DM measurement differed from the previous value significantly. For the pulsars with significant changes to their previously catalogued DM, we followed up with `TEMPO`[3] (maintained and distributed by Princeton University and the Australia Telescope National Facility). We split each detection into four subbands and created precise pulse times-of-arrival (TOAs) which can then be utilized to fit for DM. This method provides marginally more precise measurements, and so was only performed on pulsars with significant changes to previous DM measurements ($\geq 3\sigma$). All newly measured DMs are presented in Table 4, and Table 5 highlights the pulsars which were followed up with `TEMPO` timing.

4. SURVEY SENSITIVITY

4.1. *Efficiency of GBNCC Survey*

In total, there were 5633 unique beams analyzed, yielding 1328 unique detections of the 670 pulsars. Given that there were 102948 beams that had been

[3] http://tempo.sourceforge.net

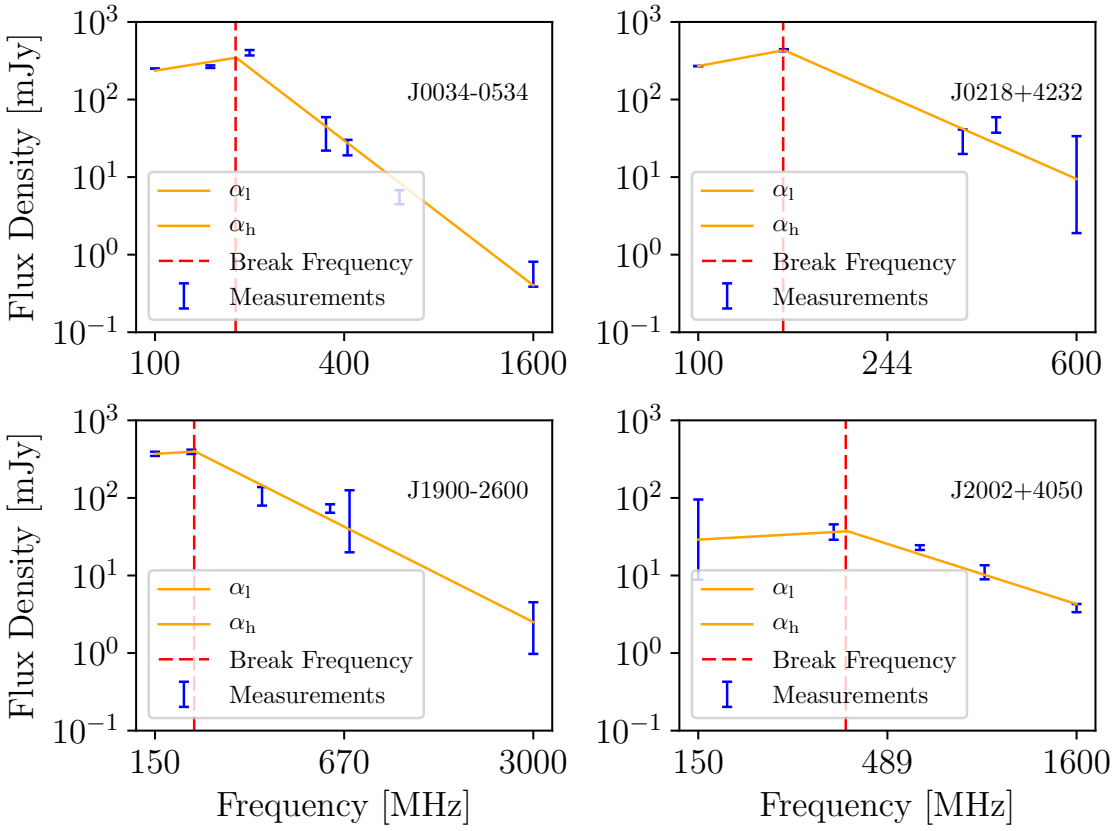

Figure 2. Pulsars with broken power-law spectral indices. We plot all available measurements of flux density in the ATNF catalog as well as the 350 MHz measurements made in this study against observing frequency. We fit two disjoint lines to the low- and high-frequency measurements (orange solid lines). The red dashed line indicates the frequency of the turnover in the spectrum, determined by finding the point at which the two lines match up. Information for these measurements is presented in Table 2.

observed at the beginning of this project, this corresponds to an average number of detections per beam of ~ 0.013 (0.063 detections per square degree), and ~ 0.38 detections per hour of observing. The ability to detect pulsars at 350 MHz is limited most stringently by sky temperature and scattering in the interstellar medium (which correlates with dispersion). The expected S/N for detections is inversely proportional to system temperature, which is dominated by sky temperature near the Galactic plane. At 350 MHz, this effect is quite significant, with temperatures approaching 1000 K in this region. Scattering is especially detrimental in the detection of pulsars with short periods, as even a few milliseconds of smearing can eliminate the pulse entirely. Given a particular spin period and the estimated DM smearing, we can estimate the minimum flux density that will be detected by the survey. This relationship comes from solving Equation 2 for flux density and assuming both an average sky temperature and duty cycle for the pulsars in the survey. Plotted in Figure 3 are curves corresponding to a number of trial values of DM, showing the sensitivity floor at those values. Because DM and sky temperature are correlated, we determined the average sky temperature for each curve that is plotted, resulting in an increase in minimum detectable signals for higher DM pulsars. Also plotted are flux density measurements for detections made by this survey and expected flux density measurements for the pulsars which were not successfully detected. The colors in the plot correspond to the dispersion measure of each pulsar, showing how pulsars that may be intrinsically bright enough to be detected can still be missed because of dispersive smearing and/or scattering. The minimum flux density expected to be measured in the survey (regardless of spin period) can be determined to be the asymptotic value of the DM curve corresponding to the faintest detection. This value is directly proportional to the minimum S/N which results in a detection, hereafter S/N_{cut}, which was found to be ~ 3.8. For all detections, we plot both the expected S/N at 350 MHz as well as the measured S/N of the detection. These are plotted in Figure 4 along with a line marking unity. There is

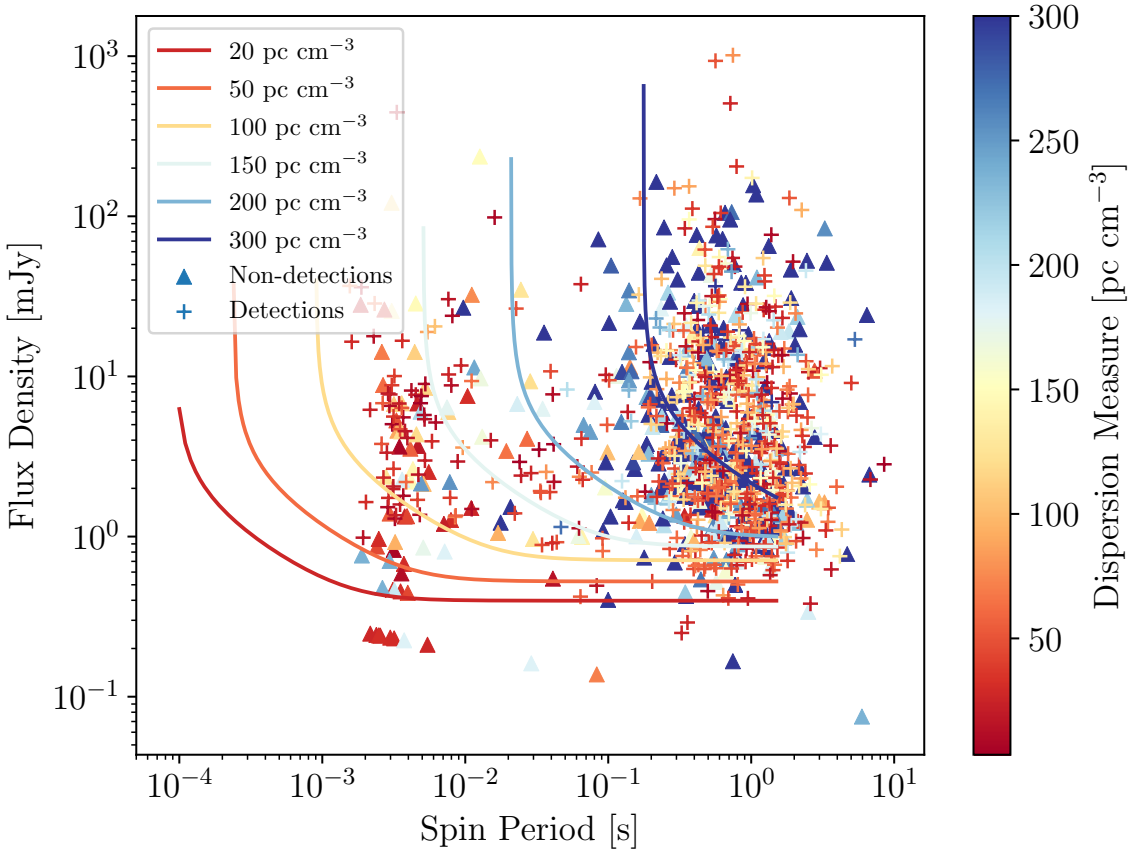

Figure 3. Flux density sensitivity in the GBNCC as a function of pulse period. Assuming a duty cycle of 6% and an average unmasked bandwidth of 67 MHz (which incorporates a 20 MHz rolloff in the bandpass), we plot the predicted lower limit on the flux density of detectable pulsars for dispersion measures of 20, 50, 100, 150, 200, and 300 pc cm^{-3}. To determine the sky temperature for the curves, we found the average sky temperature as a function of DM using the sky temperatures at the positions of all detected pulsars. We then drew from this function the temperatures at each DM for which a curve is plotted. For the above DMs, the function returns 95, 126, 171, 208, 237, and 273 K. We glean the minimum detectable S/N for the survey by matching the curves to the faintest detection. This was found to be ∼3.8. Higher DM pulsars are more susceptible to smearing, and so the likelihood of detection is decreased for high DM, short period pulsars. We also plot both the detections (plus symbols) and non-detections (triangles), which are colored by their DM.

a large spread about this line, due mostly to stochastic noise sources in the data (telescope noise, temperature fluctuations, scintillation, and variable pulsar emission). When examining these results, several of the more significant outliers were analyzed in closer detail. One of the three significant outliers in the lower right portion of the plot was found to be a new nulling candidate, and the other two were initially labeled as possible nullers that could not be verified without higher resolution observations.

Low frequency observations can result in significant deterioration of the pulse due to scattering and scintillation effects, as residual dispersive time delay within a frequency channel with finite width increases as ν^{-3} and scattering roughly as ν^{-4} (Lorimer & Kramer 2004). Both of these phenomena result in a broadened pulse and subsequently a reduction in S/N. To shed light on the causes for some of the missed pulsars, we calculate the expected S/N using information from both the catalog and information about the beams in which we expect to detect them. We predict flux density at 350 MHz calculated as described in §2, determine the masked fraction of the closest beam to the pulsar's position (when measured), and determine T_{sys} for the corresponding sky position. To determine W, we fit a line to our measurements of W_{10} as a function of spin period and draw from this function. This allows for a measurement of the spin period-pulse width relation at 350 MHz, supplementing previous measurements at other frequencies. This best fit line was measured to be $W_{10} = 18.5^\circ(4)P^{0.270(10)}$, which is consistent with the relation determined in Johnston & Karastergiou (2019) modulo a frequency-dependent scaling factor (for a more

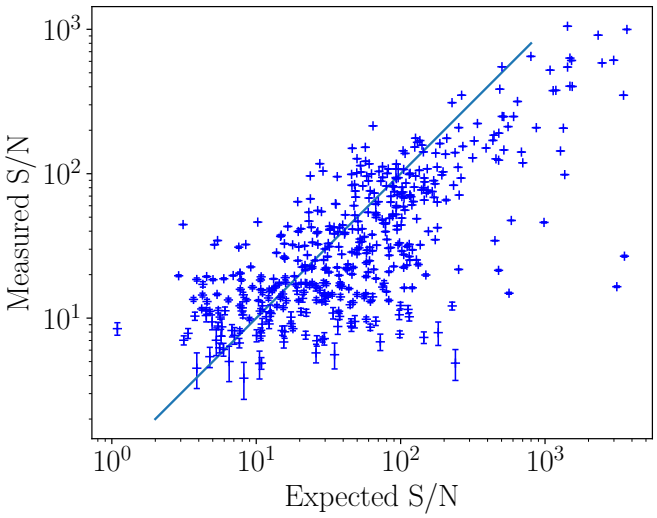

Figure 4. Measured S/N vs. expected S/N for detections in the GBNCC survey. Extrinsic contributions to expected S/N include system temperature, telescope gain, scintillation, and offset from the beam center (newer pulsars without full timing solutions may have significant uncertainties in position). Errors in these quantities, previous flux measurements, and spectral indices increase the spread about unity, as does variable pulsar emission, i.e. nulling.

in-depth analysis, see Chen & Wang 2014). This fit is shown in Figure 5.

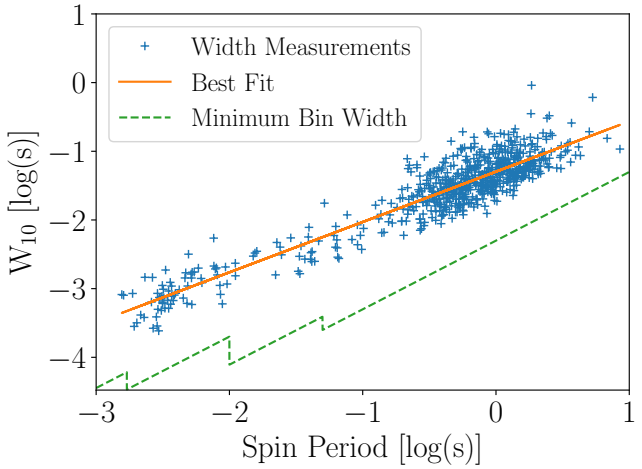

Figure 5. Pulse width at 10% of the pulse maximum as a function of spin period. The solid line shows the line of best fit through the data, described by $W_{10} = 18.5^\circ(4)P^{0.270(10)}$. The dashed line shows the minimum bin width as a function of period, as described in §2.

After drawing widths from either the catalog or the above function (based on availability of previous measurements of W_{10} near 350 MHz), we determined the expected S/N for all non-detections. These are plotted along with the measured S/N for all of the detections in Figure 6. The detections have been divided between those found from the catalog and those discovered by the GBNCC survey, and non-detections are divided based on Galactic latitude. These divisions allow for direct comparison between the survey's ability to detect pulsars blindly as well as the limits placed on the survey by high temperatures and scattering near the Galactic plane. Included in the plot are three different S/N cutoffs placed during different stages of the survey. The least stringent cutoff of S/N = 12 comes from Stovall et al. (2014), where it was used as an estimated cutoff for detection to predict the survey's sensitivity. At this S/N, ≃75% of non-detections are not expected to be detected. Pulsars close to the plane generally have lower S/N as the temperature is so high, while pulsars outside of the plane generally have smaller DM and temperature but more scintillation. The two detection curves show that the GBNCC is sensitive to intrinsically fainter pulsars, as the histogram is skewed toward lower measured S/N than those from the catalog. Note that there was one pulsar discovered by the GBNCC search pipeline with S/N = 5.98, which is the bin to the left of the search S/N cutoff.

In Figure 7, we plot all pulsars' periods against their dispersion measure. Each point's color and shape describe whether or not the pulsar was detected, and if not, whether we expect to have detected it. Missed detections that were unexpected are plotted with point sizes reflecting the expected flux density (calculated as described in §2) normalized by the value of the effective sensitivity curve for that pulsar, so larger points indicate pulsars with expected flux density much higher than the minimum detectable flux density at the pulsar's position.

In total, there are 116 undetected pulsars plotted in Figure 7 that have been classified as "unexpected" by the logic above. Many of these pulsars are quite close to the sensitivity line, and so small errors in other flux density measurements and spectral indices may change them to "expected." Because the effective sensitivity curve includes temperature and bandwidth (RFI, by proxy) information, reasons for missed detections are limited to effects that are harder to characterize. The most likely contributors include scintillation, abnormal pulsar behavior (i.e. nulling), and imprecise previous measurements of pulsar parameters resulting in inflated expected flux densities. Scintillation depends on DM (Cordes & Lazio 1991), with increased timescales for smaller DM. Many of the non-detected pulsars that are outside of the Galactic plane are in this low-DM high-scintillation regime, and are likely to have been obscured

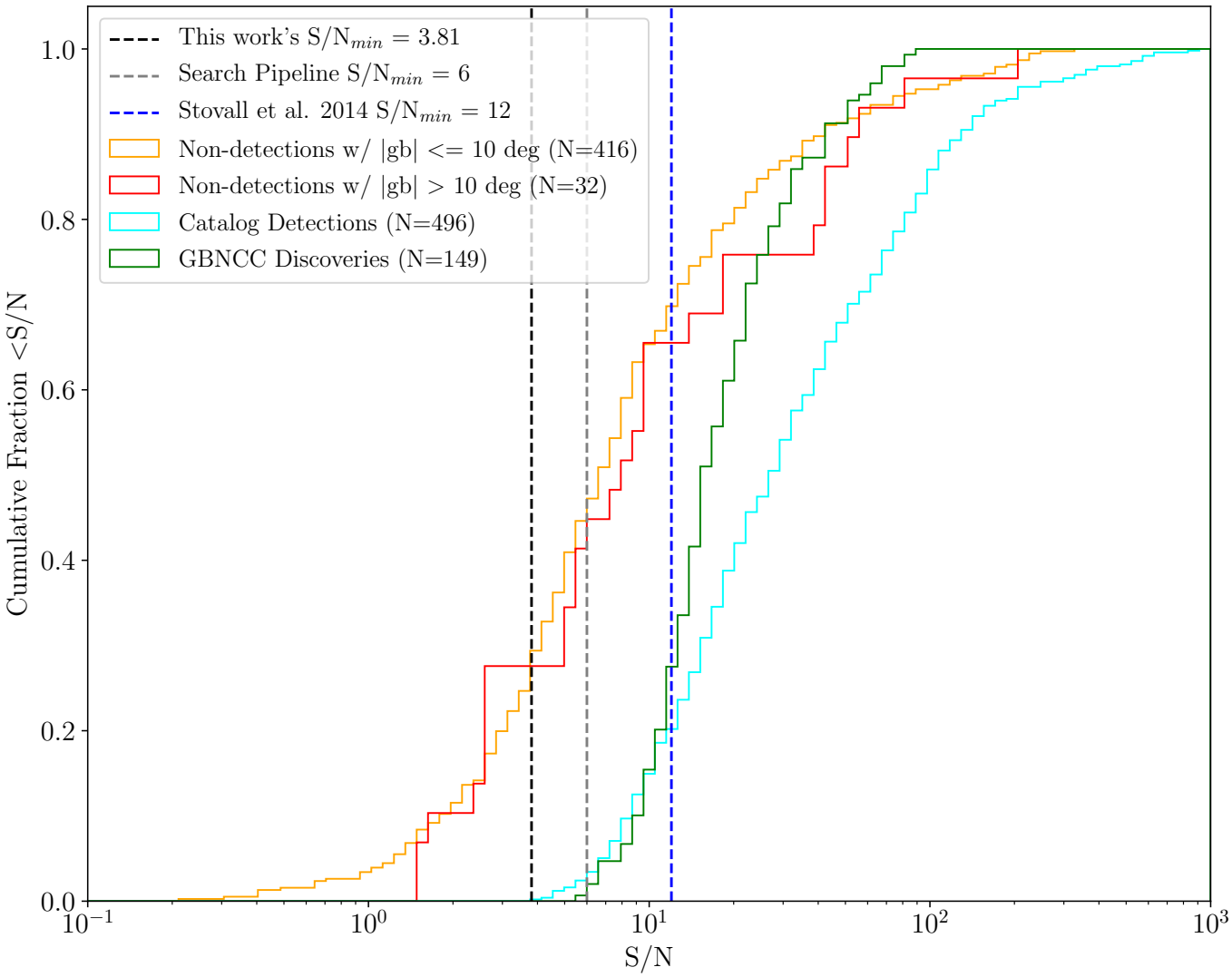

Figure 6. Histograms of measured S/N for detections and expected S/N for non-detections. Detections are differentiated by GBNCC discovery/catalog pulsars (green/cyan lines), and non-detections by distance from the Galactic plane (the red line indicates pulsars that are within 10° from the plane, and the orange line indicates pulsars outside of this region). The dashed lines indicate three different S/N cutoffs: the first line, in black, show the minimum S/N detected in the survey; the second, in grey, indicates the significance down to which candidates are folded in the GBNCC search pipeline; and the third, in blue, shows the predicted S/N limit used in Stovall et al. (2014) to predict sensitivity of the survey.

(the expected number of scintles in the observation are on the order of ∼10). Many of the other missed detections, especially those from surveys with comparable limiting fluxes, were inspected individually. Many of these were obscured by significant RFI across the band. For example, PSR J0108−1431 (spin period of $\simeq 0.81$ s and DM of 2.38 pc cm^{-3}, to the right of the bottom center of Figure 7) should be easily detected but was obscured by RFI. When examining a number of the other sources, it was found that many of the published spectral indices came from a 1400 MHz study conducted by Han et al. (2017), and were unusually steep. This steepness results in high expected values of flux at 350 MHz, which are not reflected in our results.

4.2. *RFI Analysis*

To visualize how RFI affects the efficiency of the survey, we determined the limiting flux density for each beam based on a S/N cutoff of 3.8, the temperature at the sky position of the beam, and the bandwidth available after RFI excision. Figure 8 displays a histogram of the beams by their limiting flux, and Figure 9 shows these same data projected onto their sky positions. The sky map depicts a few important characteristics of the survey: the most obvious is the decreased sensitivity

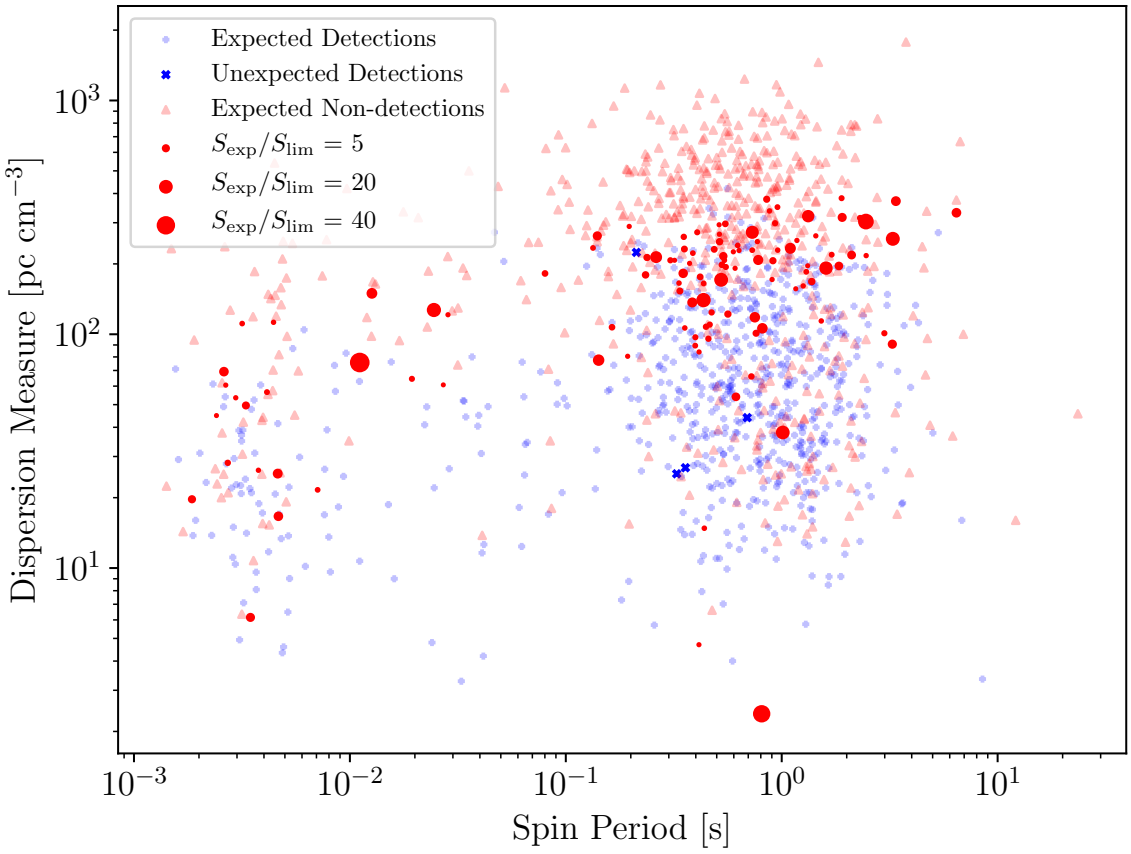

Figure 7. Period vs. DM for all included pulsars. Blue symbols indicate detections made by the survey, and red symbols indicate non-detections. Red triangles indicate missed pulsars that were not expected to be detected, in that they lie below the expected sensitivity of the survey. Red circles indicate missed pulsars that lie above their expected sensitivity, and so were unexpected non-detections (see §4.1 for details). Blue circles indicate detections that were expected, and blue x symbols indicate detection of pulsars with expected flux densities that were below our sensitivity limit. The area of these points is given by the ratio of expected flux density to the limiting flux density at the pulsar's position.

near the Galactic plane, but also visible are many individual pointings within the completed regions where significant RFI masking has reduced sensitivity. To mitigate this, these beams will be scheduled for reobserving. There is a small discrepancy between the number of observed beams displayed in Figures 1 and 9 due to a backlog of data which has yet to processed, and so mask fractions have not been determined for these beams.

4.3. *Nulling/Mode-Changing Candidates*

The large set of data analyzed in this study as well as the "by-eye" verification of all detections allowed for easy identification of potential nulling/mode-changing candidates in the results. This way, we are sensitive to nulling timescales between that of the pulsar spin period and the observation time (120 seconds). These cases were first identified by the appearance of missing pulses in the time-phase plots from processing using the `PRESTO` package. When a pulsar was noted as a candidate, we

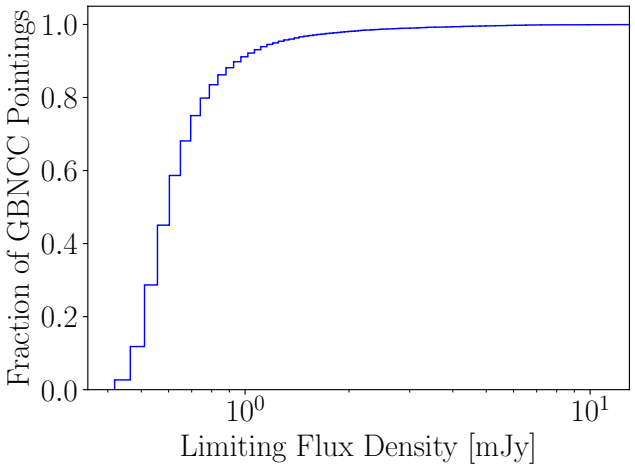

Figure 8. Cumulative histogram of limiting flux density for GBNCC. The mean and median limiting flux densities in the histogram 0.74 mJy and 0.62 mJy, and the values range from 0.42 mJy to 47. mJy. All flux density values are given in mJy.

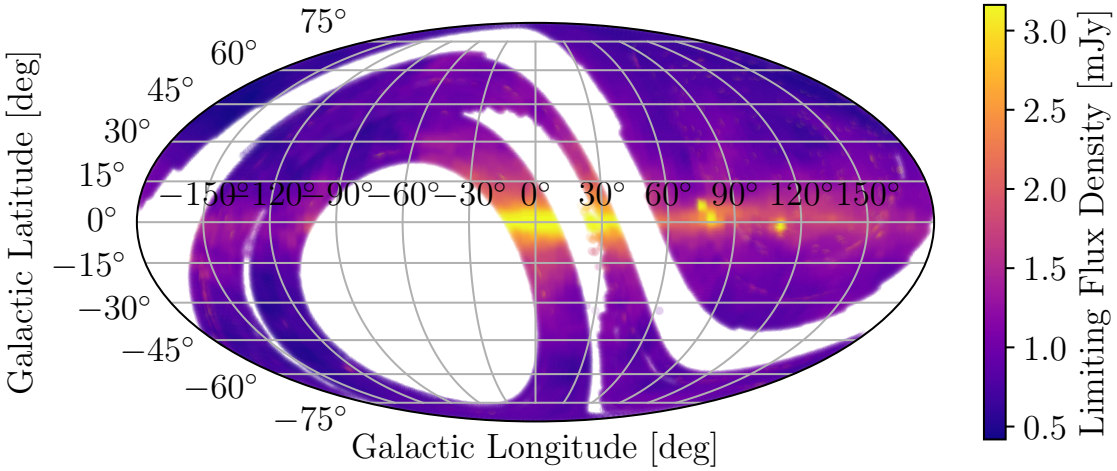

Figure 9. Sky map of GBNCC beams, colored by limiting flux density. The map is plotted in Galactic coordinates on a Mollweide projection, and the flux density is given in mJy.

followed up using the `dspsr`[4] package. We folded the time series data in 10 second integrations, zapped remaining RFI by hand, and integrated across frequency using the `pav` and `pam` commands within `PSRCHIVE`[5]. When it was possible to discern on- and off-pulse regions by eye (i.e. significant changes in intensity for some rotations), the candidates were considered likely to be nulling. Some pulsars exhibited behavior similar to mode-changing, where multiple components of the averaged profile were found to be on during different portions of the observation. These pulsars were not treated differently than other nulling candidates – we folded for single pulses to determine the likelihood that different components were visible. All of these sources will be followed up in later works regarding these data. In total, 223 pulsars were found to exhibit intensity variations similar to nulling or mode-changing during their observations, 62 of which have not previously been found to to do so. These candidates' names are marked in Table 4 with an asterisk.

[4] http://dspsr.sourceforge.net/index.shtml
[5] http://psrchive.sourceforge.net/index.shtml

4.4. *The Galactic Pulsar Population*

Given its overall sky coverage and the large number of pulsar detections reported here (670), the GBNCC survey will play an important role in future understanding of the Galactic pulsar population. To date, the GBNCC survey has detected 571 non-recycled (long-period) pulsars in the Galactic field and 70 Galactic MSPs, which have undergone recycling and have spin periods, $P < 30$ ms. Remaining detections are either associated with globular clusters (3) or are recycled pulsars with spin periods, $P > 30$ ms (26), and have been intentionally ignored for the following analysis, since our current models do not adequately describe the features of this sub-population.

To estimate expected numbers of non-recycled/millisecond pulsar detections in the GBNCC survey, Galactic populations were simulated using PsrPopPy2[6], a more recent and currently-maintained version of PsrPopPy (Bates et al. 2014, and citations within). Pulsar populations were generated using PsrPopPy2's `populate`

[6] https://github.com/devanshkv/PsrPopPy2

function, which simulates pulsars by drawing parameters from predefined distributions until some condition is met. Due to its large sample size, population estimates from the Parkes Multibeam Pulsar Survey (PMPS) provide the best-known sample parameters. For this reason, these results were used to set a limit on the number of pulsars simulated by `populate`. For the non-recycled pulsar population, pulsars were generated until a synthetic PMPS "detected" 1038 sources; for MSPs, the desired population size was set to 30,000 sources. Specific parameters defining pulsars' Galactic radial distribution, as well as scale height, spin period, luminosity, and duty cycle can be found in Swiggum et al. (2014). However, an updated model for the MSP P-distribution (Lorimer et al. 2015) was implemented in simulations here.

Synthetic surveys were conducted with 100 realizations each of the Galactic non-recycled/millisecond pulsar populations using `survey` and a GBNCC model file, including survey parameters identical to those presented in §2 and lists of completed/remaining GBNCC pointing positions. In the first round of simulations, we fixed the S/N limit for detections to $\mathrm{S/N_{cut}} = 3.8$ (as determined in §4.1). This simulation predicted 1442/126 simulated detections for non-recycled/millisecond pulsar populations, respectively (on average; compared to 571/70 actual detections). We then fixed the number of simulated non-recycled/millisecond pulsar detections to their actual values (571/70) and found nominal S/N thresholds for each sub-population, $\mathrm{S/N_{cut}} = 15.3/9.1$. The discrepancies between simulated and actual yields suggest uncertainties in population parameters informed primarily by the PMPS survey, which targeted the Galactic plane and was conducted at 1.4 GHz. Population parameters determined by these previous surveys produce over-estimates for GBNCC pulsar yields. As an all-sky, low-frequency search, the GBNCC survey (when complete) will be a valuable counterpoint to further refine non-recycled/millisecond pulsar population parameters. As we will show below, positional and rotational parameters of the simulated populations do not match the detected population when these thresholds are set.

To test the validity of underlying non-recycled/millisecond pulsar populations, we compared cumulative distribution functions (CDFs) of simulated (`sim`) pulsar parameters (P, DM, S_{350}, and b) with those of the actual (`act`) detections using a `scipy` implementation of the 2-sample Kolmogorov–Smirnov (K-S) test. For each parameter, the K-S test statistic and p-value were computed over a range of $\mathrm{S/N_{cut}}$. When $p < 1\%$, the null hypothesis (that `act`/`sim` parameters are drawn from the same underlying distribution) is rejected. Figures 10 and 11 illustrate these comparisons for non-recycled and millisecond pulsar population parameter distributions, and Table 3 summarizes K-S test results when the nominal $\mathrm{S/N_{cut}}$ values for non-recycled/millisecond pulsar sub-populations (15.3/9.1) are implemented, though we measured these p-values for a range of imposed $\mathrm{S/N_{cut}}$ values.

Table 3. K-S test statistics and p-values resulting from comparisons between actual/simulated parameter distributions for non-recycled/millisecond pulsars. In cases where the p-value is $< 1\%$, the null hypothesis (that the two distributions are the same) is rejected.

Parameter	Normal[a]		MSP[b]	
	K-S	$p(\%)$	K-S	$p(\%)$
Spin Period (P)	0.20	$\ll 1$	0.14	10
Dispersion Measure (DM)	0.21	$\ll 1$	0.26	< 1
Flux Density (S_{350})	0.13	$\ll 1$	0.21	< 1
Galactic Latitude (b)	0.04	41	0.17	3

[a] For simulated non-recycled pulsars, $\mathrm{S/N_{cut}} = 15.3$.

[b] For simulated MSP population, $\mathrm{S/N_{cut}} = 9.1$.

Comparing `act`/`sim` parameters for the non-recycled pulsar population, we find broad agreement between b distributions, regardless of $\mathrm{S/N_{cut}}$. Results for other non-recycled pulsar parameters in Table 3 show significant inconsistencies between `act`/`sim` samples. DM distributions are clearly different for $\mathrm{S/N_{cut}} > 4$, likely due to an over-abundance of low-DM simulated detections. For $\mathrm{S/N_{cut}} = 15.3$, we find twice as many `sim` detections with DM $< 35\,\mathrm{pc\,cm^{-3}}$. Presumably due to the prevalence of nearby `sim` sources, this sample also has a larger fraction of high-flux density sources, so S_{350} distributions are statistically different for $\mathrm{S/N_{cut}} = 15.3$. However, there is a small window ($10.25 < \mathrm{S/N_{cut}} < 12.25$) where `act`/`sim` S_{350} distributions become statistically similar, with $p > 1\%$. The null hypothesis is rejected for P due to `act`/`sim` log-normal distributions having different mean values: $\langle \log P_{\mathrm{act}} \rangle = 2.88$ versus $\langle \log P_{\mathrm{sim}} \rangle = 2.72$ (see Figure 10). This discrepancy persists, regardless of chosen $\mathrm{S/N_{cut}}$.

Because the simulated versions of the non-recycled pulsar population were primarily informed by PMPS (e.g. Lorimer et al. 2006), which was conducted at 1.4 GHz and exclusively covered regions of sky near the Galactic plane ($|b| < 5\,^\circ$), we expect there to be bias toward highly dispersed pulsars near the plane. Due to more uniform sky coverage and – near the Galactic plane – higher sky temperatures and more signif-

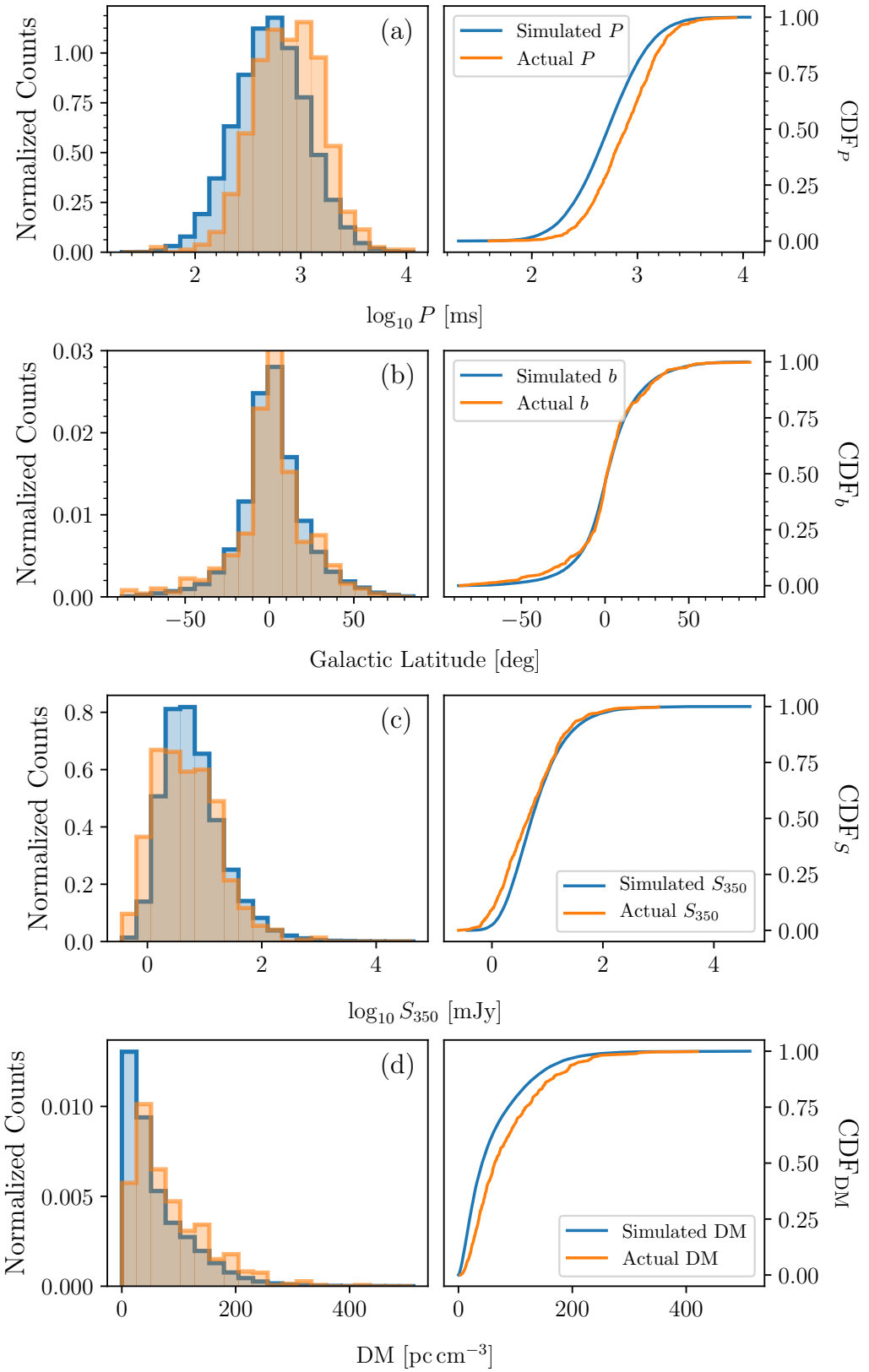

Figure 10. Normalized histograms showing comparisons between (a) spin period, P, (b) Galactic latitude, b, (c) flux density, S_{350}, and (d) dispersion measure, DM, distributions for simulated non-recycled pulsars (blue) and actual detections (orange). The rightmost panel in each row compares actual/simulated CDFs for each parameter. K-S tests comparing these CDFs (see Table 3 for details) show disagreement between `act`/`sim` P, S_{350}, and DM distributions, but $p = 41\%$ for b distributions.

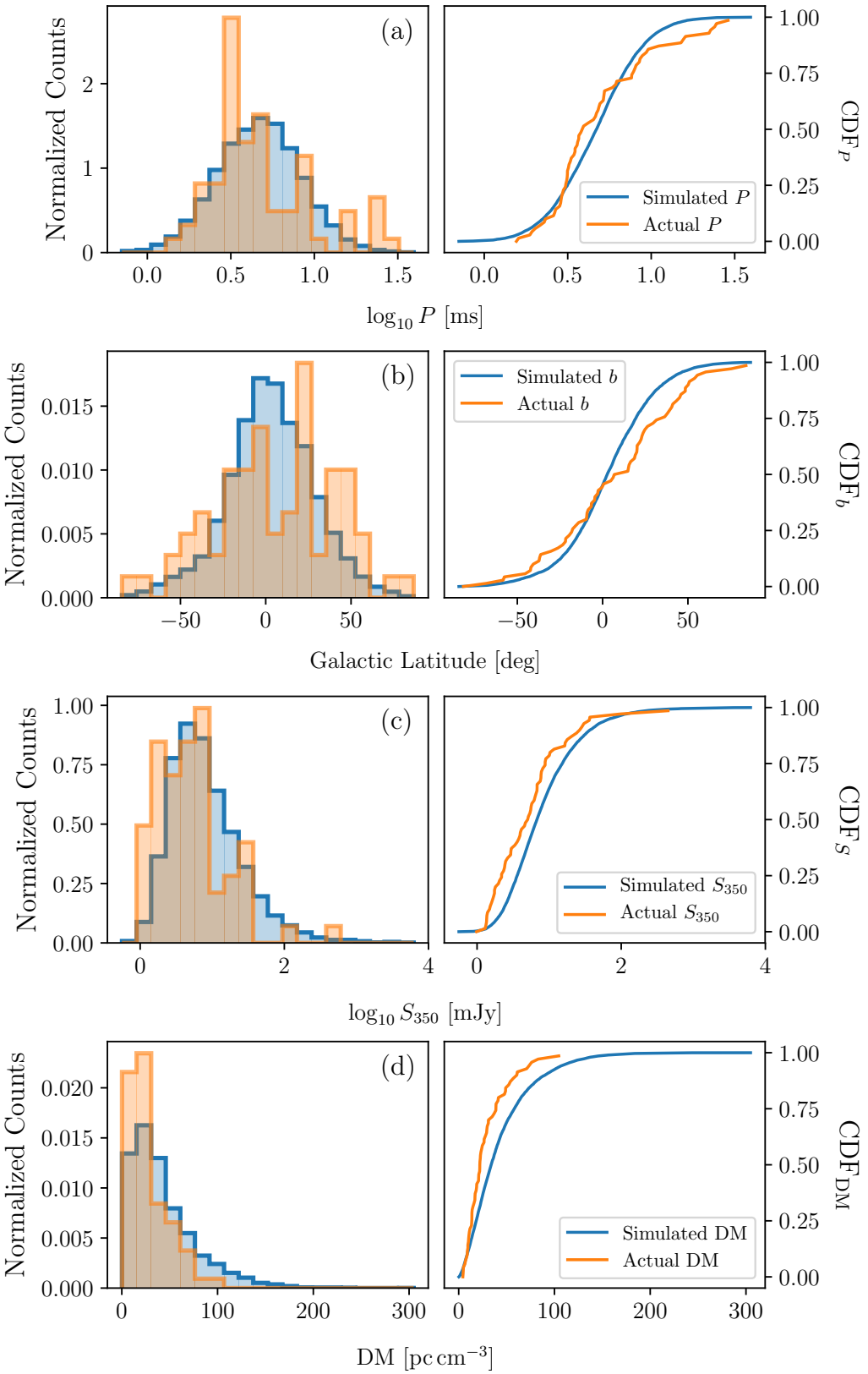

Figure 11. Normalized histograms showing comparisons between (a) spin period, P, (b) Galactic latitude, b, (c) flux density, S_{350}, and (d) dispersion measure, DM, distributions for simulated millisecond pulsars (blue) and actual detections (orange). The rightmost panel in each row compares actual/simulated CDFs for each parameter. K-S tests comparing these CDFs (see Table 3 for details) show disagreement between `act/sim` S_{350} and DM distributions, but distributions for b and P have $p = 3\%$ and 10%, respectively.

icant scattering at 350 MHz, the majority of GBNCC detections (67%) are away from the plane ($|b| > 5°$). Young pulsars are typically born in the plane and tend to be found nearby, therefore GBNCC's reduced sensitivity to low-latitude sources means that relatively few detections are young pulsars. The P-$\dot{P}$ diagram in Figure 12 nicely illustrates this shortage of pulsars detected with characteristic ages, $\tau \leq 1$ Myr. By imposing an age cutoff on non-recycled pulsars in the ATNF catalog, $\tau > 1$ Myr, the resulting simulated spin period distribution is statistically similar to that of GBNCC detections (K-S $p > 1\%$). This selection effect accounts for the apparent differences between `act`/`sim` P-distributions, but can not explain discrepancies in S_{350} and DM distributions for non-recycled pulsars.

K-S tests comparing `act`/`sim` parameter distributions for the MSP population show better agreement (see Table 3 and Figure 11). For MSPs, selection effects based on Galactic latitude and spin period do not come into play since MSPs are more isotropically distributed and model parameters for this sub-population are based on results from multiple Parkes Telescope surveys (see Lorimer et al. (2015), and references therein). For these reasons, the simulated population's spin periods are statistically similar to the sample detected by GBNCC. This conclusion does not change, regardless of the chosen S/N_{cut} value. For b, the null hypothesis is still not rejected by our criteria ($p < 1\%$). Based on the b histograms themselves, there appears to be an absence of detections in the `act` sample in/near the Galactic plane, which is not the case for `sim` sources. The null hypothesis is rejected for S_{350} due to the over-abundance of high-flux-density sources in the `sim` sample compared to those present in the `act` sample. Median flux densities for `act`/`sim` detections are 4.9/6.8 mJy respectively. Comparing `act`/`sim` DM distributions, the `sim` sample consists of a higher fraction of high-DM MSPs and 12% of simulated detections have DMs in excess of the `act` maximum value, 104.5 pc cm^{-3}. This is likely related to the bias toward high-flux-density detections noted in S_{350} for `sim` MSPs mentioned above.

Based on discrepancies between predicted yields from simulations and actual numbers of detections by the GBNCC survey, it appears that model parameters need to be further refined in order to generate more realistic Galactic pulsar populations in the future. For now, we proceed with nominal S/N_{cut} values in order to estimate the GBNCC survey's future yields. In the remaining ≈21,000 pointings, we expect an additional 160/16 non-recycled/millisecond pulsar detections, or ≈ 60/5 discoveries, accounting for detectable known pulsars in regions of sky remaining (Manchester et al. 2005).

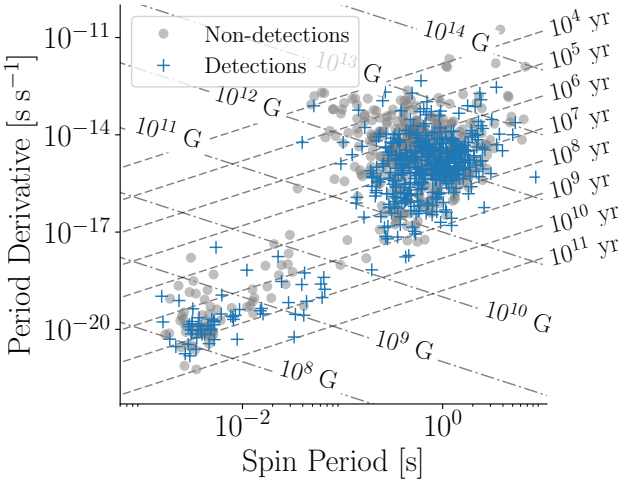

Figure 12. Period vs. period derivative for pulsars in GBNCC survey area. Shown in grey are pulsars that were not detected, and blue plus symbols show detections.

5. CONCLUSIONS

We have provided all detections of currently known pulsars that exist within the area of the 350 MHz GBNCC pulsar survey and performed some preliminary analysis of the resulting data set. Specifically, we have provided new flux density and pulse width measurements as well as pulse profiles for the 670 detections. When possible, we used our flux density measurements with previous measurements at different frequencies to refine spectral index. We also made a measurement of the spin period-pulse width relation, observing a powerlaw correlation of the form $W_{10} \propto P^{-0.27}$. The low frequency of the survey provides increased sensitivity to dispersion, allowing for more precise measurements of DM for many pulsars that have only been measured in high frequency surveys. Using all of this information, we have made quantitative measurements of the survey's efficacy and the RFI environment at 350 MHz, with a minimum detectable S/N of ∼3.8 and a mean limiting flux density of 0.74 mJy. These measurements have allowed us to make realistic predictions about the survey's yield when complete based on the detectability of known pulsars in the dataset, and we expect to detect on the order of 160 non-recycled pulsars and 15 MSPs. The simulations from which these expectations come uncovered discrepancies in DM, spin period, and spatial distribution in the Galaxy for the simulated populations which will be addressed in a future study. Combing through the data following processing has brought many interesting characteristics of pulsars in the survey to light, including 223 pulsars exhibiting evidence of variable intensities suggestive of nulling/mode-changing and 4 showing evidence for broken power-law spectral energy distribu-

tions. These kinds of qualitative observations pave the way for follow-up quantitative analyses of these data and the remaining beams that will be observed in the next few years.

ACKNOWLEDGEMENTS

We thank our anonymous referee for their suggestions and guidance. This work was supported by the NANOGrav Physics Frontiers Center, which is supported by the National Science Foundation award 1430284. The Green Bank Observatory is a facility of the National Science Foundation (NSF) operated under cooperative agreement by Associated Universities, Inc. R.S. acknowledges support through the Australian Research Council grant FL150100148. WF acknowledges the WVU STEM Mountains of Excellence Graduate Fellowship. MM and MS acknowledge the National Science Foundation OIA award number 1458952. JvL acknowledges funding from the European Research Council under the European Union's Seventh Framework Programme (FP/2007-2013) / ERC Grant Agreement n. 617199 ('ALERT'), and from Vici research programme 'ARGO' with project number 639.043.815, financed by the Netherlands Organisation for Scientific Research (NWO). VMK acknowledges the NSERC Discovery Grant, the Herzberg Award, FRQNT and CRAQ, Canada Research Chairs, CIFAR and the Webster Foundation Fellowship, and the Trottier Chair in Astrophysics and Cosmology. Computations were made on the supercomputer Guillimin at McGill University[7], managed by Calcul Quebec and Compute Canada. The operation of this supercomputer is funded by the Canada Foundation for Innovation (CFI), NanoQuebec, RMGA and the Fonds de recherche du Quebec - Nature et technologies (FRQ-NT). The CyberSKA project was funded by a CANARIE NEP-2 grant. PC acknowledges the FRQNT Doctoral Research Award. SMR is a CIFAR Senior Fellow. Pulsar research at UBC is supported by an NSERC Discovery Grant and by the Canada Foundation for Innovation.

Software: `Astropy` (Price-Whelan et al. 2018), `PRESTO` (Ransom 2001), `PsrPopPy2` (Bates et al. 2014), `SciPy` (Jones et al. 2001), `NumPy` (Oliphant 2006), `dspsr` (van Straten & Bailes 2011), `PSRCHIVE` (Hotan et al. 2004), `TEMPO` (http://tempo.sourceforge.net/)

Facilities: Robert C. Byrd Green Bank Telescope (GBT)

REFERENCES

1984, Birth and evolution of neutron stars: Issues raised by millisecond pulsars

Aloisi, R. J., et al. 2019, ApJ, in press, arXiv:1903.03543

Ashworth, M., & Lyne, A. G. 1981, MNRAS, 195, 517

Bailes, M., et al. 1997, ApJ, 481, 386

Barr, E. D., et al. 2013, MNRAS, 435, 2234

Bates, S. D., Lorimer, D. R., Rane, A., & Swiggum, J. 2014, MNRAS, 439, 2893

Bell, M. E., et al. 2016, MNRAS, 461, 908

Bhattacharyya, B., et al. 2013, ApJL, 773, L12

Biggs, J. D., Bailes, M., Lyne, A. G., Goss, W. M., & Fruchter, A. S. 1994, MNRAS, 267, 125

Bilous, A. V., et al. 2016, A&A, 591, A134

Boyles, J., et al. 2013, ApJ, 763, 80

Brinkman, C., Freire, P. C. C., Rankin, J., & Stovall, K. 2018, MNRAS, 474, 2012

Burgay, M., et al. 2006, MNRAS, 368, 283

—. 2013, MNRAS, 429, 579

Camilo, F. 1995, PhD thesis, PRINCETON UNIVERSITY.

Camilo, F., & Nice, D. J. 1995, ApJ, 445, 756

Camilo, F., Nice, D. J., Shrauner, J. A., & Taylor, J. H. 1996a, ApJ, 469, 819

Camilo, F., Nice, D. J., & Taylor, J. H. 1996b, ApJ, 461, 812

Champion, D. J., et al. 2005, MNRAS, 363, 929

Chandler, A. M. 2003, PhD thesis, CALIFORNIA INSTITUTE OF TECHNOLOGY

Chatterjee, S., Goss, W. M., & Brisken, W. F. 2005, ApJL, 634, L101

Chen, J. L., & Wang, H. G. 2014, ApJS, 215, 11

Coenen, T., et al. 2014, A&A, 570, A60

Cognard, I., et al. 2011, ApJ, 732, 47

Cordes, J. M., & Lazio, T. J. 1991, ApJ, 376, 123

Cordes, J. M., et al. 2006, ApJ, 637, 446

Costa, M. E., McCulloch, P. M., & Hamilton, P. A. 1991, MNRAS, 252, 13

Dembska, M., Kijak, J., Jessner, A., Lewandowski, W., Bhattacharyya, B., & Gupta, Y. 2014, MNRAS, 445, 3105

Deneva, J. S., Stovall, K., McLaughlin, M. A., Bates, S. D., Freire, P. C. C., Martinez, J. G., Jenet, F., & Bagchi, M. 2013, ApJ, 775, 51

[7] www.hpc.mcgill.ca

Dewey, R. J., Taylor, J. H., Weisberg, J. M., & Stokes, G. H. 1985a, ApJL, 294, L25
—. 1985b, ApJL, 294, L25
Fomalont, E. B., Goss, W. M., Lyne, A. G., Manchester, R. N., & Justtanont, K. 1992, MNRAS, 258, 497
Foster, R. S., Fairhead, L., & Backer, D. C. 1991, ApJ, 378, 687
Frail, D. A., Jagannathan, P., Mooley, K. P., & Intema, H. T. 2016, ApJ, 829, 119
Fruchter, A. S., et al. 1990, ApJ, 351, 642
Gomez-Gonzalez, J., & Guelin, M. 1974, A&A, 32, 441
Gould, D. M., & Lyne, A. G. 1998, MNRAS, 301, 235
Halpern, J. P., Camilo, F., Gotthelf, E. V., Helfand , D. J., Kramer, M., Lyne, A. G., Leighly, K. M., & Eracleous, M. 2001, ApJL, 552, L125
Han, J., Wang, C., Xu, J., & Han, J. 2017, arXiv e-prints, arXiv:1703.05988
Han, J., Wang, C., Xu, J., & Han, J.-L. 2016, Research in Astronomy and Astrophysics, 16, 159
Haslam, C. G. T., Klein, U., Salter, C. J., Stoffel, H., Wilson, W. E., Cleary, M. N., Cooke, D. J., & Thomasson, P. 1981, A&A, 100, 209
Hobbs, G., et al. 2004, MNRAS, 352, 1439
Hotan, A. W., van Straten, W., & Manchester, R. N. 2004, PASA, 21, 302
Hulse, R. A., & Taylor, J. H. 1975, ApJL, 201, L55
Jacoby, B. A., Bailes, M., Ord, S. M., Knight, H. S., & Hotan, A. W. 2007, ApJ, 656, 408
Jankowski, F., van Straten, W., Keane, E. F., Bailes, M., Barr, E. D., Johnston, S., & Kerr, M. 2018a, MNRAS, 473, 4436
—. 2018b, MNRAS, 473, 4436
Jankowski, F., et al. 2019, MNRAS, 484, 3691
Janssen, G. H., Stappers, B. W., Bassa, C. G., Cognard, I., Kramer, M., & Theureau, G. 2010, A&A, 514, A74
Janssen, G. H., Stappers, B. W., Braun, R., van Straten, W., Edwards, R. T., Rubio-Herrera, E., van Leeuwen, J., & Weltevrede, P. 2009, A&A, 498, 223
Johnston, S., & Karastergiou, A. 2019, MNRAS, 485, 640
Johnston, S., & Kerr, M. 2018, MNRAS, 474, 4629
Johnston, S., Lyne, A. G., Manchester, R. N., Kniffen, D. A., D'Amico, N., Lim, J., & Ashworth, M. 1992, MNRAS, 255, 401
Jones, E., Oliphant, T., Peterson, P., et al. 2001, SciPy: Open source scientific tools for Python, [Online; accessed ¡today¿]
Joshi, B. C., et al. 2009, MNRAS, 398, 943
Karako-Argaman, C., et al. 2015, ApJ, 809, 67
Kawash, A. M., et al. 2018, ApJ, 857, 131
Keane, E. F., et al. 2018, MNRAS, 473, 116
Keith, M. J., et al. 2010, MNRAS, 409, 619
Kondratiev, V. I., et al. 2016, A&A, 585, A128
Kramer, M., Lange, C., Lorimer, D. R., Backer, D. C., Xilouris, K. M., Jessner, A., & Wielebinski, R. 1999, ApJ, 526, 957
Kramer, M., Xilouris, K. M., Lorimer, D. R., Doroshenko, O., Jessner, A., Wielebinski, R., Wolszczan, A., & Camilo, F. 1998, ApJ, 501, 270
Kuzmin, A. D., & Losovsky, B. Y. 2001, A&A, 368, 230
Lazarus, P., et al. 2015, ApJ, 812, 81
Levin, L., et al. 2016, ApJ, 818, 166
Lewandowski, W., Wolszczan, A., Feiler, G., Konacki, M., & Sołtysiński, T. 2004, ApJ, 600, 905
Lommen, A. N., Zepka, A., Backer, D. C., McLaughlin, M., Cordes, J. M., Arzoumanian, Z., & Xilouris, K. 2000, ApJ, 545, 1007
Lorimer, D. 1994, PhD thesis, The University of Manchester
Lorimer, D. R., & Kramer, M. 2004, Handbook of Pulsar Astronomy
Lorimer, D. R., Lyne, A. G., & Camilo, F. 1998, A&A, 331, 1002
Lorimer, D. R., Yates, J. A., Lyne, A. G., & Gould, D. M. 1995a, MNRAS, 273, 411
Lorimer, D. R., et al. 1995b, ApJ, 439, 933
—. 2006, MNRAS, 372, 777
—. 2015, MNRAS, 450, 2185
Lynch, R. S., et al. 2013, ApJ, 763, 81
—. 2018, ApJ, 859, 93
Lyne, A. G., et al. 1998, MNRAS, 295, 743
Manchester, R. N., Hobbs, G. B., Teoh, A., & Hobbs, M. 2005, AJ, 129, 1993
Manchester, R. N., et al. 1996, MNRAS, 279, 1235
—. 2013, PASA, 30, e017
McLaughlin, M. A., et al. 2006, Nature, 439, 817
Mohanty, D. K. 1983, in IAU Symposium, Vol. 101, Supernova Remnants and their X-ray Emission, ed. J. Danziger & P. Gorenstein, 503
Murphy, T., et al. 2017, PASA, 34, e020
Navarro, J., Anderson, S. B., & Freire, P. C. 2003, ApJ, 594, 943
Nicastro, L., Lyne, A. G., Lorimer, D. R., Harrison, P. A., Bailes, M., & Skidmore, B. D. 1995, MNRAS, 273, L68
Nice, D. J., et al. 2013, ApJ, 772, 50
Oliphant, T. E. 2006, A guide to NumPy, Vol. 1 (Trelgol Publishing USA)
Price-Whelan, A. M., et al. 2018, AJ, 156, 123
Qiao, G., Manchester, R. N., Lyne, A. G., & Gould, D. M. 1995, MNRAS, 274, 572
Ransom, S. M. 2001, PhD thesis, Harvard University
Ransom, S. M., et al. 2011, ApJL, 727, L16

Ray, P. S., Thorsett, S. E., Jenet, F. A., van Kerkwijk, M. H., Kulkarni, S. R., Prince, T. A., Sand hu, J. S., & Nice, D. J. 1996, ApJ, 470, 1103

Sanidas, S., et al. 2019, A&A, 626, A104

Sayer, R. W., Nice, D. J., & Taylor, J. H. 1997, ApJ, 474, 426

Stairs, I. H., Thorsett, S. E., & Camilo, F. 1999, ApJS, 123, 627

Stokes, G. H., Segelstein, D. J., Taylor, J. H., & Dewey, R. J. 1986, ApJ, 311, 694

Stovall, K., et al. 2014, ApJ, 791, 67

—. 2015, ApJ, 808, 156

Surnis, M. P., Joshi, B. C., McLaughlin, M. A., Krishnakumar, M. A., Manoharan, P. K., & Naidu, A. 2019, ApJ, 870, 8

Swiggum, J. K., et al. 2014, ApJ, 787, 137

—. 2017, ApJ, 847, 25

Taylor, J. H., Manchester, R. N., & Lyne, A. G. 1993, ApJS, 88, 529

Toscano, M., Bailes, M., Manchester, R. N., & Sand hu, J. S. 1998, ApJ, 506, 863

Tyul'bashev, S. A., Tyul'bashev, V. S., Oreshko, V. V., & Logvinenko, S. V. 2016, Astronomy Reports, 60, 220

van Straten, W., & Bailes, M. 2011, PASA, 28, 1

Wolszczan, A., & Frail, D. A. 1992, Nature, 355, 145

Xue, M., et al. 2017, PASA, 34, e070

APPENDIX

In Table 4 we list the measured quantities of DM, pulse width, S/N, S_{350}, and α. We include the references to papers from which measurements of flux density at other frequencies were taken to determine α in the table footnotes. Pulse profiles are shown in Figures 13–24.

Table 4. Pulsar Detections in the GBNCC Survey.

PSR[a]	PSR B	DM	MJD	θ	W_{50}	W_{10}	S/N	S_{350}	α	Refs.
		(pc/cm^3)		(deg)	(ms)	(ms)		(mJy)		
J0014+4746*	B0011+47	30.2(3)	55538	0.227	109	175	29.6(5)	5.0(8)	−1.0(7)	1,2
J0025−19[B]	···	21.3(3)	58079	0.002	39	95	51.3(15)	3.8(7)	···	···
J0026+6320	···	244.7(8)	55198	0.196	23	48	16.6(9)	4.7(5)	−1.12(9)	3,4
J0030+0451	···	4.335(5)	58229	0.086	0.7	1	41.2(13)	6.8(14)	−2.4(5)	5,6,7
J0033+57	···	75.65(8)	55325	0.389	8	18	29.4(15)	9.1(12)	···	···
J0033+61	···	37.6(2)	55249	0.303	16	25	12.(2)	1.7(4)	···	···
J0034−0534	···	13.76(19)	57380	0.253	0.7	0.8	103.7(18)	36.(7)	†	···
J0034−0721*	B0031−07	10.9(2)	57387	0.277	62	106	184.(8)	28.(5)	−2.4(4)	8,9,10,2,11,12
J0034+69	···	80.01(14)	55169	0.024	1	2	22.(6)	2.5(7)	···	···
J0038−25[B]	···	5.7(6)	56774	0.007	6	23	70.9(6)	5.0(10)	···	···
J0040+5716	B0037+56	92.5(2)	55325	0.207	13	26	76.0(10)	5.7(8)	−1.59(17)	1,2
J0048+3412*	B0045+33	40.0(3)	56025	0.244	17	36	19.0(17)	2.0(5)	−2.65(4)	13,1,2
J0051+0423	···	13.93(9)	58229	0.174	11	34	31.3(15)	2.1(4)	−2.3(14)	1,14,12
J0053+69	···	116.7(2)	55169	0.017	13	30	32.5(7)	2.5(3)	···	···
J0055+5117*	B0052+51	43.8(5)	55405	0.286	16	73	16.3(7)	1.2(2)	−0.7(4)	1,2
J0056+4756	B0053+47	17.93(12)	55538	0.236	12	31	21.5(16)	2.5(4)	−2.0(2)	1,2
J0058+6125	···	128.3(16)	55249	0.226	7	17	19.3(6)	2.0(2)	···	···
J0059+50	···	66.8(2)	55531	0.000	38	49	27.1(10)	1.8(3)	···	···
J0100+69[L]	···	63.5[‡]	55163	0.255	11	59	13.(7)	2.1(12)	···	···
J0102+6537*	B0059+65	65.8(4)	55188	0.237	16	66	24.1(12)	2.6(3)	−0.7(7)	1,2
J0103+54*	···	55.49(9)	55353	0.359	6	13	11.5(18)	1.8(3)	···	···
J0104+64[B]	···	44.6(3)	55188	0.008	45	82	6.0(15)	0.69(19)	···	···
J0108+6608	B0105+65	30.4(3)	55180	0.053	73	142	71.5(9)	11.6(13)	−1.65(7)	1,2
J0108+6905*	B0105+68	61.1(2)	55169	0.185	11	65	17.5(18)	1.3(2)	−1.3(3)	1,2
J0110−22[B]	···	20.8(3)	56593	0.012	42	64	22.0(12)	1.1(2)	···	···
J0112+66*	···	111.6(11)	55188	0.007	32	86	17.5(5)	1.10(14)	···	···
J0117+5914	B0114+58	49.4(2)	55253	0.301	3	7	40.8(13)	9.4(11)	−2.35(6)	1,2
J0121+14[L]	···	17.8[‡]	58347	0.291	21	44	10(10)	1.4(11)	···	···
J0125−23[B]	···	9.59(3)	56718	0.000	0.7	1	37.1(17)	5.5(11)	···	···
J0125+62	···	118.0(4)	55200	0.003	17	60	10.8(12)	0.99(15)	···	···
J0134−2937	···	21.8(3)	56898	0.177	5	12	63.9(12)	6.0(12)	−0.2(10)	15,11,12
J0136+63	···	285.8(18)	55197	0.007	24	57	11.9(14)	1.7(2)	···	···

Table 4 continued

Table 4 *(continued)*

PSR[a]	PSR B	DM (pc/cm^3)	MJD	θ (deg)	W_{50} (ms)	W_{10} (ms)	S/N	S_{350} (mJy)	α	Refs.
J0139+5621	···	102.4(4)	55325	0.302	35	63	7.0(8)	0.90(16)	−1.9(3)	1,16
J0139+5814*	B0136+57	73.84(7)	55254	0.153	5	9	175.9(18)	14.5(19)	−1.4(2)	1,2
J0141+6009*	B0138+59	34.7(3)	55250	0.245	34	97	128.(2)	26.(3)	−1.22(19)	8,1,2
J0141+63	···	272.8(18)	55197	0.006	2	4	6.(3)	1.1(6)	···	···
J0147+5922	B0144+59	40.08(5)	55253	0.315	6	9	33.4(7)	6.7(8)	−1.18(14)	1,2
J0151−0635*	B0148−06	25.5(3)	57387	0.049	58	79	47.4(16)	4.3(8)	−1.1(9)	6,2,11,12
J0152−1637	B0149−16	12.0(2)	57880	0.151	18	30	208.5(11)	11.(2)	−1.68(7)	8,6,2,11,12
J0156+3949	B0153+39	58.4(4)	55657	0.313	99	159	16.(2)	3.2(7)	−0.8(6)	1,2
J0157+6212	B0154+61	30.1(6)	55200	0.159	40	74	35.2(19)	3.6(4)	−0.3(3)	1,2
J0201+7005	···	21.0(3)	55163	0.326	11	49	6.1(17)	1.1(3)	···	···
J0212+5222	···	38.27(9)	55353	0.180	13	20	14.(2)	1.3(2)	−1.2(13)	1,17,18
J0214+5222	···	22.05(9)	55353	0.248	1	3	11.5(7)	2.4(3)	−2.8(6)	1,17
J0215+6218	···	84.65(14)	55200	0.278	41	105	14.7(9)	6.9(8)	−0.(2)	17,19
J0218+4232	···	61.23(2)	55624	0.255	1	1	48.(2)	28.(4)	†	···
J0231+7026	B0226+70	46.5(3)	55163	0.241	35	47	32.(4)	3.6(7)	−1.75(6)	1,2
J0242+62*	···	3.91(15)	55197	0.087	18	39	78.4(16)	9.6(11)	···	···
J0243+6027*	···	141.0(3)	55250	0.075	35	82	16.3(15)	2.3(3)	···	···
J0301+35[A]	···	57.43(14)	55984	0.147	5	11	12.2(14)	0.63(14)	···	···
J0323+3944	B0320+39	26.3(7)	55654	0.129	45	81	211.9(5)	11.2(18)	−1.87(16)	8,13,1,2
J0324+5239	···	115.3(8)	55352	0.243	13	21	10.(2)	1.7(5)	−1.558(6)	20,18
J0325+67*	···	64.9(3)	55171	0.007	14	26	25.3(11)	1.30(19)	···	···
J0332+5434*	B0329+54	26.76(18)	55348	0.451	7	19	610(10)	510(60)	−0.7(14)	8,2
J0335+4555	B0331+45	47.26(6)	55559	0.177	6	10	8.(7)	0.8(6)	−1.0(2)	1,2
J0335+6623	···	66.6(4)	55179	0.000	30	52	23.5(7)	1.4(2)	···	···
J0341+5711	···	101.0(4)	55279	0.150	43	75	26.(5)	2.6(6)	···	···
J0343+06[A]	···	46.0(2)	58228	0.266	32	65	9.4(14)	1.0(2)	···	···
J0343−3000	···	20.2(6)	56844	0.106	38	98	7.9(8)	0.38(13)	···	···
J0343+5312*	B0339+53	67.5(4)	55348	0.238	43	72	54.6(8)	6.6(8)	−2.0(10)	2
J0348+0432	···	40.46(15)	58233	0.311	2	5	8.(2)	1.8(6)	−1.0(2)	1,21
J0355+28[B]	···	48.68(9)	56277	0.001	8	17	14.5(10)	0.81(16)	···	···
J0357+5236	B0353+52	103.7(5)	55504	0.104	13	27	49.1(3)	9.8(11)	−1.32(19)	2
J0358+42*	···	46.27(5)	55629	0.002	10	15	23.9(14)	2.2(3)	···	···
J0358+5413*	B0355+54	57.12(4)	55343	0.208	3	9	110.7(5)	15.2(19)	−0.7(7)	8,1,2
J0358+66	···	62.27(2)	55179	0.001	2	4	10.(2)	0.8(2)	···	···
J0405+3347[B]	···	53.3(16)	56156	0.005	2	5	7.1(4)	0.42(7)	···	···
J0406+30[B]	···	49.37(2)	56277	0.008	0.2	0.6	26.1(2)	3.7(6)	···	···
J0406+6138*	B0402+61	65.32(15)	55237	0.092	19	32	157.5(7)	14.2(18)	−1.30(4)	1,2
J0408+552	···	63.76(19)	55343	0.418	47	88	23.(4)	15.(3)	···	···
J0410−31*	···	8.9(4)	56902	0.470	25	49	44.(3)	7.8(19)	···	···
J0413+58	···	57.0(17)	55263	0.435	21	55	8.(4)	4.(2)	···	···

Table 4 continued

Table 4 *(continued)*

PSR[a]	PSR B	DM	MJD	θ	W_{50}	W_{10}	S/N	S_{350}	α	Refs.
		(pc/cm^3)		(deg)	(ms)	(ms)		(mJy)		
J0414+31[B]	···	64.1(2)	56184	0.000	19	49	12.(3)	0.7(2)	···	···
J0415+6954	B0410+69	27.44(19)	55163	0.052	4	11	112.0(5)	6.0(9)	−1.7(5)	1,2
J0417+35	···	48.63(16)	55683	0.252	8	17	19.1(13)	1.6(2)	···	···
J0417+61	···	70.14(11)	55249	0.033	19	38	6.8(11)	0.82(17)	···	···
J0421−0345	···	44.3(5)	57154	0.191	27	47	53.6(7)	2.7(7)	−1.8(12)	15,22
J0426+4933	···	84.2(2)	55538	0.241	13	27	12.1(14)	1.4(2)	−1.4785(14)	1,18
J0448−2749*	···	26.22(11)	56809	0.251	6	18	14.6(13)	1.0(2)	0.2(19)	23,24,12
J0450−1248	B0447−12	37.0(11)	57122	0.262	18	30	107.7(7)	10.(2)	−1.64(19)	2,11,12
J0452−1759*	B0450−18	39.9(14)	58058	0.036	29	39	550(10)	43.(9)	−0.8(15)	2,11,12
J0454+5543*	B0450+55	14.59(8)	55343	0.154	10	30	190.(3)	24.(3)	−0.8(2)	8,1,2
J0458−0505*	···	47.8(4)	57379	0.162	17	39	26.(3)	1.2(3)	···	···
J0459−0210	···	21.0(2)	57662	0.271	15	75	29.1(10)	3.4(6)	−2.0(9)	1,15,12
J0502+4654	B0458+46	42.38(16)	55552	0.078	24	59	52.3(13)	8.5(10)	−1.2(2)	20,2
J0510+38	···	69.11(19)	55658	0.003	4	11	15.9(14)	2.5(3)	···	···
J0519+54	···	42.55(8)	55343	0.004	9	20	14.2(5)	1.22(17)	···	···
J0520−2553	···	33.77(6)	56776	0.144	2	13	55.9(5)	2.8(6)	−1.(4)	23,24,12
J0530−39[B]	···	48.5(2)	56998	0.012	33	42	22.9(8)	1.1(2)	···	···
J0533+0402*	···	83.9(2)	58251	0.319	16	32	42.3(4)	4.6(7)	−1.0(2)	1,14,11,12
J0534−13[B]	···	74.3(2)	57149	0.071	13	38	20.2(17)	1.0(2)	···	···
J0540+3207*	···	62.08(13)	56478	0.140	9	16	104.2(5)	6.7(10)	−1.98(5)	1,25
J0555+3948	···	36.1(2)	55650	0.323	26	52	15.3(15)	2.3(4)	···	···
J0557−2948	···	49.05(17)	56835	0.012	0.7	2	18.1(17)	0.9(2)	···	···
J0601−0527*	B0559−05	80.58(12)	57380	0.133	12	26	139.9(4)	12.(2)	−1.7(2)	2,26,11,12
J0608+00	···	48.4(2)	57755	0.079	17	30	20.(2)	1.1(2)	···	···
J0610−2100	···	60.7(3)	56592	0.100	0.6	0.8	17.3(7)	2.1(4)	···	···
J0610+37	···	39.09(11)	55682	0.451	12	25	19.6(6)	7.8(14)	···	···
J0611+1436	···	43.99(6)	58355	0.225	16	33	9.(3)	2.0(8)	···	···
J0612+3721	B0609+37	27.12(7)	55682	0.313	7	18	82.9(10)	12.(2)	0.0(7)	1,2
J0613−0200	···	38.77(3)	57791	0.289	0.3	0.7	29.(2)	8.8(17)	−1.60(16)	5,27,28,29
J0613+3731	···	18.78(15)	55682	0.213	10	27	15.(2)	1.6(3)	−2.7(6)	1,16
J0614−3329	···	37.04(3)	56957	0.192	0.4	0.6	18.6(10)	2.6(6)	···	···
J0614+83*	···	44.2(2)	55148	0.004	11	81	14.3(9)	1.0(2)	···	···
J0621+0336	···	72.53(6)	58355	0.190	4	7	49.8(6)	3.3(5)	−1.5(9)	1,30
J0624−0424*	B0621−04	70.9(2)	57154	0.162	24	78	51.9(10)	6.4(10)	−1.00(6)	1,2,26,12
J0627+0649	···	86.6(8)	58202	0.234	9	18	27.5(15)	3.4(5)	···	···
J0627+0706*	···	138.2[‡]	58202	0.186	7	31	60.1(11)	7.4(10)	−1.44(13)	1,31,32,26,11
J0630−0046	···	97.89(17)	57540	0.069	11	36	11.0(14)	1.6(5)	···	···
J0630−2834	B0628−28	34.4(3)	56777	0.058	72	143	349.(4)	39.(8)	−1.4(4)	8,9,10,2,26,11,12
J0636−23[B]	···	59.12(12)	56666	0.000	14	27	11.(2)	0.65(19)	···	···
J0636+5129	···	11.11(2)	55442	0.147	0.2	0.3	12.1(3)	1.5(2)	−1.1(2)	33,17

Table 4 continued

Table 4 *(continued)*

PSR[a]	PSR B	DM	MJD	θ	W_{50}	W_{10}	S/N	S_{350}	α	Refs.
		(pc/cm^3)		(deg)	(ms)	(ms)		(mJy)		
J0645+5158	···	18.24(9)	55366	0.135	0.3	0.6	36.8(6)	2.9(5)	−2.2(6)	1,17,34
J0645+80	···	49.71(16)	55146	0.011	32	52	30.5(10)	2.1(4)	0.(2)	1,17
J0648−27[B]	···	132.5(10)	56777	0.005	54	115	18.5(7)	0.75(15)	···	···
J0652−0142*	···	117.3(2)	57763	0.129	9	24	15.5(8)	1.3(2)	···	···
J0653+8051*	B0643+80	33.1(3)	55146	0.131	18	40	92.3(10)	4.5(8)	−1.2(4)	1,2
J0656−2228*	···	31.8(3)	56655	0.174	27	52	11.4(13)	0.85(17)	0.(2)	26
J0659+1414*	B0656+14	14.1(9)	58356	0.227	14	34	33.5(9)	3.9(7)	−0.52(5)	1,2,26,11
J0659−36[B]	···	83.37(16)	56987	0.013	13	35	7.1(10)	0.42(18)	···	···
J0700+6418	B0655+64	8.76(5)	55226	0.201	5	9	149.9(4)	12.(2)	−2.8(2)	8,1,2
J0709+05[A]	···	44.23(13)	58201	0.084	3	4	7.(2)	0.8(3)	···	···
J0719−2545*	···	254.4(2)	56771	0.157	83	163	26.7(4)	4.1(6)	···	···
J0721−2038	···	76.01(6)	58107	0.153	0.4	3	9.8(11)	2.1(4)	−1.7(2)	26
J0725−1635	···	99.02(19)	57854	0.115	7	14	16.7(8)	1.2(2)	−1.(5)	15,35
J0726−2612	···	69.4[‡]	56771	0.290	56	103	10.9(7)	1.2(2)	···	···
J0729−1448*	···	91.89(6)	57854	0.192	8	15	29.(2)	3.5(6)	−1.4(4)	26
J0729−1836*	B0727−18	61.34(13)	56993	0.080	6	30	98.9(10)	8.6(13)	−1.2(2)	2,26,11
J0733−2345	···	190.2(4)	56722	0.203	20	69	8.6(16)	0.79(19)	···	···
J0737−2202	···	95.59(8)	56663	0.160	11	28	19.7(12)	2.3(3)	···	···
J0737−3039A	···	48.9(9)	56902	0.307	1	4	68.7(7)	26.(4)	−1.59(17)	33,11,36,37
J0737+69*	···	15.5(17)	55173	0.008	60	154	67.(4)	2.2(4)	···	···
J0740+41	···	20.82(3)	55630	0.046	0.6	1	11.1(10)	2.0(4)	···	···
J0740+6620	···	14.95(2)	55189	0.133	0.2	0.9	42.3(7)	7.8(14)	···	···
J0742−2822	B0740−28	73.78(4)	56778	0.214	5	9	910(20)	130(20)	−1.1(5)	10,2,26,11
J0746+66*	···	27.7(15)	55189	0.010	5	20	10.(3)	0.7(2)	···	···
J0750+57*	···	26.7(3)	55290	0.007	13	104	18.9(3)	1.5(2)	−0.7(14)	1,17
J0754+3231*	B0751+32	39.8(3)	56278	0.218	13	104	41.0(5)	3.6(7)	−1.74(16)	13,1,2
J0758−1528	B0756−15	63.25(17)	57150	0.056	8	15	93.8(12)	3.8(7)	−1.1(8)	2,26,11
J0758−30[B]	···	86.4(2)	56784	0.000	27	49	27.2(12)	1.6(2)	···	···
J0804−3647*	···	187.6(5)	56969	0.239	37	76	26.4(5)	3.3(6)	···	···
J0808−3937	···	169.1(2)	56991	0.270	13	30	10.(2)	1.1(3)	···	···
J0812−3905	···	329.6(12)	56973	0.267	6	62	13.2(13)	3.0(5)	−1.4(14)	26
J0814+7429	B0809+74	5.8(3)	55171	0.118	47	93	143.6(13)	9.1(18)	−1.4(17)	8,20,2
J0815+4611[L]	···	11.09(11)	55508	0.227	13	20	35.(6)	2.5(7)	···	···
J0818−3049	···	118.9(2)	56779	0.229	46	63	22.(2)	2.8(5)	−1.5(4)	26
J0818−3232*	···	132.5(5)	56813	0.328	42	60	17.4(11)	2.0(3)	−1.1(18)	26
J0820−1350	B0818−13	41.0(3)	57096	0.128	22	38	610(20)	42.(9)	−1.4(2)	8,10,2,26,11
J0820−3826	···	195.5(3)	56971	0.110	8	16	14.(3)	2.2(6)	−1.7(4)	26
J0820−3921*	···	179.9(2)	56973	0.074	46	107	39.0(9)	8.1(11)	···	···
J0823+0159	B0820+02	23.9(2)	57688	0.179	22	37	170.0(17)	8.(2)	−1.3(3)	1,10,2,26
J0826+2637	B0823+26	19.53(13)	56529	0.067	7	16	376.(7)	31.(7)	−1.5(3)	8,13,1,2

Table 4 continued

Table 4 *(continued)*

PSR[a]	PSR B	DM	MJD	θ	W_{50}	W_{10}	S/N	S_{350}	α	Refs.
		(pc/cm^3)		(deg)	(ms)	(ms)		(mJy)		
J0828−3417*	B0826−34	51.5(4)	56902	0.362	112	913	138.2(14)	130(20)	···	···
J0835−3707	···	112.4(13)	56968	0.109	6	16	40(20)	3.2(17)	···	···
J0837+0610	B0834+06	12.8(3)	58079	0.191	23	36	400(10)	27.(6)	−2.7(2)	8,10,2,26
J0838−2621	···	116.9[‡]	56747	0.176	7	45	16.(2)	2.4(5)	···	···
J0846−3533*	B0844−35	94.2(2)	56936	0.164	16	95	75.2(8)	9.8(15)	−1.3(6)	38,26,11
J0849+8028	B0841+80	34.9(4)	55152	0.057	26	93	39.6(19)	2.0(4)	−1.12(5)	1,39
J0855−3331*	B0853−33	86.4(3)	56899	0.315	24	40	101.3(8)	12.0(19)	−2.14(9)	10,2,26,11
J0908−1739*	B0906−17	15.79(13)	57148	0.247	9	23	87.(3)	7.2(16)	−1.5(4)	8,2,26
J0912−3851	···	71.5(3)	56972	0.255	36	72	11.2(19)	1.6(4)	···	···
J0921+6254*	B0917+63	13.0(4)	55202	0.163	19	48	61.4(16)	3.4(6)	−1.04(15)	1,2
J0922+0638	B0919+06	27.29(11)	58002	0.220	11	24	248.8(11)	16.(4)	−1.6(6)	10,2,26,11
J0928+06	···	49.7(5)	58057	0.190	23	50	21.(4)	0.9(3)	···	···
J0930−2301*	···	78.4(4)	56663	0.085	12	60	27.9(9)	1.2(2)	···	···
J0931−1902	···	41.5(4)	56993	0.321	0.4	1	4.8(7)	1.6(4)	···	···
J0932−3217	···	102.1(4)	56785	0.197	22	54	31.3(12)	2.1(3)	···	···
J0943+41*	···	21.7(5)	55635	0.067	17	88	30.6(13)	1.2(2)	···	···
J0944−1354	B0942−13	12.43(14)	57095	0.351	7	13	85.1(5)	7.2(16)	−2.(5)	2,11
J0947+2740*	···	28.9(2)	56180	0.295	32	48	46.(2)	3.9(9)	−1.77(14)	1,31,40
J0952−3839*	B0950−38	163.5(3)	56973	0.165	36	85	70.8(13)	5.8(10)	−0.(4)	38,26
J1012−2337*	B1010−23	22.6(6)	56666	0.179	45	79	214.3(14)	10.(2)	−3.(2)	2
J1012+5307	···	9.022(5)	55351	0.242	0.7	1	39.(2)	8.(2)	−0.9(4)	5,1,41,27,34,42
J1018−1523[B]	···	17.17(2)	57098	0.004	2	5	8.(2)	0.49(16)	···	···
J1018−1642	B1016−16	48.8(4)	57127	0.277	28	57	96.0(3)	6.0(12)	−1.61(16)	2,26
J1024−0719	···	6.48(5)	57444	0.236	0.6	1	22.5(19)	5.7(13)	−1.7(2)	5,33,43,29,28,26
J1034−3224*	···	50.6(2)	56785	0.036	17	176	141.2(15)	14.(2)	−1.1(15)	15,26,11
J1038+0032	···	26.34(11)	57754	0.123	2	5	18.(3)	2.4(7)	−1.963(7)	33,36
J1041−1942*	B1039−19	33.9(3)	56998	0.116	41	80	126.7(7)	8.4(17)	−0.(4)	2,26
J1045−0436[B]	···	4.833(9)	57156	0.001	1	4	29.(2)	2.9(6)	···	···
J1046+0304	···	24.98(8)	57997	0.090	3	13	5.5(7)	0.25(6)	···	···
J1047−3032	···	52.28(8)	56777	0.116	13	26	80.5(4)	5.7(11)	−1.(3)	23,24,12
J1101+65*	···	19.2(9)	55227	0.007	37	69	23.3(13)	0.62(13)	···	···
J1110+58*	···	26.2(2)	55285	0.047	17	39	13.3(6)	0.66(13)	−0.(2)	1,17
J1115+5030*	B1112+50	9.1(4)	55367	0.260	22	44	141.5(5)	7.2(16)	−1.37(17)	8,1,2
J1116−2444	···	29.6(2)	56719	0.275	8	29	44.(2)	2.7(6)	···	···
J1120−24[B]	···	9.81(12)	56663	0.094	6	13	13.7(11)	0.45(11)	···	···
J1122−3546[B]	···	39.49(8)	56907	0.006	1.0	1	12.5(3)	1.7(3)	···	···
J1125+7819	···	11.22(4)	55168	0.203	0.4	1.0	52.2(4)	8.1(16)	···	···
J1126−27*	···	27.09(9)	56772	0.008	8	19	5.4(19)	0.29(12)	···	···
J1126−38	···	46.0(2)	56990	0.375	31	57	45.7(4)	10.(2)	···	···
J1134+24[G]	···	24.19(12)	56457	0.462	13	24	7.(3)	1.8(8)	···	···

Table 4 continued

Table 4 *(continued)*

PSR[a]	PSR B	DM (pc/cm^3)	MJD	θ (deg)	W_{50} (ms)	W_{10} (ms)	S/N	S_{350} (mJy)	α	Refs.
J1141−3107*	···	30.82(13)	56780	0.311	18	29	44.9(16)	4.5(9)	−1.(5)	15,12
J1141−3322*	···	46.38(7)	56844	0.086	4	9	60.0(14)	2.6(5)	−1.(6)	23,24,26
J1154−19[B]	···	10.69(4)	56999	0.011	0.5	1	15.3(8)	1.4(3)	···	···
J1221−0633[B]	···	16.43(19)	57379	0.008	0.2	0.3	9.3(4)	0.98(19)	···	···
J1231−1411	···	8.072(3)	57096	0.243	0.4	0.8	9.1(3)	1.7(3)	−2.3(3)	33,44
J1234−3630*	···	59.29(14)	56929	0.219	9	16	45.9(8)	2.9(5)	···	···
J1235−02[L]	···	18.7(9)	57545	0.191	96	135	51.4(10)	3.6(6)	···	···
J1239+2453*	B1237+25	9.4(3)	56458	0.438	36	67	384.9(13)	80(20)	−0.87(4)	8,13,1,2,12
J1239+32[B]	···	16.85(4)	56054	0.021	0.4	1	20(20)	2.(2)	···	···
J1257−1027*	B1254−10	29.7(15)	57062	0.245	6	27	73.5(6)	7.7(14)	−1.6(4)	2
J1300+1240	B1257+12	10.15(6)	58356	0.058	0.8	1	32.3(18)	5.1(10)	−1.8(17)	5,1,45,46
J1308−23[B]	···	22.357(11)	56718	0.006	0.2	0.4	32.6(12)	3.3(6)	···	···
J1311−1228	B1309−12	36.21(11)	57091	0.287	6	13	117.3(7)	10.2(19)	−2.2(13)	2
J1317−0157[B]	···	29.39(3)	57542	0.007	0.3	0.5	14.(2)	1.7(4)	···	···
J1320−3512	···	15.52(11)	56962	0.044	24	60	13.0(4)	1.7(2)	···	···
J1320+67*	···	28.0(2)	55200	0.093	11	58	15.1(7)	0.89(17)	···	···
J1321+8323	B1322+83	13.37(17)	55166	0.252	21	40	86.0(6)	7.6(15)	−1.49(11)	1,2
J1327−0755	···	27.9(2)	57637	0.251	0.1	0.3	19.2(19)	2.3(5)	···	···
J1327+34[B]	···	4.193(16)	56052	0.007	1	2	68.3(9)	3.7(7)	···	···
J1332−3032*	···	14.81(16)	56845	0.146	29	109	69.4(8)	14.(2)	−2.7(9)	23,24
J1335−3642*	···	41.82(13)	56972	0.204	10	38	35.(2)	5.3(8)	···	···
J1336−2522*	···	37.39(12)	56751	0.093	13	26	42.6(12)	2.8(5)	···	···
J1358−2533	···	16.0(2)	56752	0.228	13	51	10.(6)	0.6(4)	···	···
J1400−1431	···	4.932(3)	57855	0.216	0.2	0.5	32.2(8)	5.0(9)	−1.(2)	47
J1411+2551	···	12.34(16)	56459	0.100	2	4	17.3(13)	1.1(2)	···	···
J1418−3921	···	60.2(2)	57063	0.214	22	58	103.0(4)	13.5(18)	−2.(5)	15,12
J1434+7257	···	12.61(16)	55196	0.371	1	3	11.(2)	2.1(6)	−2.5(2)	1,17
J1439+76*	···	22.3(2)	55196	0.024	6	31	9.7(11)	0.41(9)	···	···
J1455−3330	···	13.56(8)	56962	0.058	0.6	2	40.9(6)	8.7(12)	−1.5(6)	29
J1501−0046	···	22.3(11)	57509	0.244	11	16	23.9(15)	2.2(4)	···	···
J1505−25[B]	···	44.6(2)	56754	0.001	11	26	22.3(10)	1.12(18)	···	···
J1509+5531	B1508+55	19.61(19)	55349	0.181	11	27	630(20)	50(10)	−2.0(2)	8,20,2
J1515−32[B]	···	25.3(16)	56936	0.493	2	3	65.(2)	37.(5)	···	···
J1518−0627	···	27.7(2)	57998	0.205	8	41	11.(5)	1.1(6)	···	···
J1518−3950[ML]	···	102.4(12)	57538	0.265	8	42	17.3(9)	4.9(6)	···	···
J1518+4904	···	11.61(16)	55415	0.223	1	3	82.3(15)	7.7(15)	−1.09(13)	5,1,14,27,46,42
J1524−33	···	73.3(3)	56958	0.260	16	97	8.8(18)	2.0(5)	···	···
J1527−3931*	B1524−39	48.7(6)	57384	0.061	39	65	144.1(15)	12.4(15)	−1.8(2)	38,11
J1528−3146	···	18.19(15)	56936	0.125	1	5	17.(2)	2.7(5)	···	···
J1529−26[B]	···	44.5(2)	56755	0.499	20	30	20.4(7)	9.4(14)	···	···

Table 4 continued

Table 4 *(continued)*

PSR[a]	PSR B	DM (pc/cm^3)	MJD	θ (deg)	W_{50} (ms)	W_{10} (ms)	S/N	S_{350} (mJy)	α	Refs.
J1529−3828	···	73.62‡	57129	0.101	0.8	1	6.(4)	1.3(9)	···	···
J1530−21[B]	···	38.05(13)	56588	0.000	12	28	11.8(8)	0.92(15)	···	···
J1532+2745*	B1530+27	14.6(2)	56457	0.208	18	46	108.1(4)	7.5(13)	−1.67(14)	13,1,2
J1536−30[B]	···	63.6(4)	56908	0.005	13	66	16.1(18)	1.7(3)	···	···
J1536−3602*	···	86.8(2)	57095	0.148	51	112	32.1(10)	5.2(6)	···	···
J1543−0620	B1540−06	18.3(18)	58082	0.253	9	20	150.6(14)	10.2(17)	−1.3(12)	8,2
J1544+4937	···	23.22(2)	55413	0.271	0.2	0.4	31.(2)	6.1(13)	−0.7651(12)	33,48
J1547−0944*	···	36.9(4)	58252	0.145	30	42	28.1(15)	1.7(3)	···	···
J1555−0515*	···	23.2(2)	58051	0.051	10	19	37.5(11)	1.4(2)	···	···
J1555−2341	B1552−23	51.95(13)	56718	0.189	13	31	67.8(7)	7.8(11)	−1.6(4)	2
J1555−3134*	B1552−31	73.11(13)	56936	0.379	13	32	53.9(15)	17.(2)	−1.0(3)	2,12
J1600−3053	···	52.312(3)	56933	0.338	0.3	1	7.(2)	6.3(19)	−0.8(3)	28
J1603−2531*	···	53.7(7)	56755	0.266	6	17	20.(3)	3.5(7)	···	···
J1603−2712*	B1600−27	46.2(2)	56779	0.136	20	35	161.8(12)	15.(2)	−1.5(14)	2
J1607−0032*	B1604−00	10.72(18)	57508	0.279	14	20	168.(2)	22.(3)	−2.2(3)	8,1,10,2,12
J1611−29[B]	···	83.033(3)	56907	0.006	0.5	1	22.(4)	3.5(8)	···	···
J1612−2408*	···	49.2(2)	56750	0.180	23	33	95.4(8)	8.8(11)	···	···
J1614−2230	···	34.49(3)	56663	0.215	0.3	0.6	19.5(18)	5.6(8)	···	···
J1614−23	···	52.4(13)	56747	0.148	1	2	13.5(12)	1.9(3)	···	···
J1614−3937	···	151.7(15)	58175	0.216	16	29	41.5(7)	10.9(10)	−2.0(7)	15,12
J1615−2940*	B1612−29	44.6(6)	56907	0.169	23	57	66.9(19)	5.5(7)	−1.(9)	2
J1622−3751	···	155.7(18)	57152	0.022	16	61	7.(2)	1.6(4)	···	···
J1623−0908	B1620−09	68.1(3)	58257	0.203	14	27	84.1(13)	6.5(10)	−1.6(3)	2
J1623−2631	B1620−26	62.85(4)	56776	0.218	1	2	29.(2)	9.3(12)	−2.1(2)	5,2,29,46,42
J1627+86	···	46.55(12)	55149	0.008	6	11	14.5(15)	0.62(13)	···	···
J1629+33[B]	···	35.0(3)	56089	0.002	42	59	17.0(3)	0.85(15)	···	···
J1629−3827[ML]	···	127.9(13)	57384	0.256	9	23	10.7(5)	2.3(2)	···	···
J1629+43	···	7.36(4)	55553	0.058	4	15	25.9(15)	1.9(3)	···	···
J1630+37	···	14.125(3)	56045	0.645	0.3	1	36.(2)	450(100)	···	···
J1632−1013	···	89.97(18)	58349	0.243	14	34	11.2(5)	1.6(2)	···	···
J1636−2614	···	92.72(13)	56776	0.299	6	13	23.5(13)	3.2(4)	···	···
J1638−35[B]	···	115.1(18)	57123	0.005	10	31	15.8(13)	2.6(4)	···	···
J1638−3815	···	240.2(18)	57155	0.113	10	44	6.8(12)	1.3(2)	···	···
J1641−2347*	···	28.1(2)	56752	0.088	46	68	19.8(14)	2.4(3)	···	···
J1643−10[G]	···	75.850(16)	58349	0.186	3	8	9.(2)	2.3(8)	···	···
J1644−33[B]	···	130.3(12)	56989	0.010	20	57	14.0(4)	3.6(3)	···	···
J1645−0317	B1642−03	35.71(11)	58054	0.131	4	8	1000(40)	110(20)	−2.0(11)	8,1,10,2,11,12
J1646−2142	···	29.735(6)	56588	0.231	0.8	1	7.(2)	3.9(11)	···	···
J1647−3607	···	228.5(5)	57123	0.338	2	9	4.(3)	1.6(13)	···	···
J1647+66*	···	22.7(4)	55202	0.006	23	54	55.(2)	2.8(4)	···	···

Table 4 continued

Table 4 *(continued)*

PSR[a]	PSR B	DM	MJD	θ	W_{50}	W_{10}	S/N	S_{350}	α	Refs.
		(pc/cm^3)		(deg)	(ms)	(ms)		(mJy)		
J1648−3256	···	128.5(18)	56989	0.259	11	20	27.8(7)	4.6(5)	−1.(5)	15,12
J1649+2533*	···	34.3(2)	56480	0.038	27	45	43.(2)	2.7(4)	−0.(2)	1,49
J1649+80	···	31.09(2)	55166	0.009	0.2	0.3	15.9(11)	1.6(3)	···	···
J1652−2404*	B1649−23	68.41‡	56754	0.277	39	58	83.1(8)	14.9(16)	−1.5(3)	2,12
J1652+2651*	···	40.8(2)	56459	0.126	27	48	176.(3)	12.(2)	0.5(6)	1,49,14
J1654−2636[ML]	···	103.3(2)	56783	0.233	25	150	14.(2)	4.2(8)	···	···
J1654−2713	···	93.3(2)	56783	0.271	23	46	14.5(17)	3.3(5)	···	···
J1655−3048*	···	154.1(14)	56932	0.212	19	109	22.8(18)	10.6(13)	···	···
J1700−3312*	···	167.2(3)	56989	0.139	49	75	22.(2)	5.3(7)	−1.5(19)	15,26,11,12
J1700−3611*	···	233.9(3)	57129	0.159	34	56	14.(2)	3.2(6)	···	···
J1701−3130	···	131.4(7)	56933	0.142	20	28	10.(2)	3.1(8)	···	···
J1703−3241	B1700−32	110.3(3)	56962	0.258	50	64	169.7(14)	54.(4)	−1.(2)	2,26,11,12
J1705−3423	···	146.4(6)	57123	0.110	25	57	25.(6)	14.(3)	−1.3(2)	15,26,11,12
J1706+59	···	30.7(3)	55284	0.475	20	56	96.(2)	27.(4)	−0.(3)	1,17
J1708−3426*	···	188.7(17)	57127	0.200	88	129	16.(6)	12.(5)	−2.3(3)	15,26,11,12
J1710−2616*	···	110.0(2)	56776	0.126	46	95	20.(3)	5.1(9)	···	···
J1710+49	···	7.083(3)	55416	0.000	0.3	0.7	9.6(16)	1.2(3)	···	···
J1712−2715	···	91.78(6)	56783	0.086	38	63	21.6(4)	9.6(8)	···	···
J1720−0212*	B1718−02	66.92(12)	57655	0.216	66	84	93.4(16)	27.(3)	−1.3(6)	1,2
J1720−2446*	···	104.3(2)	56755	0.221	31	55	13.(3)	3.7(10)	···	···
J1720−2933	B1717−29	42.77(16)	56908	0.322	31	42	73.(2)	47.(4)	−2.24(3)	2,11,12
J1721−2457	···	48.23(3)	56755	0.190	0.6	0.9	8.(5)	4.(3)	···	···
J1722+35	···	22.1(2)	56072	0.133	20	51	8.1(16)	0.9(2)	···	···
J1722−3207	B1718−32	126.0(12)	56958	0.208	19	39	80.0(9)	49.(3)	−1.7(2)	2,26,11,12
J1722−3712	B1719−37	99.56(6)	57170	0.156	6	15	51.(5)	40.(4)	−1.66(17)	38,11,26
J1725−0732*	···	58.72(6)	58255	0.183	10	21	14.(4)	2.8(8)	···	···
J1727−2739*	···	146.0(3)	56783	0.376	35	49	8.7(10)	5.7(8)	−0.9(5)	26,12
J1728−0007	B1726−00	41.09‡	57999	0.416	11	28	21.(6)	9.(3)	−1.64(17)	1,2
J1729−2117	···	34.22(17)	56588	0.214	1	2	11.(2)	2.2(6)	···	···
J1730−2304	···	9.624(8)	56750	0.176	0.6	1	49.2(13)	23.(2)	−1.72(7)	5,33,50,29,26
J1733−01[B]	···	61.98(7)	57535	0.004	9	16	8.(3)	0.9(3)	···	···
J1733−2228*	B1730−22	41.1(2)	56750	0.124	14	79	77.1(6)	25.(2)	−1.31(12)	2,12
J1734−0212	B1732−02	64.8(2)	57542	0.134	27	40	21.(2)	2.6(4)	···	···
J1734−2415	···	117.1(11)	56755	0.157	16	48	4.8(12)	1.4(3)	···	···
J1735−0243*	···	54.8(2)	57656	0.193	12	106	12.4(18)	3.3(6)	···	···
J1735−0724*	B1732−07	73.42(18)	58255	0.244	5	15	100.4(14)	18.(2)	−1.1(16)	2,12
J1736−2457*	···	169.4(6)	56755	0.217	109	170	12.(2)	4.7(12)	···	···
J1738−2330	···	96.6(13)	56750	0.401	39	61	4.(4)	6.(5)	···	···
J1738−3211*	B1735−32	50.09(19)	56962	0.106	26	44	11.(8)	20(10)	−0.7(3)	2,26,12
J1739−2903	B1736−29	138.4(8)	56902	0.130	17	40	7.(5)	12.(8)	−0.8(16)	2,11,26

Table 4 continued

Table 4 *(continued)*

PSR[a]	PSR B	DM	MJD	θ	W_{50}	W_{10}	S/N	S_{350}	α	Refs.
		(pc/cm^3)		(deg)	(ms)	(ms)		(mJy)		
J1740+27[L]	···	35.6(2)	56297	0.115	18	36	29.(6)	1.7(4)	···	···
J1740−3015	B1737−30	152.1(15)	56909	0.291	20	74	7.5(6)	30.(3)	−1.00(3)	2,26
J1741−0840	B1738−08	74.7(5)	58348	0.299	78	116	70(20)	24.(6)	−2.(2)	2
J1741−21[B]	···	150.7(6)	56591	0.010	81	181	9.(4)	2.1(10)	···	···
J1741−2733*	···	147.4(2)	56783	0.084	60	90	27.(2)	16.6(18)	−1.595(14)	26,12
J1741+2758*	···	28.9(3)	56297	0.180	30	48	41.(3)	2.7(5)	−1.77(14)	13,1,49
J1741−3927	B1737−39	158.2(13)	57538	0.265	18	47	59.1(11)	27.(2)	−1.3(4)	38,51,26,11,12
J1742−0203[B]	···	81.89(3)	57542	0.003	4	10	9.(3)	1.7(6)	···	···
J1742−3957	···	220.(7)	57538	0.301	60	125	7.8(7)	4.8(6)	···	···
J1743−0339*	B1740−03	30.11(11)	58054	0.357	11	20	18.(3)	5.8(13)	−1.53(16)	2
J1743−3150	B1740−31	192.2(6)	56962	0.310	113	303	14.(2)	45.(8)	−1.(2)	2,26,11,12
J1744−2335*	···	96.4(4)	56746	0.258	25	51	30(20)	11.(8)	−3.5(2)	23,24
J1745−0129*	···	89.3(2)	57535	0.124	15	50	10.(5)	1.8(9)	···	···
J1745−3040*	B1742−30	88.01(9)	56930	0.299	7	25	61.4(15)	150(10)	−1.2(2)	2,11,26
J1745−3812	···	163.6(18)	57213	0.146	21	62	0(20)	1.(5)	···	···
J1746+2245*	···	49.2(8)	56481	0.321	28	129	11.7(18)	1.5(3)	−1.304(3)	20,52
J1746+2540*	···	51.3(2)	56459	0.196	27	47	15.(2)	1.2(2)	−2.06(11)	1,49
J1750−3503	···	190.5(17)	57151	0.167	87	159	25.2(9)	17.0(15)	−2.(3)	15,35
J1752+2359*	···	36.01(15)	56480	0.404	6	15	13.(2)	2.6(7)	−0.81(19)	1,49
J1752−2806	B1749−28	50.37(14)	56900	0.245	7	13	1050(50)	930(80)	−1.85(5)	8,9,10,2,26,11,12
J1753−38*	···	167.6(17)	57384	0.093	8	21	50(30)	7.(4)	···	···
J1754−3443	···	188.7(9)	57151	0.276	28	52	16.1(17)	10.1(13)	···	···
J1754−3510	···	81.23(11)	57151	0.239	9	26	10.(2)	3.8(10)	···	···
J1754+5201	B1753+52	35.5(6)	55384	0.259	19	149	22.(2)	2.4(4)	−0.0(4)	1,2
J1755−0903	···	63.67(4)	58349	0.165	6	20	17.7(15)	6.4(7)	···	···
J1755−2725	···	115.1(6)	56810	0.205	9	27	6.0(16)	6.8(19)	···	···
J1758+3030*	···	35.0(2)	56178	0.164	22	41	107.(4)	7.4(13)	−1.5(4)	13,1,14
J1759−1029	···	115.4(6)	58355	0.347	185	329	11.7(17)	11.1(19)	···	···
J1759−2205	B1756−22	177.0(11)	56663	0.249	9	28	25.(6)	27.(7)	−2.01(18)	2,11,35,26
J1759−2922	···	79.42(14)	56902	0.286	9	17	32.(6)	14.(2)	−2.4(7)	23,24,35
J1759−3107*	···	128.3(2)	56932	0.177	25	61	17.(4)	5.7(15)	−1.4(6)	26,35
J1800−0125	···	51.0(2)	57535	0.301	25	41	10.(2)	3.3(9)	···	···
J1800+5034	···	22.64(14)	55384	0.004	13	20	43.(2)	2.0(3)	···	···
J1801−0357*	B1758−03	120.2(2)	58087	0.234	10	25	63.5(5)	11.7(11)	−2.3(14)	2
J1801−2920*	B1758−29	125.4(2)	56903	0.084	37	71	71.(2)	28.(2)	−1.90(16)	53,26,11,12
J1802+0128	···	101.4(14)	57854	0.205	29	54	5.(3)	2.0(13)	···	···
J1803−3329	···	170.9[‡]	56989	0.234	15	57	6.1(16)	2.8(8)	···	···
J1804−2717	···	24.66(9)	56783	0.102	0.8	2	14.(2)	11.(2)	−1.(4)	29,46
J1804−28	···	213.0(3)	56810	0.270	17	67	7.(2)	4.5(14)	···	···
J1805+0306	B1802+03	80.95(5)	57692	0.493	3	14	8.(5)	8.(4)	−1.33(3)	1,54

Table 4 continued

Table 4 *(continued)*

PSR[a]	PSR B	DM	MJD	θ	W_{50}	W_{10}	S/N	S_{350}	α	Refs.
		(pc/cm^3)		(deg)	(ms)	(ms)		(mJy)		
J1805−0619	···	147.1(11)	58254	0.146	15	32	7.(5)	2.1(15)	···	···
J1806+2819	···	18.69(6)	56254	0.180	2	2	21.8(17)	3.9(7)	···	···
J1807−0847	B1804−08	112.3(4)	58349	0.225	5	17	68.5(9)	32.(2)	−0.6(12)	2,26,11,12
J1807−2715	B1804−27	313.2(2)	56782	0.274	29	74	24.(3)	19.(3)	−2.5(3)	55,2,11,35
J1808+00	···	149.2(19)	57877	0.358	19	34	8.(4)	5.(2)	···	···
J1808−0813*	···	151.6(2)	58258	0.215	28	67	30.(3)	14.(2)	−2.2(3)	15,26,11,12
J1808−3249*	···	147.3(9)	56966	0.209	6	25	12.(3)	4.7(13)	···	···
J1809−0119	···	138.3(19)	57511	0.203	34	49	9.(2)	2.5(6)	···	···
J1809−3547	···	192.2(2)	57151	0.305	108	191	18.8(19)	14.(2)	···	···
J1811−0154*	···	148.1(2)	57535	0.248	26	54	10.(3)	3.4(11)	···	···
J1811−2439	···	167.2(17)	56773	0.251	19	41	19.(2)	13.(2)	···	···
J1812+0226	B1810+02	104.1(2)	57692	0.232	15	25	25.(3)	5.1(10)	−2.0(3)	2
J1812−3039	···	141.4(15)	56931	0.206	12	38	6.(2)	2.0(6)	···	···
J1813+4013	B1811+40	41.4(2)	55845	0.311	22	36	121.8(19)	12.(2)	−1.64(14)	1,2,56
J1814−0521	···	130.6(2)	58233	0.415	23	66	7.(2)	8.(3)	···	···
J1815+55	···	58.86(11)	55346	0.006	10	18	11.(7)	0.6(4)	···	···
J1816−0755	···	117.9(5)	58258	0.037	7	12	18.4(4)	5.0(5)	···	···
J1816−2650*	B1813−26	128.3(15)	56782	0.317	34	73	31.1(16)	24.(2)	−1.50(7)	2,11,12
J1816+4510	···	38.88(3)	55526	0.274	0.3	1.0	34.(4)	10.(2)	−3.5(3)	33,17
J1817−3618*	B1813−36	94.1(9)	57152	0.125	6	15	96.(2)	14.4(15)	−1.2(4)	38,57,26,11,12
J1817−3837	···	102.7(9)	57383	0.062	9	17	45.(2)	5.6(6)	−1.1(8)	23,26,12
J1819−37[B]	···	68.2(16)	57170	0.003	8	38	24.1(12)	4.2(5)	···	···
J1820−0427	B1818−04	84.37(15)	58082	0.155	10	29	118.9(11)	29.(2)	−1.(2)	1,10,2,11,12
J1820−0509*	···	102.4(8)	58233	0.212	10	22	18.(3)	7.5(16)	···	···
J1821+0155	···	51.75[‡]	57695	0.123	0.5	1	9.(2)	1.8(4)	···	···
J1821+41*	···	40.6(3)	55689	0.000	9	43	18.4(11)	0.89(19)	···	···
J1822+02[B]	···	103.8(3)	57665	0.000	62	93	14.9(5)	3.5(5)	···	···
J1822−2256*	B1819−22	121.4(4)	56750	0.278	87	128	51.8(18)	28.(2)	−1.44(5)	2,26,11,12
J1823−0154*	···	135.8(19)	57535	0.311	11	25	17.(5)	6.(2)	−2.2(7)	15,11,35
J1823−3021A	B1820−30A	86.88(5)	56908	0.234	0.9	1	27.(3)	18.(3)	−2.5(6)	29,58
J1823−3021B*	B1820−30B	86.88(9)	56908	0.232	5	13	16.(2)	3.3(6)	−2.4(3)	2,58
J1823−3106	B1820−31	50.24(7)	56931	0.092	5	12	136.3(16)	19.4(19)	−1.3(3)	10,2,26,11,12
J1824−0127*	···	63.00(2)	57535	0.125	16	59	38.(2)	7.6(9)	···	···
J1824−2328*	···	195.3(2)	56752	0.184	39	96	18.(2)	6.0(11)	···	···
J1825+0004	B1822+00	56.7(2)	57997	0.270	10	26	30.(3)	7.7(10)	−1.4(2)	1,2
J1825−0935	B1822−09	19.29(19)	58347	0.123	15	32	82.(2)	48.(3)	−2.2(9)	8,10,2,11,12
J1825−31	···	93.3(10)	56933	0.214	47	163	4.(5)	1.5(16)	···	···
J1829+0000	···	116.8(5)	57507	0.184	8	20	13.(2)	5.0(11)	···	···
J1829+25[B]	···	74.0(7)	56458	0.003	33	57	17.7(17)	0.82(15)	···	···
J1831−0823	···	246.4(15)	58347	0.119	13	54	5.7(8)	3.7(6)	−1.2(8)	26,12

Table 4 continued

Table 4 *(continued)*

PSR[a]	PSR B	DM (pc/cm^3)	MJD	θ (deg)	W_{50} (ms)	W_{10} (ms)	S/N	S_{350} (mJy)	α	Refs.
J1832−0827	B1829−08	303.7(16)	58347	0.185	49	113	12.(3)	16.(5)	−0.92(13)	2,11,26
J1833−0338	B1831−03	234.8(17)	57999	0.236	46	115	71.(5)	62.(6)	−2.7(7)	2,26,11,35
J1834−0010	B1831−00	88.36(13)	57506	0.212	29	46	17.(5)	7.(2)	−2.58(16)	1,2,35
J1834−0426*	B1831−04	79.4(7)	58055	0.178	18	83	111.(2)	150(10)	−2.0(3)	1,2,11,35
J1835−1020	···	115.9(7)	58355	0.040	10	37	10(10)	7.(9)	−0.86(3)	56,12,26
J1836−1008	B1834−10	315.8(14)	58355	0.236	49	192	16.(3)	36.(7)	−2.1(2)	2,11,12,26
J1836+51[B]	···	44.4(2)	55385	0.000	18	35	5.(6)	0.4(4)	···	···
J1837−0045	···	87.11(15)	57506	0.202	16	35	17.5(6)	5.5(4)	−1.(6)	15,12
J1838−1046	···	209.3(3)	58355	0.272	17	54	10.(2)	6.1(14)	···	···
J1839−0627	···	92.49(12)	58255	0.131	18	28	13.(5)	10.(4)	···	···
J1840−0840	···	285.2(13)	58347	0.386	243	608	9.(4)	17.(8)	···	···
J1840+5640*	B1839+56	26.7(4)	55330	0.158	25	56	310(20)	23.(3)	−1.23(8)	8,1,2
J1842+0257*	···	146.0(7)	57665	0.335	63	120	17.(4)	10.(3)	···	···
J1842−39[B]	···	47.6(9)	57384	0.013	17	56	23.(8)	3.9(14)	···	···
J1843−0000	···	101.8(2)	57507	0.152	58	179	13.2(8)	10.1(9)	−0.5(7)	26,11,12
J1844+00	···	346.6(11)	57877	0.002	43	139	21.(3)	18.(3)	···	···
J1844−0433*	B1841−04	123.0(2)	58107	0.120	42	92	23.(2)	14.(2)	−1.7(2)	2,26,35
J1846−07492	···	190.8(2)	58204	0.415	18	42	8.(3)	14.(6)	···	···
J1847−0402	B1844−04	142.0(15)	58055	0.088	33	84	80(10)	55.(8)	−2.11(15)	2,11,26
J1848−0023	···	34.9(2)	57507	0.165	8	31	7.(4)	4.(2)	···	···
J1848−0123	B1845−01	159.1(17)	57511	0.140	83	0.0	34.(3)	50.(6)	−1.2(3)	2,26,11,12
J1849−0317	···	40.0(17)	57452	0.256	15	40	15.(5)	14.(5)	···	···
J1849−0614	···	118.2(2)	58087	0.169	17	35	14.(5)	8.(3)	···	···
J1849−0636	B1846−06	148.3(3)	58204	0.225	29	77	46.(4)	31.(5)	−2.319(12)	2,26,11,35
J1849+2423	···	62.53(7)	56276	0.152	16	26	11.(6)	1.7(10)	−1.54(19)	1,52
J1850+0026	···	201.2(2)	57997	0.182	68	182	8.6(8)	9.5(11)	···	···
J1851−0053	···	23.9(3)	57510	0.274	23	42	19.(4)	11.(2)	−1.56(17)	1,12
J1852−2610	···	56.81(8)	56777	0.200	6	25	94.(7)	19.(2)	−1.8(7)	15,26,12
J1854+36[A]	···	59.8[‡]	56046	0.146	48	140	11.(4)	1.6(7)	···	···
J1855−0941	···	153.6(8)	58252	0.124	32	51	14.(2)	8.0(18)	···	···
J1856+0113	B1853+01	96.47(6)	57818	0.170	4	10	8.(2)	3.6(9)	−2.(5)	2,35
J1856−0526	···	131.8(9)	58087	0.245	16	41	13.(3)	9.(2)	···	···
J1857+0057	B1854+00	82.54(9)	57877	0.154	33	42	15.(2)	11.(2)	−1.4(7)	59,35
J1857−1027	···	107.3(9)	58355	0.140	116	257	48.(3)	11.6(14)	···	···
J1859+00	···	423.0(14)	57877	0.210	69	109	23.(3)	19.(3)	···	···
J1859+76	···	47.0(3)	55177	0.003	32	50	15.(3)	0.7(2)	···	···
J1900−2600*	B1857−26	37.92(15)	56777	0.118	13	69	521.2(5)	100(10)	†	···
J1900−0933	···	162.6(3)	58252	0.049	104	36	10(10)	2.(3)	···	···
J1900+30*	···	71.91(15)	56085	0.088	12	19	31.9(17)	2.0(3)	···	···
J1901+0156	B1859+01	105.3(7)	57692	0.276	3	8	42.5(8)	21.(2)	−2.976(19)	1,2,35

Table 4 continued

Table 4 *(continued)*

PSR[a]	PSR B	DM	MJD	θ	W_{50}	W_{10}	S/N	S_{350}	α	Refs.
		(pc/cm^3)		(deg)	(ms)	(ms)		(mJy)		
J1901−04[B]	···	106.5(7)	57544	0.016	72	352	13.(4)	6.(2)	···	···
J1901−0906	···	72.4(4)	58252	0.121	14	73	36.(2)	8.2(12)	−1.1(8)	23,24,26,11,12
J1902−1036	···	96.2(2)	58355	0.215	11	44	10.(2)	2.5(6)	···	···
J1903+0135*	B1900+01	245.0(18)	57695	0.254	23	70	73.5(15)	45.(4)	−1.6(3)	2,26,11,35
J1903−0258	···	114.1(7)	57452	0.225	11	33	7.(5)	4.(3)	···	···
J1903−0632*	B1900−06	195.7(11)	58204	0.433	18	48	25.(2)	29.(4)	−2.3(2)	2,26,11
J1903−0848	···	66.6(2)	58227	0.380	16	35	8.(6)	4.(3)	···	···
J1903+2225	···	110.8(16)	56457	0.177	7	52	5.(4)	0.9(8)	···	···
J1904+0004	···	233.2(3)	57877	0.028	11	19	20.8(10)	8.1(9)	−1.3(6)	15,26,12
J1904+33[B]	···	81.04(17)	56053	0.001	15	33	12.8(16)	1.1(2)	···	···
J1905−0056*	B1902−01	228.9(16)	57510	0.240	12	27	42.5(4)	12.7(12)	−2.0(3)	2,26,12
J1907+4002*	B1905+39	30.9(3)	55846	0.081	62	77	222.(2)	15.(2)	−0.7(6)	13,1,2
J1907+57[B]	···	54.63(19)	55330	0.002	8	25	20.(3)	1.6(3)	···	···
J1908+2351*	···	102.2(9)	56278	0.193	7	16	7.4(5)	0.81(11)	−0.(2)	20,49
J1909−3744	···	10.392(3)	57170	0.185	0.1	0.2	32.(4)	6.5(13)	−1.0(5)	26,11
J1909+0007*	B1907+00	112.7(2)	57877	0.405	8	18	39.8(9)	14.7(19)	−1.5(4)	1,2,11,35
J1909+0254	B1907+02	171.7(2)	57666	0.026	12	31	116.(6)	24.(2)	−2.1(6)	1,2,11,35
J1910+0225	···	209.0[‡]	57692	0.111	12	50	7.(4)	4.(2)	···	···
J1910−0309	B1907−03	205.4(13)	57452	0.272	7	20	81.(2)	24.(2)	−1.7(9)	1,2,11,35
J1911−1114	···	30.97(3)	58355	0.217	0.3	0.6	45.(3)	16.(2)	−2.0(2)	5,33,27,29,46
J1912+2104*	B1910+20	88.5(5)	56460	0.217	15	93	28.(2)	4.6(7)	−1.2(6)	20,2
J1912+2525	···	37.91(16)	56223	0.321	8	17	14.5(19)	2.0(3)	−2.79(4)	1,61
J1913−0440	B1911−04	89.3(2)	57544	0.244	7	15	146.0(16)	21.(2)	−1.4(6)	1,10,2,26,11,12
J1913+3732	···	72.1(2)	56017	0.191	12	30	64.(5)	4.4(8)	−1.6(5)	20,18
J1914+0219	···	236.0(11)	57666	0.275	13	37	13.8(12)	7.5(10)	···	···
J1915+0227	···	191.9(8)	57666	0.083	8	28	33.(3)	13.5(18)	···	···
J1916+32[L]	···	83.3(2)	56075	0.223	19	34	10.(9)	1.1(11)	···	···
J1917+2224*	B1915+22	134.5(11)	56297	0.230	21	38	25.(2)	5.0(7)	−1.85(4)	1,54,62
J1917−30[B]	···	38.1(3)	56902	0.181	35	60	32.7(13)	3.9(5)	···	···
J1918−0642	···	26.58(7)	57997	0.321	0.7	2	13.2(11)	10.2(14)	−1.88(2)	33,63
J1918−1052	···	62.7(2)	58255	0.211	12	20	21.(2)	2.9(5)	···	···
J1919+0021*	B1917+00	90.3(3)	57877	0.174	24	47	75.1(17)	14.2(15)	−1.89(19)	1,2,11
J1920+2650*	B1918+26	27.7(2)	56159	0.148	13	23	113.(2)	10.9(14)	−1.6(10)	1,2
J1921−05B[B]	···	80.7(5)	58087	0.000	27	96	20(10)	2.3(15)	···	···
J1921−05A	···	97.5(2)	58087	0.216	20	32	9.6(19)	1.8(4)	···	···
J1921+1948	B1918+19	154.1(2)	56480	0.561	29	80	10.(4)	17.(8)	−2.3(3)	2
J1921+2153	B1919+21	12.4(3)	56457	0.088	30	46	249.2(13)	25.(3)	−2.(4)	8,13,20,10,2,12
J1921+42	···	53.18(15)	55633	0.492	7	26	85.4(10)	32.(5)	···	···
J1922+2018	B1920+20	201.6(3)	56480	0.338	56	79	8.(4)	2.8(14)	−2.(3)	2
J1922+2110*	B1920+21	216.9(2)	56459	0.267	13	41	89.(2)	15.1(17)	−1.5(15)	1,2

Table 4 continued

Table 4 *(continued)*

PSR[a]	PSR B	DM	MJD	θ	W_{50}	W_{10}	S/N	S_{350}	α	Refs.
		(pc/cm^3)		(deg)	(ms)	(ms)		(mJy)		
J1922+58	···	53.74(13)	55330	0.017	13	20	16.(2)	0.9(2)	−1.(3)	1,17
J1923+2515	···	18.85(3)	56180	0.170	0.4	0.7	19.7(6)	4.5(6)	−1.96(4)	33,21,34
J1927+2234	B1925+22	186.5(3)	56296	0.296	28	86	13.(6)	3.0(15)	···	···
J1928+28[B]	···	79.2(2)	56107	0.005	43	55	13.(2)	1.2(2)	···	···
J1929+00	···	42.95(7)	57877	0.049	18	53	24.1(7)	3.3(3)	···	···
J1929+3817	···	93.2(2)	55851	0.122	26	84	34.0(14)	4.0(6)	···	···
J1929+62*	···	67.7(3)	56657	0.071	24	47	13.6(10)	0.66(12)	−0.7(18)	1,17
J1929+66[B]	···	59.5(2)	55178	0.010	13	38	8.2(7)	0.50(9)	···	···
J1930−01[G]	···	36.45(15)	57535	0.492	19	40	48.1(4)	48.(5)	···	···
J1931+30*	···	53.03(15)	56082	0.317	8	21	9.(7)	2.0(17)	···	···
J1932+2020	B1929+20	211.3(6)	56477	0.081	16	43	63.5(18)	19.4(18)	−1.(3)	2
J1932+2220	B1930+22	218.9(3)	56297	0.137	2	6	38.(2)	5.2(6)	−1.2(3)	2
J1932−3655*	···	60.12(14)	57155	0.319	8	31	9.2(11)	1.7(3)	−1.(2)	23,26,12
J1935+52*	···	71.26(14)	55363	0.006	21	44	18.9(15)	1.7(2)	···	···
J1937+2544*	B1935+25	53.26(5)	56180	0.227	6	14	55.5(5)	15.6(16)	−0.9(8)	1,2,12
J1937+2950	···	113.6(4)	56082	0.101	35	119	28.(2)	4.5(7)	−2.9(10)	20,64
J1939+66	···	41.24(8)	55179	0.010	0.5	1	18.9(16)	1.3(2)	···	···
J1939+2134	B1937+21	71.02(2)	56459	0.234	0.3	0.8	34.3(4)	36.(3)	−1.1(5)	33,65,27,28
J1939+2449*	B1937+24	143.2(16)	56224	0.334	23	33	22.(4)	7.4(17)	···	···
J1940−2403*	···	65.4(4)	56752	0.324	40	70	60.(2)	8.6(13)	···	···
J1940−24[B]	···	53.4(3)	56773	0.019	2	3	60.(2)	4.9(7)	···	···
J1941+0121	···	51.87(5)	57755	0.151	21	29	19.9(11)	5.6(7)	−1.68(5)	1,60
J1941+0237[HL]	···	87.2(3)	57693	0.311	47	59	23.9(13)	7.0(11)	···	···
J1941−2602*	B1937−26	50.03(14)	56777	0.198	4	13	67.(2)	5.6(8)	−1.1(9)	2,26,11,12
J1941+43*	···	79.4(2)	55633	0.002	15	29	20.4(13)	1.4(2)	···	···
J1942+81*	···	40.19(5)	55128	0.005	2	5	12.8(6)	0.52(15)	···	···
J1943−1237	B1940−12	29.0(2)	58349	0.346	12	23	89.2(3)	14.(2)	−2.16(11)	10,2,11,12
J1945−0040*	B1942−00	59.7(2)	57507	0.138	28	69	98.(3)	17.(2)	−1.7(2)	1,2
J1946−09[B]	···	50.63(2)	58055	0.006	4	8	6.(2)	0.9(4)	···	···
J1946−1312*	···	63.04(12)	58348	0.155	9	23	17.0(5)	1.8(3)	···	···
J1946+2244	B1944+22	141.5(3)	56296	0.228	17	50	10.1(9)	1.8(2)	−2.0(14)	66,67
J1946−2913*	B1943−29	44.3(2)	56901	0.254	8	25	88.(2)	7.7(11)	−1.8(7)	2,26,11,12
J1948−27[B]	···	57.85(8)	56783	0.007	6	10	14.(2)	0.75(16)	···	···
J1948+3540*	B1946+35	129.1(18)	56044	0.092	29	89	98.5(4)	17.(2)	−1.(3)	20,2
J1949−2524*	B1946−25	23.0(2)	56777	0.225	12	24	75.(2)	5.4(8)	−1.7(4)	2,11
J1949+34[B]	···	228.2(14)	56052	0.006	17	53	15.5(16)	3.3(4)	···	···
J1952+3252	B1951+32	45.17(15)	56073	0.085	3	7	32.8(8)	10.7(10)	−1.83(13)	1,2
J1953+2732*	···	194.2(3)	56157	0.218	33	43	9.4(14)	1.3(2)	···	···
J1953+67	···	57.14(8)	55178	0.007	0.5	0.8	16.(4)	1.3(4)	···	···
J1954+2923*	B1952+29	7.95(11)	56089	0.245	7	30	46.9(18)	14.1(14)	−1.5(11)	1,2

Table 4 continued

Table 4 *(continued)*

PSR[a]	PSR B	DM (pc/cm^3)	MJD	θ (deg)	W_{50} (ms)	W_{10} (ms)	S/N	S_{350} (mJy)	α	Refs.
J1954+3852	···	65.36(9)	55852	0.234	4	9	11.(2)	11.(2)	···	···
J1954+43*	···	129.6(3)	55633	0.002	100	135	19.(8)	3.0(13)	···	···
J1955+2908	B1953+29	104.5(6)	56107	0.191	0.6	1	39.6(10)	20.(2)	−1.2(3)	33,68,46
J1955+5059*	B1953+50	31.98‡	55420	0.314	7	15	164.(2)	20.(2)	−1.22(7)	1,2
J1957+2831*	···	138.8(7)	56107	0.013	8	18	14.0(4)	2.0(2)	−0.4(2)	19
J1959+2048	B1957+20	29.11(2)	56477	0.230	0.4	0.8	32.0(9)	16.(2)	−2.29(18)	33,69,46
J2000+29[B]	···	132.3(7)	56089	0.005	23	87	15.(2)	1.4(3)	···	···
J2001+42	···	54.92(18)	55633	0.005	10	19	18.5(15)	1.6(2)	···	···
J2002+30	···	187.8(18)	56081	0.228	25	79	8.3(10)	3.5(5)	···	···
J2002+3217*	B2000+32	142.0(18)	56073	0.103	17	44	20.8(17)	3.9(4)	−1.1(2)	2
J2002+4050*	B2000+40	130.9(2)	55691	0.371	30	71	60.7(14)	36.(3)	†	···
J2004+3137	B2002+31	234.8(5)	56075	0.131	22	51	107.(5)	13.6(17)	−1.5(10)	2
J2005−0020*	···	36.0(5)	57507	0.203	56	78	37.(3)	4.2(8)	−1.4(4)	1,15,12
J2006−0807*	B2003−08	32.45(15)	57877	0.182	30	113	138.7(18)	31.(5)	−1.3(2)	2,26,11,12
J2006+22[L]	···	127.3(4)	56459	0.363	53	71	6.(5)	1.5(13)	···	···
J2008+2513	···	60.29(15)	56224	0.224	12	31	13.(2)	2.0(4)	−1.6(5)	1,61
J2010−1323	···	22.16(5)	58347	0.262	0.3	0.6	16.0(12)	2.9(5)	−0.4(2)	26,70
J2010+2845	···	112.3(14)	56089	0.188	7	23	31.6(10)	4.5(5)	···	···
J2012−2029	···	37.67(14)	58386	0.397	18	33	17.(5)	4.9(19)	···	···
J2013−0649	···	63.29(14)	57661	0.220	9	21	31.0(14)	2.7(4)	···	···
J2013+3058*	···	148.7(7)	56080	0.050	3	7	18.5(6)	1.7(2)	···	···
J2013+3845	B2011+38	238.2(5)	55852	0.148	27	50	44.1(9)	20.2(18)	−1.00(7)	2
J2015+2524*	···	10.9(5)	56180	0.066	51	97	10.(2)	0.9(2)	···	···
J2016+1948	···	33.76(16)	56480	0.445	1	2	13.3(12)	4.0(7)	−1.947(5)	1,71
J2017−0414[B]	···	30.85(16)	57384	0.008	1	2	10.(2)	0.9(2)	···	···
J2017+2043	···	60.43(13)	56460	0.313	5	24	20.5(3)	3.2(4)	−1.8(10)	1,71
J2017−2737[B]	···	25.38(5)	56783	0.017	12	62	15.9(15)	3.0(5)	···	···
J2017+59	···	60.1(14)	55263	0.003	19	69	12.5(7)	1.7(2)	···	···
J2018+2839	B2016+28	14.19(14)	56089	0.154	16	24	590(20)	100(10)	−0.7(7)	8,13,1,10,2
J2019+2425	···	17.2‡	56254	0.216	0.4	0.9	14.(4)	4.1(14)	···	···
J2019+72[B]	···	34.88(8)	55178	0.006	20	55	10.4(11)	1.7(3)	···	···
J2022+2534[B]	···	53.66(2)	56180	0.009	0.5	1	16.4(6)	6.8(9)	···	···
J2022+2854*	B2020+28	24.66(8)	56089	0.059	7	19	550.3(12)	84.(9)	−0.78(19)	8,1,10,2,72
J2022+5154*	B2021+51	22.54(13)	55383	0.198	9	31	120(10)	17.(2)	−0.0(16)	1,2
J2023+5037	B2022+50	32.98(9)	55440	0.245	6	22	38.(2)	6.3(8)	−1.2(2)	1,2
J2027+4557	···	229.7(2)	55508	0.064	41	120	32.1(14)	7.8(8)	−1.3(10)	64,17
J2027+74	···	11.42(13)	55149	0.008	29	87	25.3(17)	3.0(5)	···	···
J2029+3744*	B2027+37	190.9(3)	55982	0.158	25	50	69.7(6)	17.0(14)	−2.25(17)	1,2
J2030+2228	B2028+22	71.93(16)	56297	0.214	13	29	44.(3)	4.3(7)	−0.72(18)	1,55
J2030+55*	···	59.43(14)	55362	0.149	19	35	13.0(12)	1.3(2)	···	···

Table 4 continued

Table 4 *(continued)*

PSR[a]	PSR B	DM	MJD	θ	W_{50}	W_{10}	S/N	S_{350}	α	Refs.
		(pc/cm^3)		(deg)	(ms)	(ms)		(mJy)		
J2033+0042*	···	37.5(12)	57753	0.307	113	192	51.7(8)	9.1(17)	−0.6(8)	1,11
J2033−1938*	···	23.3(3)	58232	0.099	10	48	26.(3)	1.9(5)	···	···
J2036+2835	···	84.3(3)	56089	0.202	25	35	37.5(10)	2.9(4)	−1.5(6)	1,18
J2037+1942*	B2034+19	36.6(5)	56480	0.453	20	46	30.9(13)	5.6(10)	−1.(2)	1,54
J2037+3621*	B2035+36	93.56(15)	56025	0.200	26	48	43.(4)	10.0(14)	−1.8(5)	2
J2038+35	···	57.91(4)	56046	0.298	5	11	6.0(18)	1.7(6)	···	···
J2038−3816	···	34.0(4)	57170	0.210	29	51	39.7(15)	2.9(5)	−2.(7)	23,26,12
J2038+5319	B2036+53	160.6(3)	55362	0.222	27	54	16.8(13)	1.9(2)	−1.5(3)	20,2
J2039−3616[B]	···	23.96(3)	57151	0.006	0.3	0.5	10.0(15)	1.3(3)	···	···
J2040−21[B]	···	23.87(14)	56655	0.009	22	29	52.6(4)	3.0(5)	···	···
J2043+2740	···	21.02(2)	56110	0.193	2	5	82.5(7)	10.2(13)	−2.(2)	1,40
J2043+7045	···	57.64(15)	55160	0.346	37	23	21.4(17)	3.6(6)	···	···
J2044+28[B]	···	90.3(4)	56089	0.005	31	58	15.1(12)	1.07(16)	···	···
J2044+4614	···	311.3(3)	55508	0.336	104	211	11.2(8)	6.9(8)	···	···
J2046−0421	B2043−04	35.9(3)	57384	0.369	22	39	93.(3)	13.(2)	−1.3(3)	1,10,2,11,26
J2046+5708	B2045+56	101.6(12)	55325	0.165	12	29	22.(4)	2.5(5)	−1.7(3)	1,2
J2048−1616*	B2045−16	11.4(5)	58118	0.260	57	105	377.8(9)	52.(9)	−1.8(10)	9,10,2,26,11,12
J2048+2255	···	70.46(7)	56297	0.248	6	18	11.(9)	1.4(13)	−0.6(2)	20,71
J2051−0827	···	20.72(4)	57656	0.314	0.3	0.7	28.1(9)	7.6(15)	−1.60(14)	5,33,27,29,26,46,42
J2054−39[B]	···	24.8(2)	57214	0.000	8	36	30.9(19)	1.5(3)	···	···
J2055+2209	B2053+21	36.1(2)	56459	0.182	9	24	107.8(5)	9.3(14)	−1.10(3)	1,2
J2055+3630	B2053+36	97.34(5)	56025	0.267	6	19	65.5(19)	14.0(18)	−1.5(9)	1,2
J2102+38*	···	86.2(3)	55982	0.345	37	65	15.(2)	3.5(6)	···	···
J2105+28	···	62.48(14)	56156	0.041	7	11	12.(2)	0.65(16)	···	···
J2108−3429*	···	30.1(3)	57015	0.150	15	32	48.0(5)	2.3(4)	−1.(3)	23,26,12
J2108+4441*	B2106+44	139.8(17)	55626	0.286	30	67	80.7(11)	28.(3)	−0.8(6)	1,2
J2111+2106*	···	59.1(10)	56477	0.047	40	87	48.(3)	2.0(3)	−0.71(4)	20,60
J2113+2754*	B2110+27	25.1(3)	56156	0.227	13	25	98.0(12)	5.7(10)	−1.73(15)	8,13,1,2
J2113+4644*	B2111+46	141.3(2)	55557	0.180	31	118	403.8(18)	170(20)	−1.5(5)	1,2
J2113+67*	···	54.98(14)	56655	0.047	8	27	10(20)	0.6(15)	−1.487(7)	1,17
J2123+36[L]	···	108.2(3)	56025	0.056	21	39	20.2(6)	1.27(19)	···	···
J2122+54	···	31.78(3)	55348	0.003	2	6	10.4(7)	1.21(15)	···	···
J2124−3358	···	4.595(5)	56967	0.197	0.9	3	15.2(6)	7.5(14)	−1.4(3)	29,28
J2129−0429	···	16.88(7)	57214	0.191	1	5	44.(2)	30.(5)	···	···
J2131−31[B]	···	31.5(13)	56932	0.015	53	98	26.(2)	1.0(2)	···	···
J2136−1606*	···	18.5(3)	57875	0.123	19	36	42.0(9)	2.1(4)	···	···
J2137+64*	···	106.0(4)	55196	0.017	19	53	14.2(9)	0.90(14)	···	···
J2138+4911	···	168.4(17)	55524	0.103	26	59	53.3(7)	7.9(9)	···	···
J2139+00	···	31.18(8)	57696	0.323	14	31	24.0(14)	4.6(9)	···	···
J2139+2242*	···	44.1(2)	56298	0.096	40	62	217.9(14)	15.(2)	−0.2(2)	13,1,14

Table 4 continued

Table 4 *(continued)*

PSR[a]	PSR B	DM (pc/cm^3)	MJD	θ (deg)	W_{50} (ms)	W_{10} (ms)	S/N	S_{350} (mJy)	α	Refs.
J2144−3933*	···	3.(2)	57152	0.260	50	107	65.(3)	2.8(6)	−2.(2)	15,11,22
J2145−0750	···	9.005(6)	57445	0.157	1	3	316.(2)	100(20)	−1.41(11)	5,33,10,27,26,11,29
J2145+21[B]	···	44.1(3)	56459	0.009	24	44	10(20)	0.6(10)	···	···
J2148−34[B]	···	13.9(2)	56967	0.008	20	35	16.7(5)	0.84(17)	···	···
J2149+6329*	B2148+63	129.6(9)	55229	0.127	18	34	154.5(4)	21.(2)	−1.0(8)	1,2
J2150−03[B]	···	20.67(3)	57170	0.006	0.2	0.5	15.(3)	1.5(4)	···	···
J2150+5247	B2148+52	148.9(8)	55362	0.074	10	23	64.1(4)	7.9(9)	−0.9(4)	1,2
J2151+2315	···	20.6(9)	56297	0.248	17	49	8.2(13)	1.0(2)	···	···
J2154−2812*	···	32.9(3)	56838	0.309	9	22	28.3(9)	1.6(3)	···	···
J2155+2813*	···	78.1(4)	56156	0.252	26	41	15.4(14)	1.0(2)	−0.8(12)	1,49
J2155−3118	B2152−31	14.8(2)	56932	0.268	15	37	152.8(12)	10.(2)	−1.8(5)	2,11,12
J2156+2618	···	48.33(12)	56159	0.304	8	17	17.(2)	1.8(4)	−1.0(4)	1,61
J2157+4017*	B2154+40	71.1(3)	55847	0.072	67	124	206.6(11)	20.(2)	−0.7(5)	13,1,2
J2158−27[B]	···	22.15(12)	56837	0.498	13	25	30.(3)	9.(2)	···	···
J2202+21[A]	···	17.6(3)	56477	0.241	22	31	9.(3)	0.5(2)	···	···
J2203+50	···	76.98(19)	55504	0.949	29	72	10.(4)	1010(500)	···	···
J2205+1444	···	36.7(2)	58355	0.215	8	57	17.3(8)	1.8(3)	−1.355(2)	1,61
J2206+6151	···	168.8(8)	55199	0.220	24	49	10.1(10)	2.8(4)	−0.(5)	17,18
J2207−15[B]	···	27.5(19)	57789	0.004	25	40	13.1(12)	0.76(17)	···	···
J2207+40	···	11.33(16)	55657	0.057	28	61	23.5(4)	2.5(3)	···	···
J2208+5500*	···	104.6(2)	55348	0.245	14	29	54.0(8)	6.7(8)	−1.2(5)	1,3
J2210+21[L]	···	46.5(4)	56477	0.090	21	41	44.8(18)	1.9(3)	···	···
J2210+57	···	192.1(5)	55325	0.021	63	154	9.0(7)	1.28(17)	···	···
J2212+2933*	B2210+29	74.5(2)	56086	0.067	52	64	50.9(14)	3.6(6)	−1.0(2)	1,2
J2214+3000	···	22.56(3)	56086	0.243	0.2	0.8	8.4(9)	1.9(4)	−0.9(8)	33,44,34
J2217+5733*	···	130.49(9)	55327	0.176	43	99	26.6(8)	5.2(5)	−1.6(7)	3,17
J2219+4754*	B2217+47	43.49(13)	55554	0.285	7	15	650(30)	90(10)	−2.44(11)	8,1,2,73
J2222−0137	···	3.265(13)	57541	0.276	0.8	1	25.(3)	3.4(9)	−0.90(8)	1,26,11
J2222+2923*	···	49.44(7)	56086	0.240	5	21	18.7(10)	2.1(3)	···	···
J2222+5602*	···	163.3(3)	55348	0.394	42	122	9.5(8)	4.3(6)	···	···
J2225+6535*	B2224+65	36.22(17)	55196	0.216	22	78	76.(3)	19.(2)	−1.76(5)	1,2
J2227+30*	···	20.0(2)	56080	0.287	24	32	43.(2)	4.4(9)	−1.7(3)	1,74
J2229+64	···	193.8(4)	55196	0.005	51	74	13.2(15)	1.1(2)	···	···
J2229+2643	···	22.72(3)	56159	0.241	0.5	0.7	33.8(9)	7.7(14)	−1.4(4)	5,75,46
J2229+6114	···	205.1(13)	55249	0.129	8	17	20.3(17)	8.2(11)	−1.(5)	17,76
J2229+6205*	B2227+61	124.5(11)	55199	0.173	26	35	100.5(14)	17.4(19)	−2.0(5)	1,2
J2234+2114*	···	35.5(3)	56480	0.283	33	189	27.(2)	5.0(10)	−1.7(2)	13,1,61
J2238+6021*	···	185.3(7)	55250	0.158	25	56	46.(7)	4.3(9)	···	···
J2242+6950*	B2241+69	40.4(4)	55164	0.189	20	51	22.(2)	1.8(3)	−1.6(3)	1,2
J2243+69*	···	67.8(2)	55164	0.055	45	12	12.3(12)	1.13(19)	···	···

Table 4 continued

Table 4 *(continued)*

PSR[a]	PSR B	DM	MJD	θ	W_{50}	W_{10}	S/N	S_{350}	α	Refs.
		(pc/cm^3)		(deg)	(ms)	(ms)		(mJy)		
J2244+63	···	92.15(11)	55198	0.590	16	23	11.(6)	15.(8)	···	···
J2248−0101	···	29.1(12)	57510	0.264	13	21	58.3(6)	5.5(11)	−1.(2)	1,15,12
J2251+24[A]	···	34.6(3)	56295	0.130	19	84	8.(6)	0.7(6)	···	···
J2253+1516*	···	29.0(2)	58349	0.494	7	30	13.0(15)	6.0(13)	−1.7(9)	1,61
J2256−1024	···	13.774(2)	57151	0.286	0.2	0.4	62.(3)	17.(3)	···	···
J2257−16[B]	···	52.66(12)	57998	0.005	5	10	15.(4)	0.6(2)	···	···
J2257+5909	B2255+58	151.1(9)	55259	0.099	8	24	127.0(3)	95.(6)	−1.1(8)	1,2
J2302+4442	···	13.72(5)	55562	0.106	0.3	1	21.(8)	5.(2)	−0.2(12)	33,17,77
J2302+6028	···	156.7(3)	55250	0.109	20	35	99.6(11)	15.1(14)	−1.7667(19)	1,14
J2305+3100*	B2303+30	49.5(4)	56080	0.014	19	42	93.(3)	6.0(14)	−1.2(5)	8,1,2
J2305+4707	B2303+46	60.5(2)	55557	0.368	19	60	5.0(17)	1.3(5)	−1.65(16)	1,2
J2307+2225	···	6.74(13)	56459	0.290	10	24	15.(2)	1.4(3)	1.(2)	20,61
J2308+5547*	B2306+55	46.48(12)	55328	0.250	28	34	152.4(9)	61.(5)	−1.9(8)	1,2
J2313+4253*	B2310+42	17.31(9)	55625	0.153	8	15	208.3(6)	15.(2)	−0.7(14)	1,2
J2315+58	···	73.1(2)	55327	0.000	38	53	37.(6)	11.(2)	···	···
J2316+69*	···	71.3(2)	55164	0.011	17	32	11.(6)	0.8(4)	···	···
J2317+1439	···	21.9(3)	58350	0.259	0.4	0.7	30.(3)	6.7(15)	−1.0(3)	5,33,78,46
J2317+2149	B2315+21	20.8(3)	56477	0.068	23	41	349.5(17)	14.(2)	−1.48(5)	13,1,2
J2319+6411	···	246.1(5)	55198	0.321	38	77	32.(3)	23.(3)	···	···
J2321+6024*	B2319+60	94.0(5)	55250	0.171	111	184	117.(3)	109.(8)	−0.4(17)	1,2
J2322+2057	···	13.38(4)	56481	0.279	0.3	0.6	10(10)	1.3(17)	···	···
J2325−0530*	···	14.9(2)	57380	0.109	13	25	29.1(7)	1.3(2)	···	···
J2325+6316*	B2323+63	197.5(3)	55198	0.202	137	162	102.7(7)	22.(2)	−0.2(11)	1,2
J2326+6113*	B2324+60	122.5(6)	55235	0.108	15	22	74.(3)	13.4(15)	−0.6(2)	1,2
J2326+6141	···	34.5(2)	55199	0.780	26	46	17.(6)	200(80)	···	···
J2327+62[B]	···	193.4(6)	55199	0.000	4	25	9.4(17)	1.6(3)	···	···
J2329+47[L]	···	43.94(18)	55557	0.168	9	16	10(10)	0.6(5)	···	···
J2330−2005*	B2327−20	8.5(4)	58106	0.224	24	44	248.5(7)	13.(2)	−1.4(7)	8,2,11,12
J2333+6145	···	125.0[‡]	55199	0.185	23	97	6.(3)	1.9(10)	···	···
J2337+6151*	B2334+61	58.19(12)	55199	0.328	14	34	22.4(14)	6.9(8)	−1.29(13)	1,2
J2343+6221*	···	116.6(4)	55199	0.122	56	98	14.(2)	1.9(3)	···	···
J2346−0609*	···	22.5(3)	57384	0.189	10	73	105.5(14)	7.6(16)	−1.1(5)	15,11,12
J2347+02[A]	···	15.0(3)	57666	0.056	25	40	22.6(19)	1.2(3)	···	···
J2352+65	···	152.7(3)	55197	0.271	32	118	7.3(6)	2.3(3)	···	···
J2353−22[B]	···	9.92(14)	56666	0.015	9	21	32.(2)	1.4(2)	···	···
J2351+8533	···	38.2(2)	55082	0.011	17	33	16.4(4)	0.71(13)	0.(9)	1,17
J2354+6155*	B2351+61	94.7(2)	55199	0.344	10	29	19.3(6)	5.9(6)	−0.0(6)	1,2
J2356+22[B]	···	22.9(4)	56480	0.000	68	124	20.(2)	1.1(2)	···	···

Table 4 continued

Table 4 *(continued)*

PSR[a]	PSR B	DM (pc/cm^3)	MJD	θ (deg)	W_{50} (ms)	W_{10} (ms)	S/N	S_{350} (mJy)	α	Refs.

[a] Asterisks indicate pulsars with confirmed nulling or mode-changing during the observations. Letter superscripts indicate pulsars from survey discovery data: A corresponds to AODrift, ML to HTRU-mid and -lo lat, HL to HTRU-hi lat, S to SUPERB, G to GBT350, L to LOTAAS, and B to GBNCC.

† Single daggers in the α column correspond to pulsars with broken powerlaw spectral indices, which are reported in Table 2.

‡ Double daggers indicate DM values that could not be improved by searching, and so come directly from the ATNF catalog.

◇ PSR J2315+58 was found in a GBNCC beam that was $>3\sigma$ from the pulsar's published position, resulting in unbelievable flux density measurements. This is likely due to an error in the published position. So, we measure flux in the beam in which it was detected, and assume that the angular offset to the pulsar is zero.

References—1: Sanidas et al. (2019), 2: Lorimer et al. (1995a), 3: Surnis et al. (2019), 4: Joshi et al. (2009), 5: Kuzmin & Losovsky (2001), 6: Frail et al. (2016), 7: Lommen et al. (2000), 8: Stovall et al. (2015), 9: Bell et al. (2016), 10: Xue et al. (2017), 11: Jankowski et al. (2019), 12: Johnston & Kerr (2018), 13: Tyul'bashev et al. (2016), 14: Sayer et al. (1997), 15: Manchester et al. (1996), 16: Coenen et al. (2014), 17: Stovall et al. (2014), 18: Barr et al. (2013), 19: Lorimer et al. (1998), 20: Bilous et al. (2016), 21: Lynch et al. (2013), 22: Lorimer (1994), 23: Lyne et al. (1998), 24: Gould & Lyne (1998), 25: Nice et al. (2013), 26: Jankowski et al. (2018b), 27: Stairs et al. (1999), 28: Manchester et al. (2013), 29: Toscano et al. (1998), 30: Burgay et al. (2013), 31: Brinkman et al. (2018), 32: Chandler (2003), 33: Kondratiev et al. (2016), 34: Levin et al. (2016), 35: Hobbs et al. (2004), 36: Burgay et al. (2006), 37: Chatterjee et al. (2005), 38: Taylor et al. (1993), 39: Dewey et al. (1985b), 40: Ray et al. (1996), 41: Nicastro et al. (1995), 42: Kramer et al. (1999), 43: Bailes et al. (1997), 44: Ransom et al. (2011), 45: Wolszczan & Frail (1992), 46: Kramer et al. (1998), 47: Swiggum et al. (2017), 48: Bhattacharyya et al. (2013), 49: Lewandowski et al. (2004), 50: Lorimer et al. (1995b), 51: Costa et al. (1991), 52: Champion et al. (2005), 53: Johnston et al. (1992), 54: Stokes et al. (1986), 55: Ashworth & Lyne (1981), 56: Dembska et al. (2014), 57: Qiao et al. (1995), 58: Biggs et al. (1994), 59: Mohanty (1983), 60: Boyles et al. (2013), 61: Camilo & Nice (1995), 62: Han et al. (2016), 63: Janssen et al. (2010), 64: Janssen et al. (2009), 65: Foster et al. (1991), 66: Hulse & Taylor (1975), 67: Lazarus et al. (2015), 68: bbf (1984), 69: Fruchter et al. (1990), 70: Jacoby et al. (2007), 71: Navarro et al. (2003), 72: Gomez-Gonzalez & Guelin (1974), 73: Fomalont et al. (1992), 74: Camilo et al. (1996a), 75: Camilo (1995), 76: Halpern et al. (2001), 77: Cognard et al. (2011), 78: Camilo et al. (1996b)

Here we list pulsars for which we have measured DM to have changed from previous measurements by $\geq 3\sigma$.

Table 5. Pulsars with $\geq 3\sigma$ DM changes.

Name	DM_{cat}[a] (pc cm^{-3})	DM_{search}[b] (pc cm^{-3})	Period (s)
J0026+6320	245.06(6)	244.70(8)	0.318
J0218+4232	61.252(5)	61.230(2)	0.002
J0502+4654	41.83(2)	42.38(16)	0.639
J0610−2100	60.6662(17)	60.700(3)	0.004
J0610+37	27.1549(3)	39.09(11)	0.444
J0740+6620	14.9617(2)	14.950(2)	0.003
J0818−3049	133.7(2)	118.9(2)	0.764
J1125+7819	11.73(15)	11.220(4)	0.004
J1231−1411	8.090(1)	8.072(3)	0.004

Table 5 continued

Table 5 *(continued)*

Name	DM_{cat} [a] ($pc\,cm^{-3}$)	DM_{search} [b] ($pc\,cm^{-3}$)	Period (s)
J1320−3512	16.42(1)	15.52(11)	0.458
J1327−0755	27.91215(6)	27.900(2)	0.003
J1358−2533	31.27(1)	16.0(2)	0.913
J1600−3053	52.3299(2)	52.312(3)	0.004
J1614−2230	34.9179(3)	34.490(3)	0.003
J1614−3937	152.44(2)	151.7(15)	0.407
J1622−3751	153.8(5)	155.7(18)	0.731
J1647−3607	224(1)	228.50(5)	0.212
J1654−2713	92.31(12)	93.3(2)	0.792
J1701−3130	130.73(6)	131.40(7)	0.291
J1708−3426	190.7(3)	188.7(17)	0.692
J1712−2715	92.64(13)	91.78(6)	0.255
J1721−2457	47.758(19)	48.230(3)	0.003
J1722+35	23.83(6)	22.1(2)	0.822
J1729−2117	34.49(4)	34.22(17)	0.066
J1734−2415	126.3(7)	117.1(11)	0.613
J1742−3957	186(8)	220.(7)	1.016
J1745−3040	88.373(4)	88.01(9)	0.367
J1745−3812	160.8(4)	163.6(18)	0.698
J1750−3503	189.35(2)	190.5(17)	0.684
J1754−3510	82.3(3)	81.23(11)	0.393
J1800−0125	50.0(2)	51.0(2)	0.783
J1802+0128	97.97(12)	101.4(14)	0.554
J1805−0619	146.22(9)	147.1(11)	0.455
J1809−3547	193.84(7)	192.2(2)	0.860
J1811−2439	172.0(5)	167.2(17)	0.416
J1824−0127	58.0(15)	63.00(2)	2.499
J1824−2328	185(3)	195.3(2)	1.506
J1829+0000	114.0(4)	116.80(5)	0.199
J1832−0827	300.869(1)	303.7(16)	0.647
J1836−1008	316.98(3)	315.8(14)	0.563
J1839−0627	88.5(7)	92.49(12)	0.485
J1844+00	345.5(2)	346.6(11)	0.461
J1848−0023	30.6(1)	34.9(2)	0.538
J1849+2423	62.2677(16)	62.53(7)	0.276
J1855−0941	151.99(14)	153.60(8)	0.345
J1856−0526	130.5(4)	131.8(9)	0.370
J1903+2225	109.20(3)	110.8(16)	0.651
J1904+0004	233.61(4)	233.20(3)	0.140
J1908+2351	101.695(15)	102.2(9)	0.378

Table 5 continued

Table 5 *(continued)*

Name	DM_{cat} [a] ($pc\,cm^{-3}$)	DM_{search} [b] ($pc\,cm^{-3}$)	Period (s)
J1914+0219	233.8(4)	236.0(11)	0.458
J1918−0642	26.46(3)	26.580(7)	0.008
J1922+2018	203.31(1)	201.6(3)	1.173
J1935+52	71.9(1)	71.26(14)	0.568
J1940−2403	63.3(1)	65.4(4)	1.855
J1952+3252	45.006(19)	45.17(15)	0.040
J2016+1948	33.8148(16)	33.76(16)	0.065
J2044+4614	315.4(4)	311.3(3)	1.393
J2048+2255	70.684(2)	70.46(7)	0.284
J2151+2315	23.6(2)	20.6(9)	0.594
J2207+40	11.837(9)	11.33(16)	0.637
J2210+57	189.43(6)	192.1(5)	2.057
J2214+3000	22.545(2)	22.560(3)	0.003
J2229+6114	204.97(2)	205.10(13)	0.052
J2305+4707	62.067(3)	60.5(2)	1.066

[a] DM value from ATNF catalog.

[b] DM value from our search.

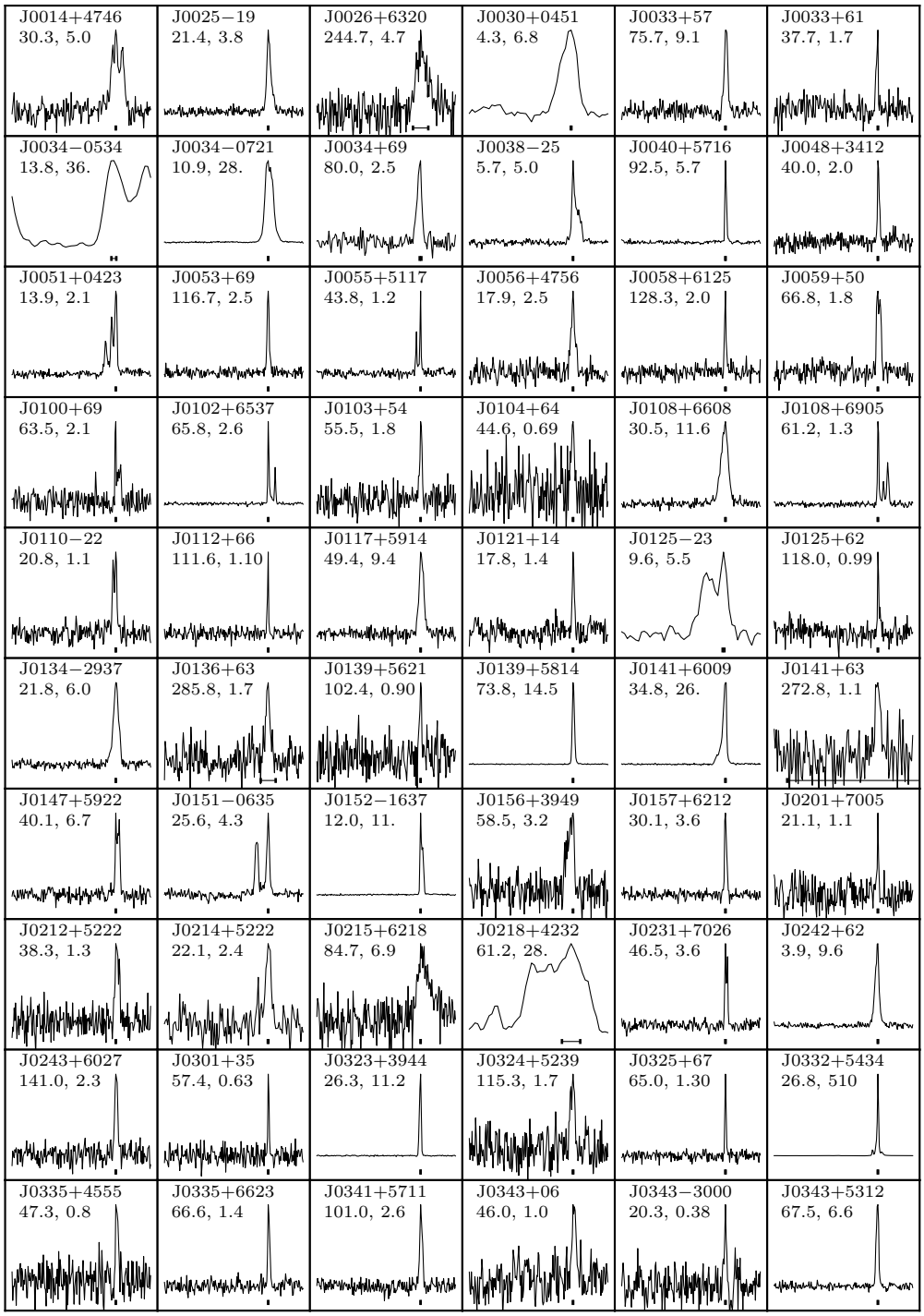

Figure 13. Pulse profiles for all detections. Text in each plot gives the pulsar name, dispersion measure in $\mathrm{pc\,cm^{-3}}$, and flux density in mJy. Centered beneath the profiles' peaks are error bars corresponding to the expected dispersive smearing of the pulse.

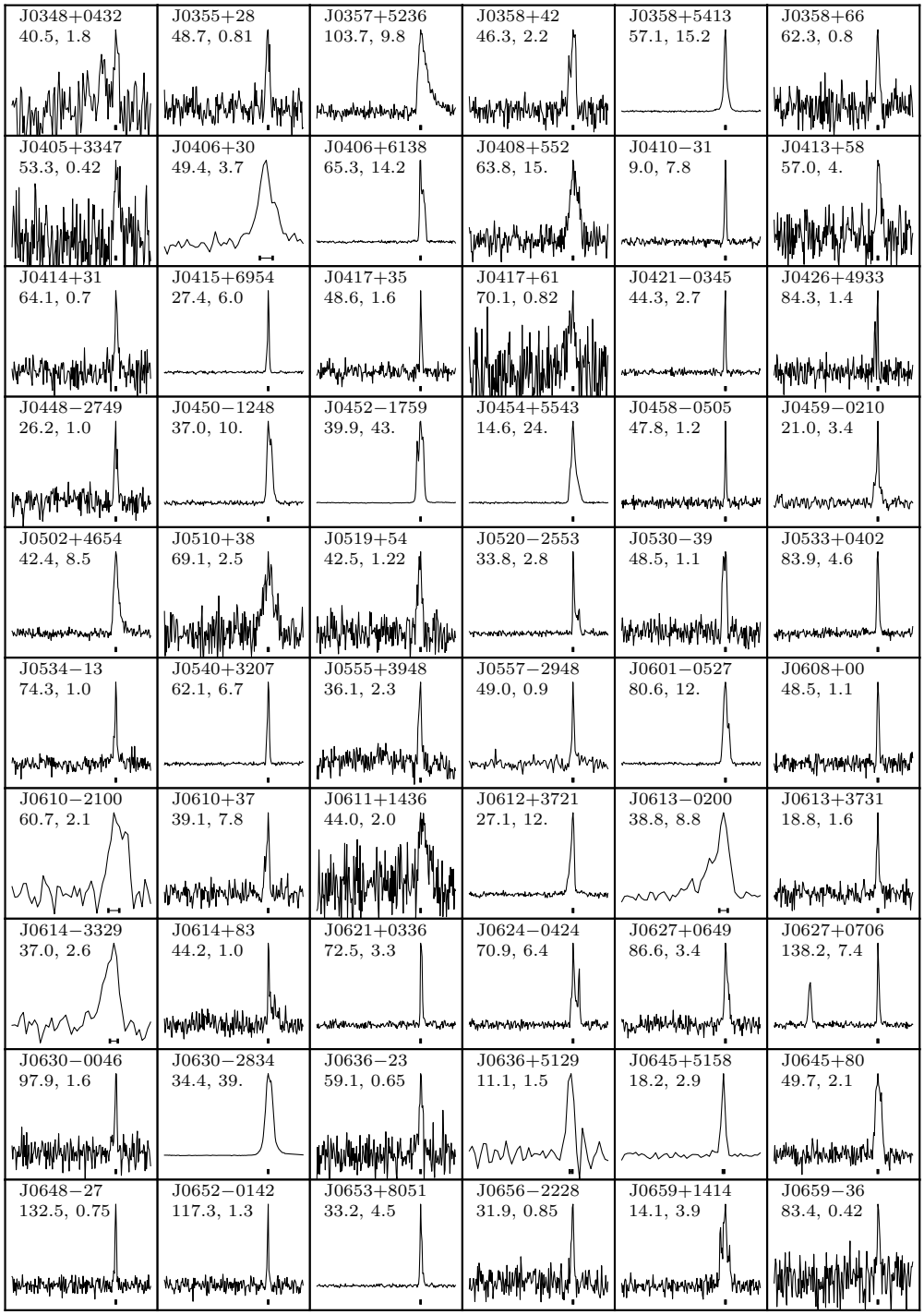

Figure 14. Profile plots (continued). See Figure 13 for details.

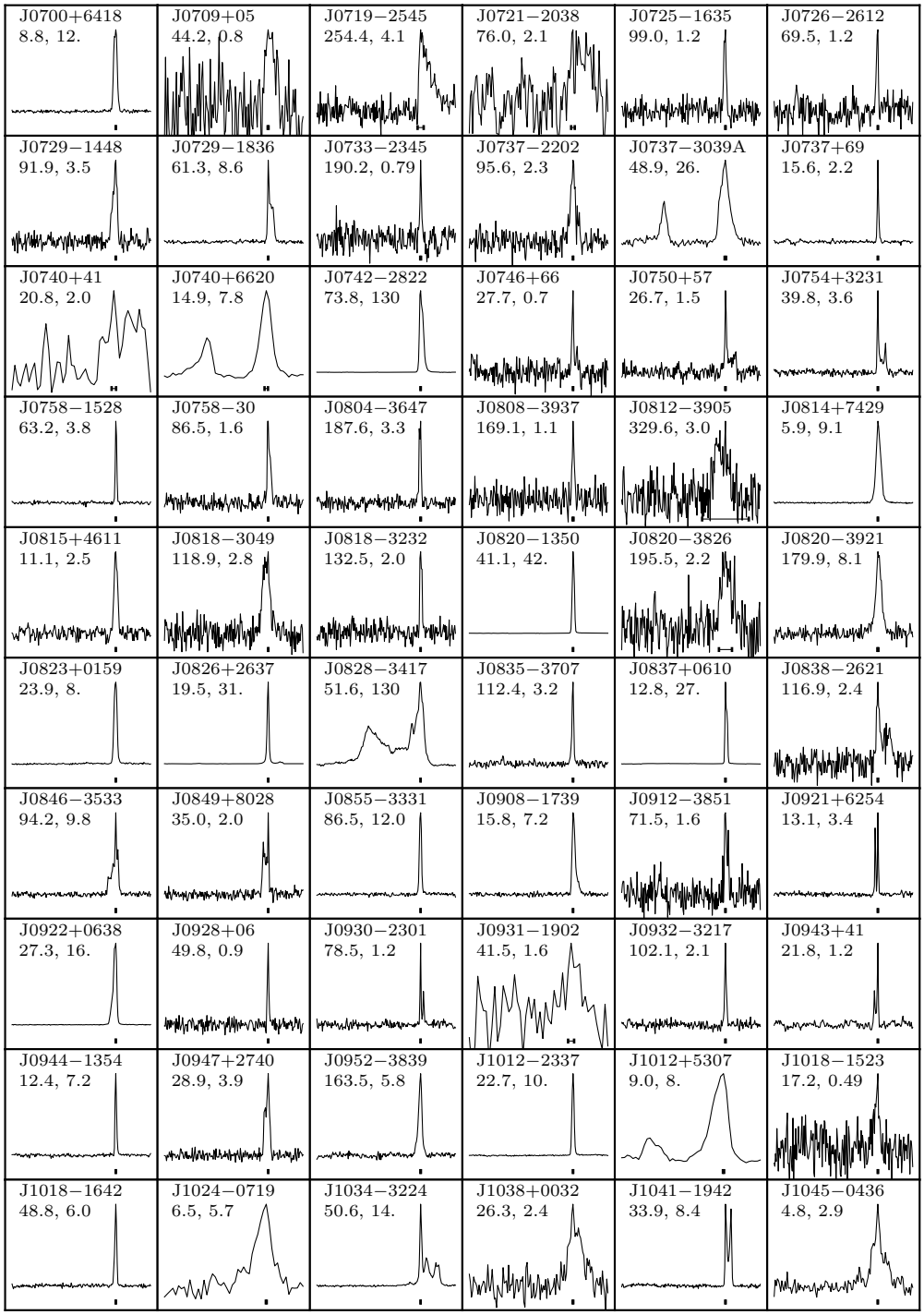

Figure 15. Profile plots (continued). See Figure 13 for details.

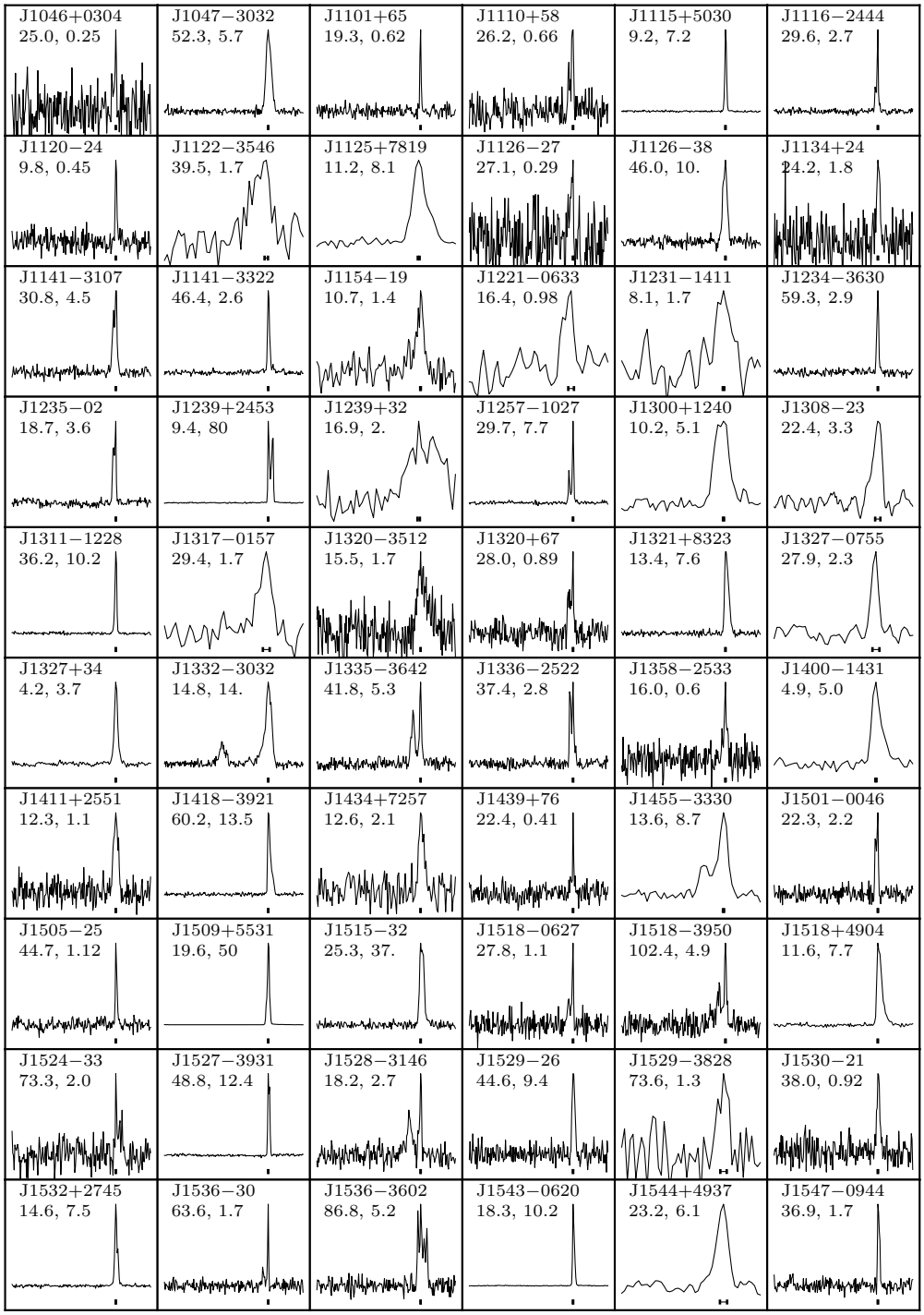

Figure 16. Profile plots (continued). See Figure 13 for details.

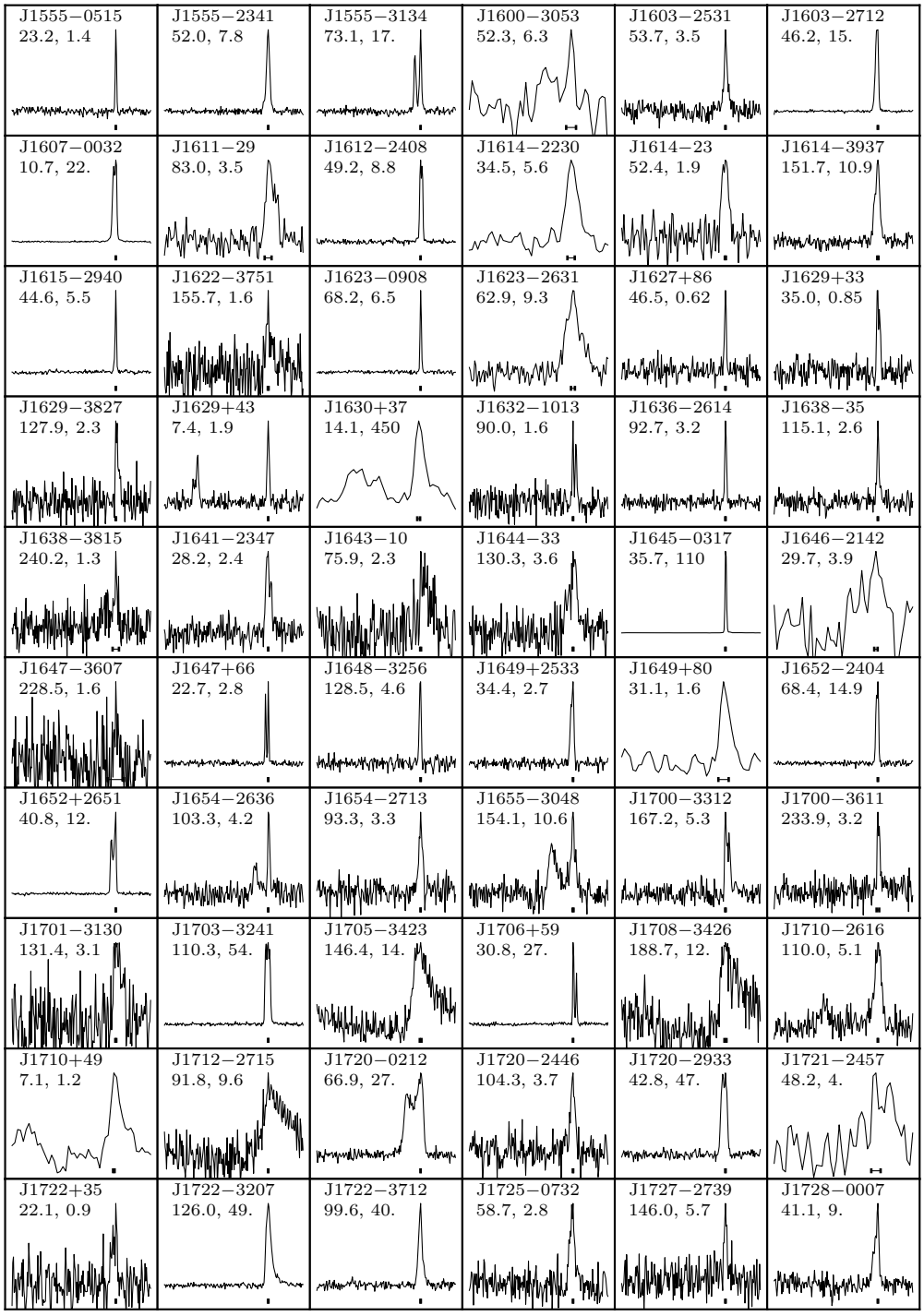

Figure 17. Profile plots (continued). See Figure 13 for details.

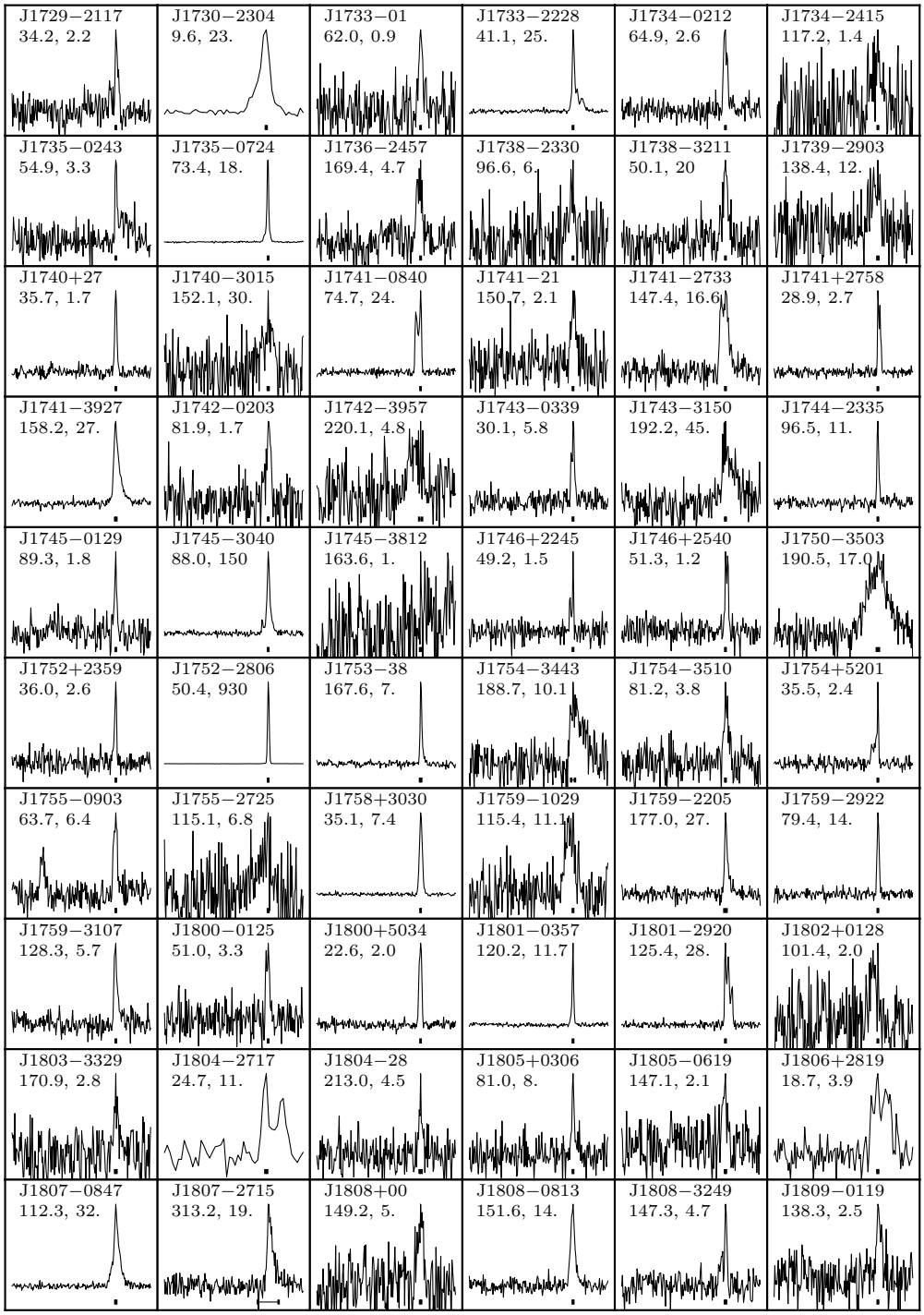

Figure 18. Profile plots (continued). See Figure 13 for details.

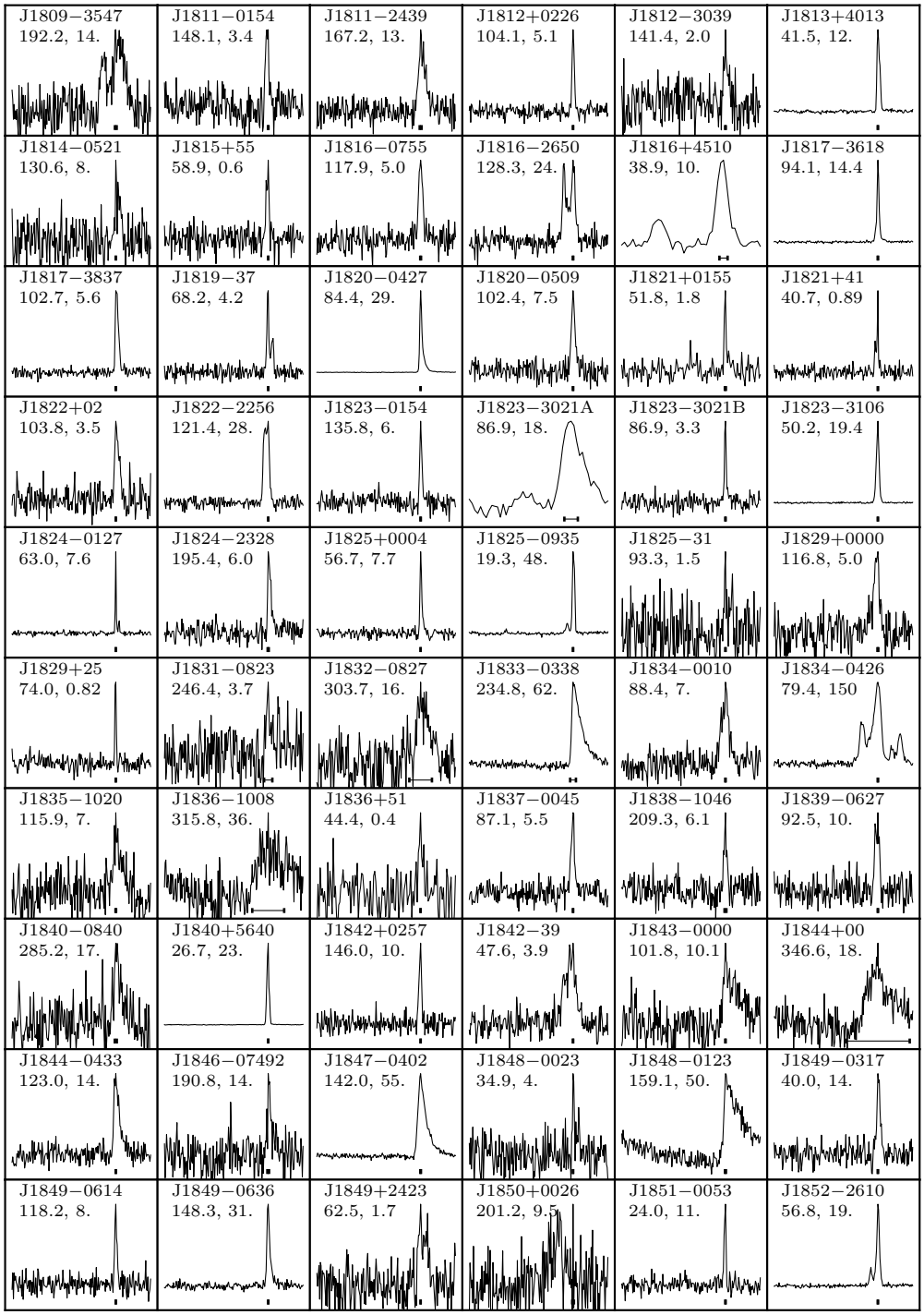

Figure 19. Profile plots (continued). See Figure 13 for details.

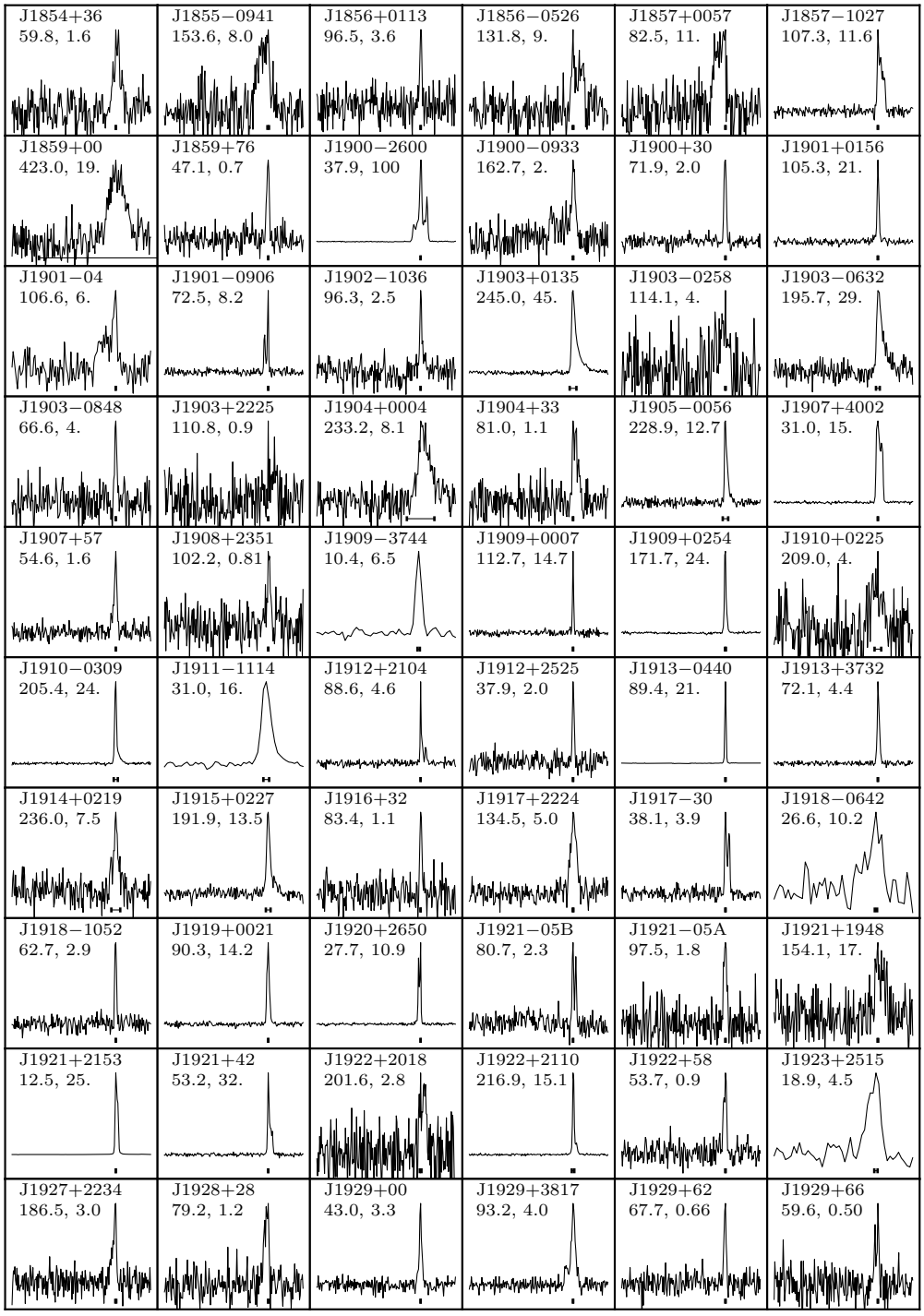

Figure 20. Profile plots (continued). See Figure 13 for details.

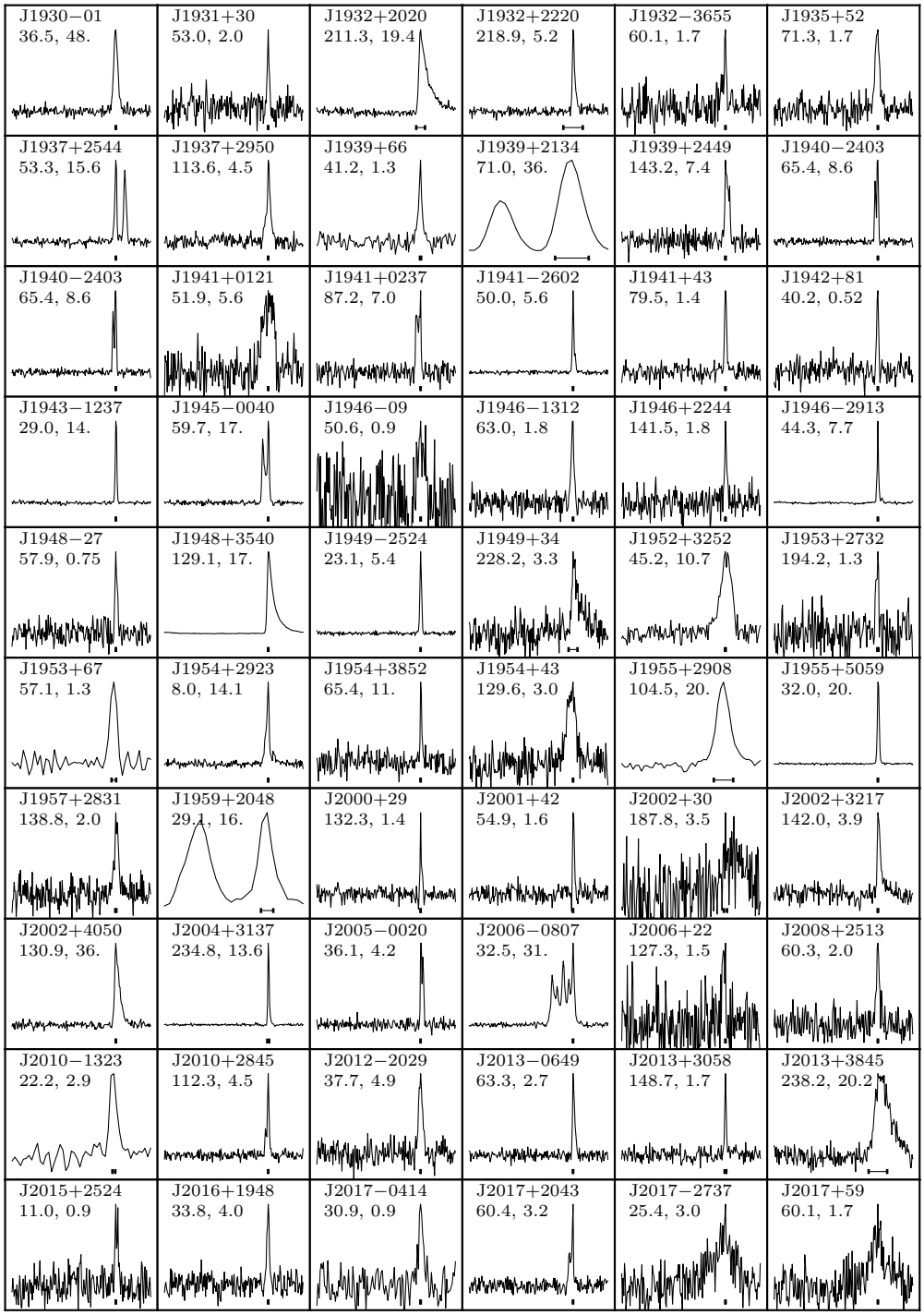

Figure 21. Profile plots (continued). See Figure 13 for details.

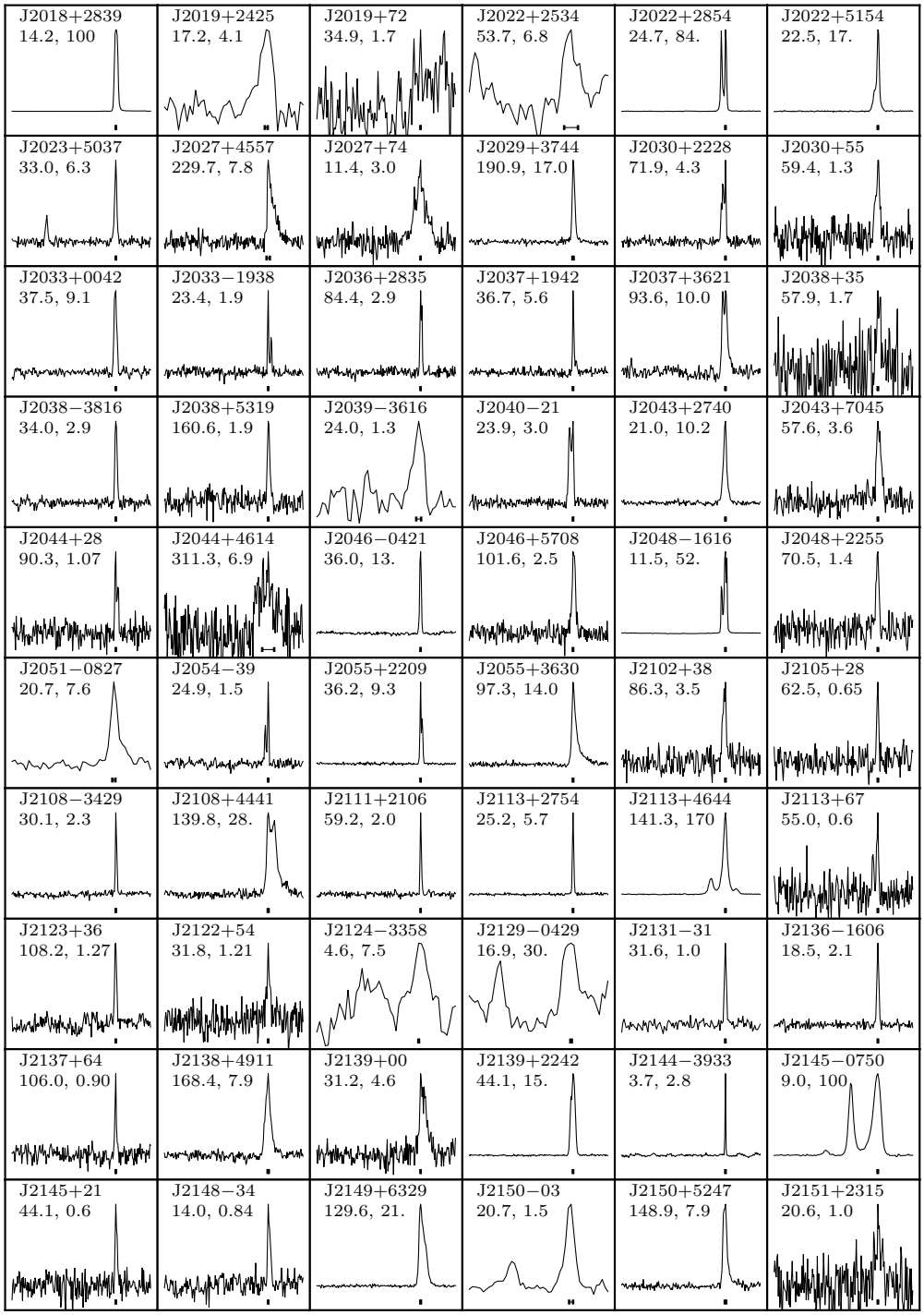

Figure 22. Profile plots (continued). See Figure 13 for details.

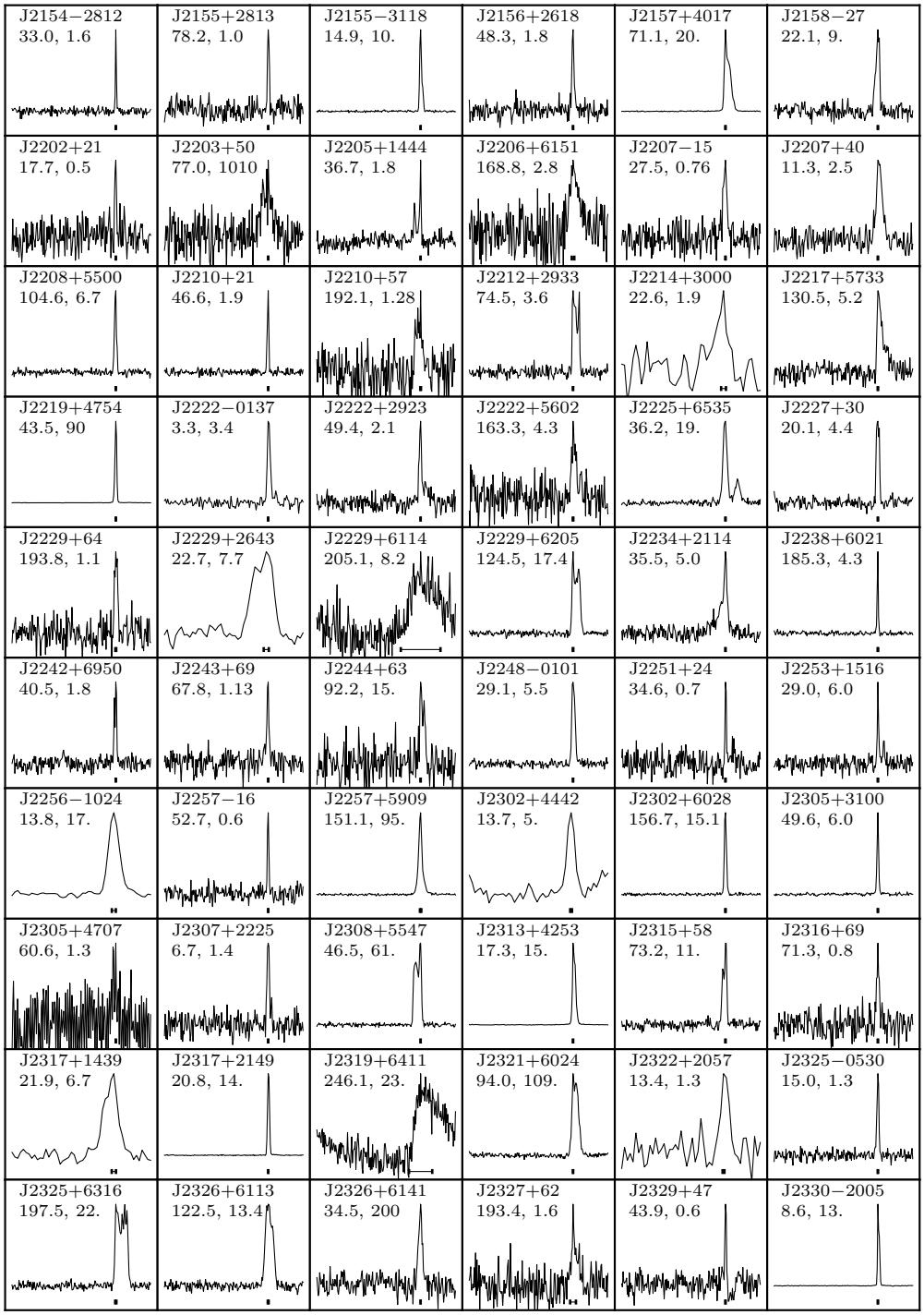

Figure 23. Profile plots (continued). See Figure 13 for details.

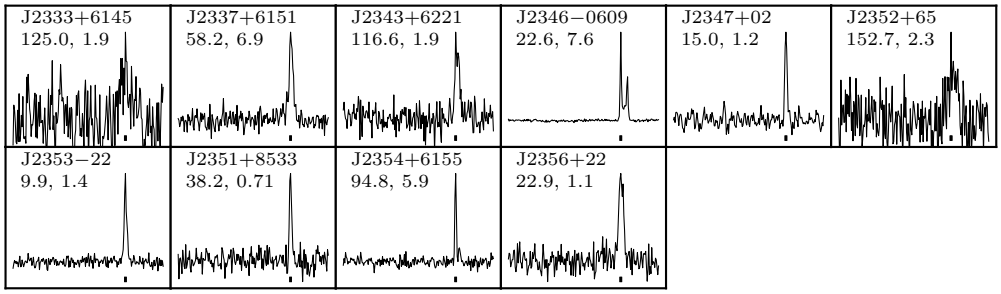

Figure 24. Profile plots (continued). See Figure 13 for details.